

SIGNATURES OF TOPOLOGICAL PHASES
IN ULTRACOLD FERMIONIC LADDERS

ANDREAS HALLER

MASTER THESIS

CONDENSED MATTER THEORY - KOMET337
DEPARTMENT OF PHYSICS, MATHEMATICS AND COMPUTER SCIENCE
JOHANNES GUTENBERG-UNIVERSITÄT MAINZ

Signatures of Topological Phases
In Ultracold Fermionic Ladders

SUPERVISOR:

Jun.-Prof. Matteo Rizzi, Ph.D.

CO-SUPERVISOR:

Michele Burrello, Ph.D.

LOCATION:

Mainz

TIME FRAME:

20th October 2015 - 17th October 2016

ABSTRACT

In the presence and absence of interactions, we investigate what interesting phases can emerge in simple, quasi-one-dimensional setups. The physical framework are fermionic two- and four-leg ladder models which are presently feasible (or envisionable in short-time) in cold atomic experiments. We derive and analyze analytic solutions for many expectation values in finite size systems for both two- and four-leg ladder models (in Ch. I). Applying the concept of resonances in chiral currents (see Ch. I.5), we find a topological order parameter (see Ch. I.6), distinguishing between trivial and quantum Hall (QH) phases. In Ch. II, we aim for evidence about fractional QH phases in simulations of interacting fermionic ladders. Numerical observations in finite size setups give rise to the conclusion that constraints on the Luttinger parameter K_ρ may prevent the emergence of fractional $\nu < 1/2$ phases in case of nearest neighbor Hubbard interactions (see Ch. II.3). For both nearest and next-to-nearest neighbor interactions, simulations show the presence of exotic $\nu = 1/2$ phases (see Ch. II). We obtain convincing results for the presence of $\nu = 1/3$ Laughlin states in strong coupling regimes of next-to-nearest neighbor Hubbard interactions (see Ch. II.4). We implement special engineered interactions that yield multi-particle operators which are predicted to give rise to Laughlin states (see Ch. III). For intermediate interacting regimes we face phase separation in multiple crystalline insulating phases and combine exact arguments with results from simulations to explain the structure of crystalline phases in the strong-coupling regime (see Ch. III). In weak-interacting regimes, we discover an emerging integer QH phase for the density-assisted spin-flip interaction (see Ch. III).

DECLARATION

Hiermit erkläre ich, dass ich diese Abschlussarbeit selbständig verfasst habe, keine anderen als die angegebenen Quellen und Hilfsmittel benutzt habe und alle Stellen, die wörtlich oder sinngemäß aus veröffentlichten Schriften entnommen wurden, als solche kenntlich gemacht habe. Darüber hinaus erkläre ich, dass diese Abschlussarbeit nicht, auch nicht auszugsweise, im Rahmen einer nichtbestandenenen Prüfung an dieser oder einer anderen Hochschule eingereicht wurde.

I hereby declare that this thesis and the work reported herein was composed by and originated from me. Information derived from the published and unpublished work of others has been acknowledged in the text and references are given in the list of sources. Furthermore I declare that this thesis has not been submitted at any university within the scope of a failed exam.

Mainz, 17th October 2016

ACKNOWLEDGEMENTS

I am very grateful to Matteo Rizzi. For the engagement and time, for his support and fruitful discussions which motivated me to stay in his group and explore the rich field of topological states of matter. I had the pleasure to work with him in all periods of my undergraduate studies - his enthusiasm and mentoring influenced me by far the most.

I would like to highlight special acknowledgement to Michele Burrello for all of his many contributions regarding this project and for exciting analytical results, which he gladly shared. For every single question he provides two good answers, which helped me scratch the surface of understanding the difficult, yet beautiful field theoretic description of matter.

Many thanks to Leonardo Mazza for stimulating discussions and help - and for outstanding competence, always pushing forward.

Without Johannes Jünemann no numerical results could be presented. He is the leading author of the code without whom any simulation in thesis would be impossible. For all discussions, for his advice and support that extended to a valuable friendship, I express my gratitude.

Many thanks to Manon Bischoff and my fellow students and good friends Philipp Schmoll and William Janke for their corrections. For all of those joint lunches and coffee breaks, which always extended to welcome diversions and off-topic debates. All of these remarkable people working on different and challenging projects make university an experience of inestimable value - I would not want to miss it for the world.

I express my deepest gratitude to Susanne Stamer, the love of my life. For the unconditional support and encouragement all along my studies.

CONTENTS

INTRODUCTION	1
I FREE SYSTEM	4
I.1 Hamiltonian	4
I.2 Symmetries and Analytic Solution	7
I.3 Dispersion Relation	10
I.4 Entanglement Entropy	15
I.5 Chiral Currents	23
I.6 Momentum Zero Current	30
I.7 Simulation Feasibility	32
II HUBBARD INTERACTION	39
II.1 Motivation	40
II.2 Mean Field Approximation	43
II.3 Restrictions From Bosonization	46
II.4 Numerical Results	51
III PERSPECTIVES	56
IV SUMMARY	63
A LUTTINGER LIQUIDS	65
A.1 Constructive Bosonization	65
A.2 Phenomenological Bosonization	72
B SUPPLEMENTARY MATERIAL	75
B.1 Jordan-Wigner Transformation	75
B.2 Reformulation to MPO	78
B.3 Transformation to Majorana-Fermions	86
C OPTICAL LATTICES	88
C.1 Optical Potentials	88
C.2 Artificial Gauge Fields and State Dependent Superlattices	90

ACRONYMS & NOMENCLATURE

QH	quantum Hall
fQH	fractional quantum Hall
iQH	integer quantum Hall
MPS	Matrix Product States
MPO	Matrix Product Operator
DMRG	Density Matrix Renormalization Group
PBC	Periodic Boundary Conditions
OBC	Open Boundary Conditions
VNEE	von Neumann entanglement entropy
U(1)	U(1) symmetry
BDI	BDI symmetry class [1]
SU(2)	special unitary group of degree 2

INTRODUCTION

The results which we present in this master thesis must be regarded preliminary work within the scope of a greater goal. This goal is to *engineer* fractional topological phases in the environment of cold atomic gases giving rise to so-called parafermionic \mathbb{Z}_N modes [2]. We therefore combine geometrical constraints, different range of interactions and (synthetic) gauge fields to find a microscopic tight-binding model, enriched with proper density-dependent hoppings and interactions, leading to the emergent low-energy \mathbb{Z}_N theory postulated in recent works [3]. The inspiration is adapted from an alternative approach, often called wire deconstructionism [4], where fractional states emerge as a consequence of suitable interactions appearing under renormalization group analysis as multi-particle terms in the one-dimensional Luttinger liquid picture (see Ch. III).

Before we jump straight into such complicated setups, we need to accomplish some short-time milestones that increase transparency between field theoretic predictions and actual results of more physical setups. For once, we need to know, if it is possible to stabilize $\nu = 1/3$ fractional quantum Hall (fQH) phases in finite size systems by means of "simple" two-body interactions as required by simulations and experiments, or, if such phases require strong-coupling regimes and approaching the thermodynamic limit. If this conclusion is negative, could a three-body interaction improve the situation at smaller interaction-strengths, or would such systems suffer from dramatic restrictions on the density profile thus prevent us to explore the full phase space from low to high density?

The answer to both milestones will give further conclusions about which Hamiltonian terms are to be used in the long-term vision of this project.

INTEREST IN TOPOLOGICAL QUANTUM MATTER

We start with a quick overview about research trends and prospects of topological phases and topological states before we analyze their properties and signatures in the context of multi-species ladder models.

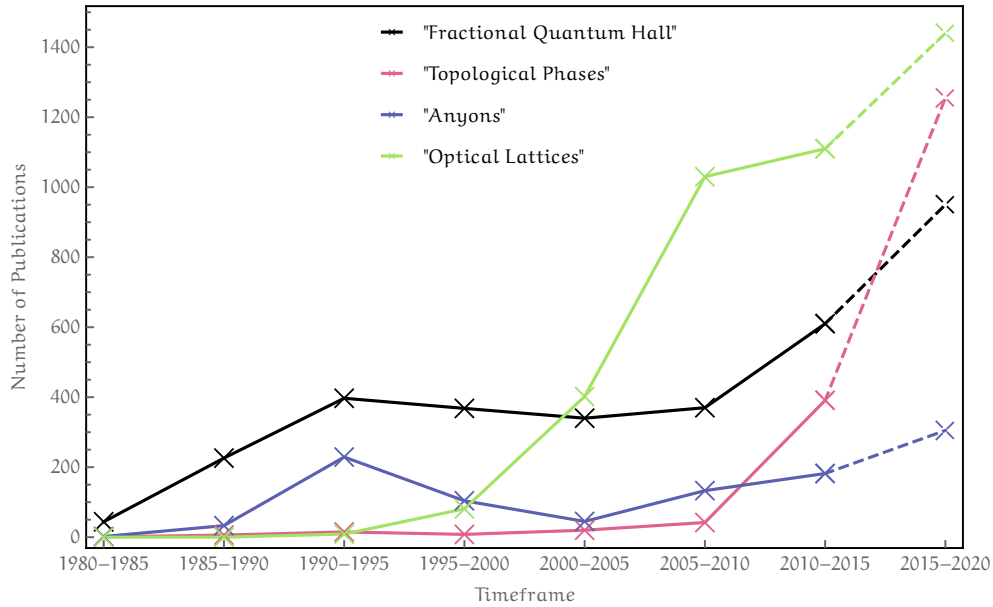


Figure 1: Publications per timeframe. The content is extracted from search results in google scholar. Data points show the number of publications with a title containing phrases such as: "Fractional Quantum Hall", "Topological Phases", "Anyons" and "Optical Lattices". In the past ten years, topological phases and topological states of matter became an exciting new field in condensed matter theory.

By the turn of the millennium, the rapid boost of publications in the framework of optical lattices (many in the context of ultracold atoms) is strongly correlated with the increasing theoretical research interest in exotic excitations such as (fractional) QH phases, anyons and topological phases in general. This exciting boost is due to the possibility to confine atoms in well-controllable lattice structures dictated by a certain laser setup (see App. C). Such systems provide the required framework to simulate simple lattice models which have been subject for theoretical analysis for a long time [5]. Due to the nature of being highly controllable in the laboratory, synthetic quantum matter is the best suited experimental environment to push forward the verification and comprehension of exotic, low-dimensional states of matter. In particular, the study of quasi-one-dimensional (spin) ladders is very fruitful, because they show all advantages of one-dimensional quantum matter (such as a lot of analytical and numerical tools to treat them), and, at the same time exhibit some of the rich effects which show up exclusively for higher-dimensional systems such as quantum Hall physics.

Additionally, topological phases provide the proper environment for the emergence of exotic quasi-particle excitations. Sometimes, these excitations are so-called anyons, which extend the usual (± 1) exchange statistics of bosons and fermions to a more general braiding statistics. If the particle exchange of two anyons yields a complex phase in the overall wavefunction, they are called Abelian anyons due to their commuting nature. On the other hand, if braiding of anyons yields non-commuting unitary transformations between a subspace of degenerate states, anyons are called non-Abelian. These particular topological states of matter are extraordinarily interesting with the prospect of quantum information: If non-Abelian anyons provide rich braiding statistics, they are suited to implement all quantum gates necessary for universal quantum computation [6].

One revolutionary milestone for condensed matter theory would be to verify the existence of such superior non-Abelian states in finite size setups (experimentally, or at least numerically), which is one of the main reasons why researchers are interested in topological phases of low-dimensional systems. This trend has been enhanced by new numerical schemes based on tensor network states [7], which are particularly suited to approximate ground states of quantum systems in low dimensions. Aspects of conformal field theory show that ground states of short-range Hamiltonians obey what is called an area law for entanglement [8]. It states that the bipartite entanglement of ground states must have an upper bound – thus providing a quantity to connect with renormalization group aspects [9]. This allows to reduce low-energy many-body wavefunctions to be decomposed into what is called Matrix Product States (MPS) [10]. It is known that Density Matrix Renormalization Group (DMRG), which is widely used in many different communities, is a scheme which relies on tensor network methods, effectively mimicking certain aspects of quantum systems [11].

We explicitly use both *analytical* and *numerical arguments* to find an answer to the following question: *Is it possible to utilize (non-)local observables as signatures to verify the presence of topological (integer and fractional QH) phases in (non-)interacting fermionic multi-species ladder systems of finite sizes?* In particular, for integer and emerging fractional quantum Hall phases, recent developments show that so-called chiral currents may be exceptionally well suited for this specific task [12]. However, a detailed numerical analysis for fermionic setups is still lacking in the literature, which is why we focus on properties and signatures of the chiral current in finite-sized systems.

I

FREE SYSTEM

In this chapter we present important properties of the non-interacting Hamiltonian in Eq. I.3. This model has already been given a detailed account of topological properties recently [13]. After a thorough recap including a full solution in the next sections, we want to go beyond and explore the nature of chiral currents, providing the power of detecting topological phases.

The first section gives a detailed overview about the different terms in the free Hamiltonian (and their physical significance). We introduce the reader into the notation that we will use for this thesis.

In the second section we investigate and characterize present symmetries in order to arrive at a more simple form of the Hamiltonian according to [13]. The exact solution of the dispersion relation can be derived in Periodic Boundary Conditions (PBC). Along this way we will focus on its set of symmetries, providing a more intuitive understanding of the two fermion stripe's role in the physics and dynamics of the Hamiltonian. We will also consider systems with Open Boundary Conditions (OBC), whose path to a solution is more demanding.

The remaining sections focus on observables and entanglement properties of the non-interacting Hamiltonian with OBC. All analytic work then serves in the last part of this chapter as foundation and starting point to compare numerical results to (as preliminary work for Ch. II and Ch. III).

I.1 HAMILTONIAN

Let us suppose that fermionic annihilation \hat{a}_τ and creation operators \hat{a}_τ^\dagger refer to four-spinor fermions which can be labelled with a spacial (τ) and spin (σ) degree of freedom. We make explicit use of a set of two Pauli matrices $\{\sigma_i, \tau_i\}$, $i \in \{x, y, z\}$ to access this two internal degrees of freedom. Each of the

four components of \hat{a}_r are fermionic operators $\hat{c}_{\sigma\tau}^\dagger$ labelled by τ and σ , satisfying the fermionic commutation relations

$$\left\{ \hat{c}_{r,\tau\sigma}^\dagger, \hat{c}_{r',\tau'\sigma'} \right\} = \delta_{rr'} \delta_{\tau\tau'} \delta_{\sigma\sigma'}, \quad \left\{ \hat{c}_{r,\tau\sigma}^\dagger, \hat{c}_{r',\tau'\sigma'}^\dagger \right\} = 0. \quad (\text{I.1})$$

We will use the possible representation of \hat{a}_r which is a four-component vector composed of such single-species operators

$$\hat{a}_r := (c_{r,++}, c_{r,+ -}, c_{r,- +}, c_{r,--}). \quad (\text{I.2})$$

Having these definitions at hand, it is possible to define a four-leg ladder out of fermions, confined to equally spaced grid positions r and subject to the following non-interacting Hamiltonian

$$\begin{aligned} \hat{H} = \sum_r \hat{a}_r^\dagger t \left(\tau_z \otimes e^{i\sigma_z \frac{B}{2}} \right) \hat{a}_{r+1} + \hat{a}_{r+1}^\dagger t \left(\tau_z \otimes e^{-i\sigma_z \frac{B}{2}} \right) \hat{a}_r \\ + \hat{a}_r^\dagger \left(\Omega (\mathbb{1} \otimes \sigma_x) + J (\tau_x \otimes \mathbb{1}) + \mu (\tau_z \otimes \mathbb{1}) + \mu_0 (\mathbb{1} \otimes \mathbb{1}) \right) \hat{a}_r. \end{aligned} \quad (\text{I.3})$$

We can understand the setup and all contributions, when we picturize this particular system, split up the internal degrees of freedom and place arrows to indicate the possible intra- and inter-species flips that are encoded in the Hamiltonian.

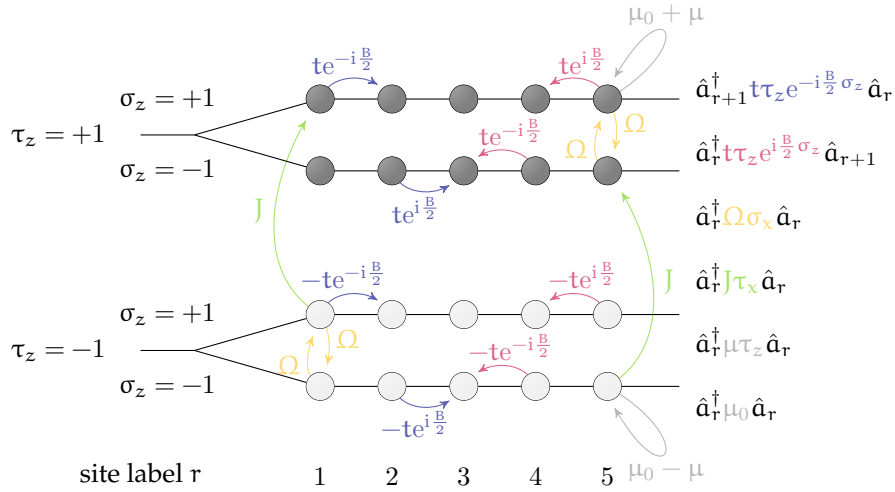


Figure 2: Contributions of the different terms in the Hamiltonian. The arrows represent the direction of movement for a single particle changing its lattice position $(r, \tau\sigma) \rightarrow (r', \tau'\sigma')$. At each virtual site there are at most five steps possible - a chain flip from $\tau = \pm 1 \rightarrow \tau' = \mp 1$, a spin flip $\sigma = \pm \rightarrow \sigma' = \mp$, hopping along each chain $r \leftrightarrow r \pm 1$ and staying at the same vertex.

The following table shows the physical meaning of individual contributions, where the relevance of the hopping is dictated by a set of parameters:

1.	$r \in \{1, \dots, L\}$	L $\in \mathbb{N}$ denotes the system size	
2.	$\Omega \in \mathbb{R}^+$	contribution of spin-flips	
3.	$J \in \mathbb{R}^+$	contribution of chain-tunneling	
4.	$\mu \in \mathbb{R}$	potential barrier between τ chains	(I.4)
5.	$t \in \mathbb{R}$	nearest-neighbor hopping	
6.	$\mu_0 \in \mathbb{R}$	chemical potential (mostly redundant)	

The parameter r denotes the position along a 1D stripe of equally spaced grid vertices. For simplicity, the lattice spacing and \hbar have been set to unity. The systems we want to observe are confined to a finite size L and obey either periodic or open boundary conditions, which we will define explicitly when needed. In the chosen gauge, the vector potential results in a Peierl's phase in the Hamiltonian, contributing to the hopping terms along the same wire. We can shift this phase by means of a unitary transformation $\hat{a}_r \rightarrow \hat{a}_r e^{-iB r \sigma_z}$. The new gauge then yields a factor $e^{\pm iB r}$ for the spin-flips instead. We recognize for both gauges, the accumulated phase when hopping in a circle around each plaquette remains a constant $e^{\pm iB}$. The \pm sign depends only on the hopping direction for such circle-processes. For the sake of book-keeping (e.g. for applying a Jordan-Wigner transformation or a mapping to Majorana fermions, which we do explicitly in App. B), let us introduce here the following order of fermionic modes acting on Fock space. After a thorough recapitulation including a full solution in the

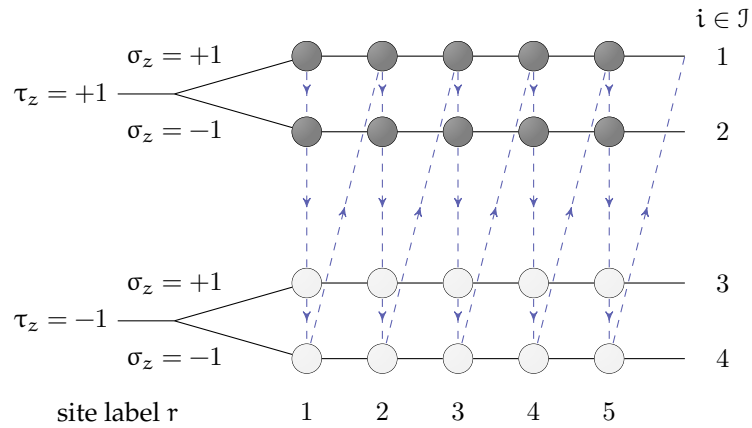


Figure 3: Possible relabeling of the lattice vertices. This allows for a convenient definition of a single component $\hat{c}_{j,\tau\sigma} \rightarrow (\hat{a}_r)_i$.

next subsections we want to go beyond and explore i.e. chiral currents as order parameter for detecting topological phases.

I.2 SYMMETRIES AND ANALYTIC SOLUTION

For all our purposes it is valid to set $\mu_0 = 0$ since this external potential corresponds to a constant energy offset for all sites. We will from now on strictly assume $\mu_0 = 0$. Let \hat{N} be the particle number operator that we will define as sum of densities at all possible lattice vertices

$$\hat{N} = \sum_{\mathbf{r}} \sum_{\tau\sigma} \hat{c}_{\mathbf{r},\tau\sigma}^\dagger \hat{c}_{\mathbf{r},\tau\sigma} = \sum_{\mathbf{r}} \hat{a}_{\mathbf{r}}^\dagger \hat{a}_{\mathbf{r}} := \hat{a}_{\mathbf{r}}^\dagger \hat{a}_{\mathbf{r}}, \quad (\text{I.5})$$

using sum convention. We see that the particle number commutes with the free Hamiltonian since for an arbitrary 4×4 matrix Γ

$$\begin{aligned} \hat{a}_{\mathbf{r}}^\dagger \Gamma \hat{a}_{\mathbf{r}}, \hat{N} &= \hat{a}_{\mathbf{r},i}^\dagger \Gamma_{i,j} \hat{a}_{\mathbf{r}',j} \hat{a}_{\mathbf{r}'',k}^\dagger \hat{a}_{\mathbf{r}'',k} \\ &= \hat{a}_{\mathbf{r},i}^\dagger \Gamma_{i,j} \left(\delta_{\mathbf{r}'\mathbf{r}''} \delta_{jk} - \hat{a}_{\mathbf{r}'',k}^\dagger \hat{a}_{\mathbf{r}',j} \right) \hat{a}_{\mathbf{r}'',k} \\ &= \hat{a}_{\mathbf{r},i}^\dagger \Gamma_{i,j} \hat{a}_{\mathbf{r}',j} + \hat{a}_{\mathbf{r}'',k}^\dagger \hat{a}_{\mathbf{r},i} \Gamma_{i,j} \hat{a}_{\mathbf{r}',j} \hat{a}_{\mathbf{r}'',k} \\ &= \hat{a}_{\mathbf{r},i}^\dagger \Gamma_{i,j} \hat{a}_{\mathbf{r}',j} - \hat{a}_{\mathbf{r}'',k}^\dagger \hat{a}_{\mathbf{r},i} \hat{a}_{\mathbf{r}'',k} \Gamma_{i,j} \hat{a}_{\mathbf{r}',j} \\ &= \hat{a}_{\mathbf{r},i}^\dagger \Gamma_{i,j} \hat{a}_{\mathbf{r}',j} - \hat{a}_{\mathbf{r}'',k}^\dagger \left(\delta_{\mathbf{r}\mathbf{r}''} \delta_{ik} - \hat{a}_{\mathbf{r}'',k} \hat{a}_{\mathbf{r},i}^\dagger \right) \Gamma_{i,j} \hat{a}_{\mathbf{r}',j} \\ &= \hat{N} \hat{a}_{\mathbf{r}}^\dagger \Gamma \hat{a}_{\mathbf{r}}, \end{aligned} \quad (\text{I.6})$$

using commutation relations of the component representations of \hat{a} . This means that the free system conserves the number of particles,

$$[\hat{H}, \hat{N}] = 0. \quad (\text{I.7})$$

Another way of seeing that N is a good quantum number is due to the invariance of the Hamiltonian sending $\hat{a}_{\mathbf{r}} \rightarrow e^{i\alpha} \hat{a}_{\mathbf{r}}$ which is a rotation in the complex plane and hence a transformation by a representative of the $U(1)$ symmetry. We make explicit use of this symmetry in a more efficient numerical implementation of variational MPS [14]. Such symmetry implementations in tensor network states, even the task of implementing a working MPS routine itself, is a time-consuming project and has to be considered out of scope for this thesis. For introductory concepts of MPS and for a working matlab code without symmetries, we will refer to [15].

In the next part of this section, we try to shape the Hamiltonian in Eq. I.3 to a more convenient form using unitary transformations - i.e. we want to diagonalize \hat{H} . Instead of using tensor products in Eq. I.3, it is more practical to introduce a diagonal matrix T and a hermitian matrix O that describe the nearest neighbor and inter-species hoppings respectively. With this, the Hamiltonian becomes

$$\hat{H} = \sum_{\mathbf{r}} \hat{a}_{\mathbf{r}}^\dagger T \hat{a}_{\mathbf{r}+1} + \hat{a}_{\mathbf{r}+1}^\dagger T^* \hat{a}_{\mathbf{r}} + \hat{a}_{\mathbf{r}}^\dagger O \hat{a}_{\mathbf{r}}. \quad (\text{I.8})$$

We may use the Fourier transform of $\hat{a}_r = \frac{1}{\sqrt{L}} \sum_k \hat{a}_k e^{ikr}$, which simplifies the nearest neighbor hopping to

$$\begin{aligned}\hat{H} &= \sum_{r=1}^L \sum_{k=1}^L \sum_{k'=1}^L \frac{1}{\sqrt{L}} e^{i(k'-k)r} \left(\hat{a}_k^\dagger T \hat{a}_{k'} e^{ik'} + \text{H.c.} + \hat{a}_k^\dagger O \hat{a}_{k'} \right) \\ \hat{H} &= \sum_k \hat{a}_k^\dagger \left(T e^{ik} + (T e^{ik})^* + O \right) \hat{a}_k \\ \hat{H} &= \sum_k \hat{a}_k^\dagger \left(\text{Re}(T e^{ik}) + \Omega \mathbb{1} \otimes \sigma_x + J \tau_x \otimes \mathbb{1} + \mu \tau_z \otimes \mathbb{1} \right) \hat{a}_k.\end{aligned}\tag{I.9}$$

The Hamiltonian is written as direct sum of 4×4 blocks corresponding to different momenta k . The diagonalization of

$$\tilde{\epsilon}_k = \left(\text{Re}(T e^{ik}) + \Omega \mathbb{1} \otimes \sigma_x + J \tau_x \otimes \mathbb{1} + \mu \tau_z \otimes \mathbb{1} \right), \tag{I.10}$$

thus yields four (in general different) solutions ϵ_k for each k . Up to now, we did not choose any basis for the spin σ and pseudospin τ degree of freedom, which allows to restrict to cases $\Omega > 0$ and $J > 0$. Explicitly, this holds true since

$$[\sigma_i, \sigma_j] = 2i \epsilon_{ijk} \sigma_k, \quad [\tau_i, \tau_j] = 2i \epsilon_{ijk} \tau_k \quad \forall i, j \in \{x, y, z\} \tag{I.11}$$

and hence $\sigma_z \tilde{\epsilon}_k(\Omega) \sigma_z = \tilde{\epsilon}_k(-\Omega)$ which is similarly valid for J . By observation, we have an anti-unitary map given by $\mathcal{T} := \sigma_x$ that can be interpreted as time reversal symmetry which transforms

$$\sigma_x \tilde{\epsilon}_k \sigma_x = \tilde{\epsilon}_{-k}^*. \tag{I.12}$$

The composition $\mathcal{C} := \tau_y \otimes \sigma_y$ has a somewhat peculiar property

$$\mathcal{C} \tilde{\epsilon}_k \mathcal{C}^\dagger = -\tilde{\epsilon}_{-k}^*, \tag{I.13}$$

that refers to a particle-hole character of the Hamiltonian. These two symmetries assign the Hamiltonian to the topological class **BDI** which shows a chiral property when we evaluate the action of $\mathcal{P} := \mathcal{C}\mathcal{T}$

$$\mathcal{P} \tilde{\epsilon}_k \mathcal{P}^\dagger = -\tilde{\epsilon}_k. \tag{I.14}$$

If we project the Fourier transformed components of the Hamiltonian $\tilde{\epsilon}_k$ to the normalized eigenbasis of \mathcal{P} , we achieve an 4×4 off-diagonal matrix that reads

$$\tilde{\epsilon}_k = \begin{pmatrix} 0 & A \\ A^\dagger & 0 \end{pmatrix} \tag{I.15}$$

with a 2×2 matrix A that satisfies $A^\dagger = A^*$ and has the explicit form

$$A := \begin{pmatrix} -iJ - \mu - 2t \cos(B/2 - k) & \Omega \\ \Omega & iJ - \mu - 2t \cos(B/2 + k) \end{pmatrix}. \tag{I.16}$$

The eigenvalues of this A matrix as a function of k return the dispersion relation of the four bands of the system. We notice that, due to the mentioned chiral symmetry (and the structure of Eq. I.15), we are bound to have two pairs of

opposite values. Since we are focusing on the half-filled system (i.e., all of the negative modes are occupied), if no zero eigenvalue is present, i.e., if $\det(A) \neq 0$, then the system exhibit an excitation gap. Furthermore, we recognize a symmetry $B \rightarrow B + 2\pi$ which maps $t \rightarrow -t$. Since $t \rightarrow -t$ only flips the sign of the cosine dispersion, thus only shifts the position of k in momentum space and not the overall energy, we may as well restrict to $B \leq 2\pi$ (as it would indicate from the flux per plaquette). Following [16], the complex phase $\xi(k)$ of this determinant gives rise to a topological invariant (spin winding number) that may distinguish between trivial and topological regions. This invariant is defined only for PBC. The proper self consistency condition to arrive at PBC reads

$$\hat{a}_1 = \hat{a}_{L+1} \quad (\text{I.17})$$

which is only satisfied, if $1 = e^{ikL}$, yielding a discretization of $k \in \mathbb{Z} \cdot 2\pi/L$. Since the dependence on k in the Hamiltonian appears in a function which is 2π symmetric anyhow, we further restrict k to L points in the interval $[-\pi, \pi]$. The phase $\xi(k)$ of the determinant of A is defined as

$$\det(A) = |\det(A)| e^{\pi i \xi}, \quad (\text{I.18})$$

which leads to a solution for

$$\tan(\xi) = \frac{4tJ \cos\left(\frac{B}{2}\right) \cos(k)}{J^2 - \Omega^2 + (\mu + 2t \cos\left(\frac{B}{2} - k\right)) (\mu + 2t \cos\left(\frac{B}{2} + k\right))}. \quad (\text{I.19})$$

Let us analyze in detail properties of this quantity $\mathcal{W} = \text{sign}\left(\frac{\tan \xi(0)}{\tan \xi(-\pi)}\right) \in \{\pm 1\}$. In this expression, the dependence of the numerator in Eq. 1.19 cancels, yielding

$$\mathcal{W} = \text{sign}\left(\frac{J^2 - \Omega^2 + (\mu + 2t \cos\left(\frac{B}{2}\right))^2}{J^2 - \Omega^2 + (\mu - 2t \cos\left(\frac{B}{2}\right))^2}\right). \quad (\text{I.20})$$

The two phase transitions where \mathcal{W} changes its sign appear at

$$\Omega^2 \in \left\{ J^2 + \min_{\max} \left(\mu \pm 2t \cos\left(\frac{B}{2}\right) \right)^2 \right\}. \quad (\text{I.21})$$

The phase diagram along Ω is shown in Fig. 4. Let $\vec{\Sigma}$ be defined as

$$\vec{\Sigma}(k) := \frac{1}{2} \hat{a}_k^\dagger (\mathbb{1} \otimes \vec{\sigma}) \hat{a}_k \quad \vec{\sigma} := (\sigma_x, \sigma_y, \sigma_z)^T. \quad (\text{I.22})$$

The spin winding number \mathcal{S} is defined as the number of rotations of the spin expectation value $\left\langle \sum_k \vec{\Sigma}(k) \right\rangle$ around the axes origin. Since topological nontrivial behavior (if any) is expected to appear for the second- and third-lowest energy band, the spin winding number \mathcal{S}_2 of a state filling only and exclusively the second band yields topological signatures [17]. It can be rigorously shown that the parities of $(-1)^{\mathcal{S}_2}$ and \mathcal{W} coincide for all phase regions. Therefore \mathcal{W} serves as a topological invariant to distinguish between trivial and topological phases. To obtain an expression for the spin winding number, one needs to evaluate the proper eigenstates of $\tilde{\epsilon}_k$. Since the derivation of the analytic expression for \mathcal{S}_2 is rather technical and requires a lot of book-keeping, we refer the interested reader to details in [13].

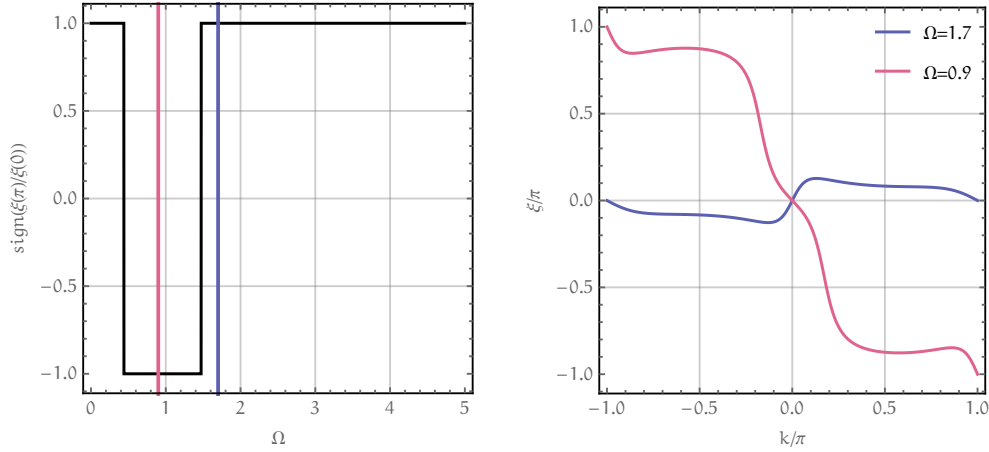


Figure 4: (Left) Shape of \mathcal{W} driving through Ω for fixed $B = \frac{4\pi}{3}$, $t = 1$, $J = 0.4$, $\mu = 0.8$. (Right) When going from edge to edge in the Brillouin zone, \mathcal{W} distinguishes between trivial and topological regions due to a winding of ξ . Whereas in topological systems the determinant of the Hamiltonian accumulates a nonzero phase, ξ vanishes for trivial parameter settings.

1.3 DISPERSION RELATION

In the next sections we are going to exploit exact solutions to find expressions and characteristics for observables in the non-interacting case which might be useful to distinguish topological from non-topological phases in the interacting cases as well. Let us stress that the following sections (apart from Fig. 6), have not been subject in publication [13].

Using four different species which correspond to different spacial and spin alignments, we arrive at a set of four different energy bands $\vec{\omega} = (\omega_1, \dots, \omega_4)^T$, that show topological features such as energy zero modes and nontrivial spin-winding numbers in states that correspond to a superposition of modes living in the second and third band.

We start at Eq. I.15 to derive an analytic expression for the dispersion relation $\vec{\omega}(\mathbf{k})$ by evaluating the eigenvalues of $A^\dagger A$. The eigenvalues of $A^\dagger A$ relate directly to the two different eigenvalues $\omega_\pm^2(\mathbf{k})$ of \hat{H}^2 , since

$$\hat{H}^2 = \begin{pmatrix} AA^\dagger & 0 \\ 0 & A^\dagger A \end{pmatrix} \quad (\text{I.23})$$

and because of the properties of A , we know that $A^\dagger A$ and AA^\dagger share the same set of eigenvalues

$$\rho(A^\dagger A) \subset \mathbb{R} \Rightarrow \rho(A^\dagger A)^* = \rho(AA^\dagger) = \rho(A^\dagger A). \quad (\text{I.24})$$

This yields the dispersion relation

$$\omega_\pm^2(\mathbf{k}) = J^2 + \Omega^2 + a_1^2(\mathbf{k}) + a_2^2(\mathbf{k}) \pm 2\sqrt{\Omega^2(a_2^2(\mathbf{k}) + J^2) + a_1^2(\mathbf{k})a_2^2(\mathbf{k})} \quad (\text{I.25})$$

where

$$\alpha_1(k) := 2t \sin\left(\frac{B}{2}\right) \sin(k), \quad \alpha_2(k) := \left(2t \cos\left(\frac{B}{2}\right) \cos(k) + \mu\right). \quad (\text{I.26})$$

In turn, this means that the four components of $\vec{\omega}(k)$ are given by the four combinations of $\pm\sqrt{\omega_{\pm}^2(k)}$. It is therefore sufficient to plot only the positive or negative part of the energy spectrum to fully classify the dispersion relation.

Fig. 5 shows the influence on the energy bands, when turning on different parameters. Having only nearest neighbor hopping of strength t and all other transitions turned off, the dispersion relation ends up with only two different energy bands $\pm|2t \cos(k)|$ that are each doubly degenerate, i.e. $\omega_1 = \omega_2$ and $\omega_4 = \omega_3 = -\omega_1$.

The interchain-tunneling (J) opens a total gap between bands $\omega_{1/2}$ and $\omega_{4/3}$ (top left). Spin-flips (Ω) induce an additional energy difference between $\omega_{1/4}$ and $\omega_{2/3}$ (top right). The effective potential μ controls the total occupation imbalance between different τ species, resulting in a deformation of all four bands (bottom left). With the strength of the flux per plaquette B , we are able to control the relative phase between the two cosii, eventually driving the system from trivial to topological phase (bottom right). The relative phase induced via B can be most easily seen when considering $\Omega = 0$, because the dispersion relation then reads fully simplified

$$\omega_{\pm}^2 \Big|_{\Omega=0} = J^2 + \left(\mu + t \cos\left(\frac{B}{2} \pm k\right)\right)^2. \quad (\text{I.27})$$

For the solution of the dispersion relation we assume PBC - causing all momenta in the Fourier space to be real numbers. This is not necessarily true for open systems in general, which causes solving a model considering other than periodic boundaries to be a very demanding problem itself.

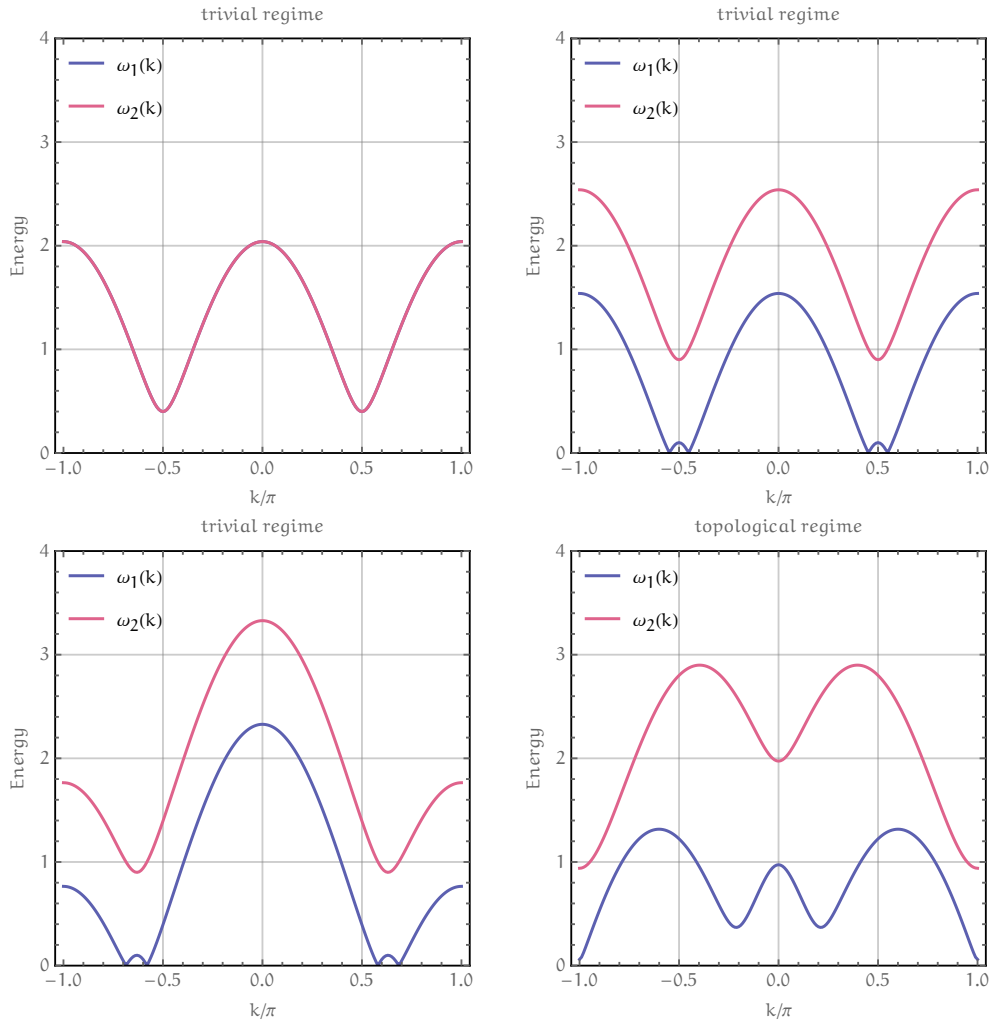


Figure 5: Dispersion relation changing parameters from 0 to a certain value for a system with PBC in the thermodynamic limit. Top left to bottom right - $J = 0.4$, $\Omega = 0.5$, $\mu = 0.8$, $B = \frac{4\pi}{5}$. We only printed the shape of ω_1 and ω_2 since $\omega_3 = -\omega_2$ and $\omega_4 = -\omega_1$. At the top of each panel, we explicitly state whether the system is trivial or topological. This property cannot be seen from the dispersion relation only, instead, we calculate for each setting \mathcal{W} to evaluate the phase.

For this specific problem, we have a rather simple form of the Hamiltonian \hat{H} being quadratic in creation and annihilation operators, meaning we can write all terms as linear combinations of vector components with a $4L \times 4L$ matrix H

$$\hat{H} = \vec{c}^\dagger H \vec{c}. \quad (\text{I.28})$$

The vector \vec{c}^\dagger contains all $4L$ single fermionic creation operators $\hat{c}_{r,\tau\sigma}^\dagger$, i.e.

$$\vec{c}^\dagger := \left(\hat{c}_{1,++}^\dagger, \hat{c}_{1,+ -}^\dagger, \dots, \hat{c}_{L,- +}^\dagger, \hat{c}_{L,--}^\dagger \right). \quad (\text{I.29})$$

Consequently, using a brute force diagonalization procedure on H , it is quite efficient to evaluate the eigensystem to arbitrary precision for large systems.

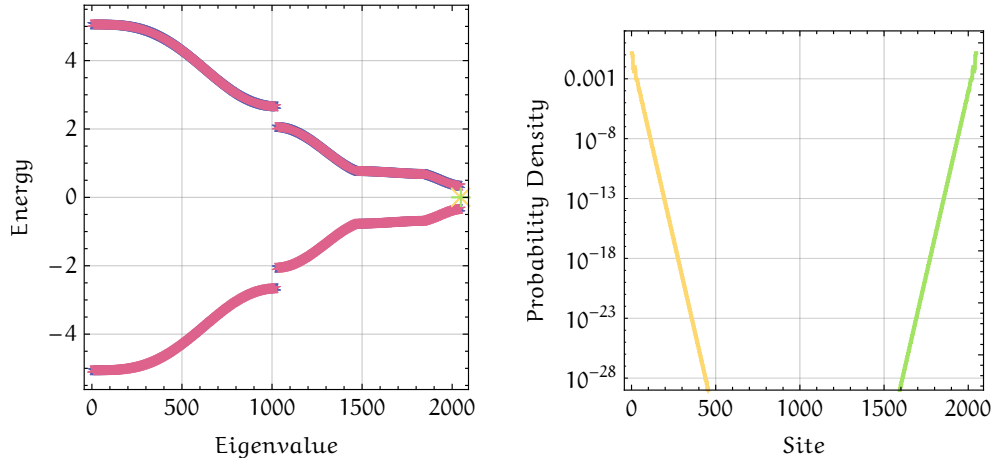


Figure 6: Eigenmodes and eigenvalues of the Hamiltonian assuming $t = 1$, $B = \frac{\pi}{2}$, $J = 1$, $\mu = 1$, $\Omega = 1.5$ for a total size $L = 512$. Left figure - Eigenvalues of H for **PBC** (red crosses) and **OBC** (blue crosses). The topological regime shows under **OBC** two eigenvalues $\epsilon_{1/2}^0$ with energy zero (yellow and green). The right figure shows the probability density profiles (on a logarithmic scale) of two single-mode states corresponding to the two zero-energy eigenvalues, respectively. We see that the two modes are located either at the left or right edge.

In Fig. 6, we show all eigenvalues for a system in the topological regime of length $L = 512$. The red crosses are eigenvalues for **PBC**, whereas the blue ones represent **OBC**. Interestingly, for **OBC** there appear two energy zero modes, that have the shape of boundary modes, which is why we explicitly highlighted those two modes with corresponding eigenvalues in yellow and green. The existence of such modes is not by chance. In particular, for *all* topological regimes which are distinguished from trivial ones by the topological invariant \mathcal{W} , these two boundary modes are present. The right plot in Fig. 6 shows the probability density profiles of two single mode states - each boundary mode is exponentially localized at one of the two borders while showing vanishing probability density on the other. In this sense, the boundary modes show a "chiral" property. Upon reflecting on the central position of the system, they map into each other. Such modes in the context of topological systems have many promising properties such as stability against local perturbations, but for now, we will not exploit and characterize their robustness. Another consequence of their presence is that

we have a four-fold degeneracy of the ground state, since we can either occupy or not each of the two edge modes (in general, k pairs of edge modes give 2^k degeneracy).

The ground state energy is always the sum of the lowest $2L$ eigenvalues. Let us define the energy difference $\Delta E_j = E_j - E_0$ of energies E_j of excited states with respect to the ground state energy E_0 . To achieve the excitation spectrum for the non-interacting system (without degeneracies), we can evaluate the sum of all possible combinations of $N = 2L$ eigenvalues. In order to save a bit of time, this procedure can be accelerated by summation of the lowest $2N - k$ values and evaluating all possible contributions of k of the remaining $2L + k$ eigenvalues (although we may lose information about the degeneracies of the spectral lines).

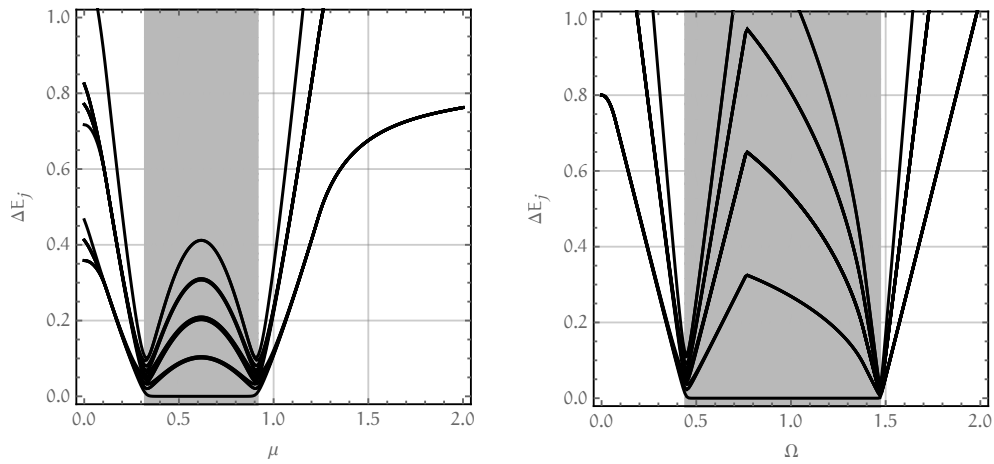


Figure 7: Energy spectrum of some low-excited states for $L = 396$, $t = 1$, $B = 4\pi/5$, $J = 0.4$ and $\Omega = 0.5$ (left), $\mu = 0.8$ (right). Topological phases are highlighted in grey. We can distinguish the two phases when we look at $\Delta E_1 = E_1 - E_0$ being the energy difference of the first excited state which is zero in the topological and nonzero in trivial phases. $\Delta E_2 = E_2 - E_0$ is zero at the topological borders and nonzero in the topological region. In fact, all further ΔE_j go to zero thus showing that the gap of the system closes at topological borders and opens again in the topological regime.

Fig. 7 shows the lowest single particle excitation gaps along a variation of certain parameters by keeping others fixed. It is clear that the energy of the ground state is degenerate in the topological regime due to the appearance of both boundary modes. However since we only have two boundary modes with energy zero, all other single particle excitations will be nonzero, when we keep the total number of particles fixed. Again, this is a consequence of topological edge states at zero energy, since they can appear or disappear only if the gap of the system is closing at the topological borders. We observe this by the fact that all of the displayed low-lying excitations tend to go to zero at the phase boundaries. This can be noticed in Fig. 7.

I.4 ENTANGLEMENT ENTROPY

Entanglement entropies in general provide a quite successful tool visualizing nonlocal (and nonclassical) correlations between subparts of the system. This property can be understood when considering a particular example:

The reduced density matrix of a state with common orthonormal basis $|\psi\rangle$ of two systems A and A^C is defined as the partial trace of the common density matrix $\rho = \rho_A \otimes \rho_{A^C}$,

$$\rho_{A/A^C} \equiv \text{tr}(\rho)_{A^C/A} . \quad (\text{I.30})$$

This can be simplified using the Schmidt decomposition to

$$\rho_A = \sum_{\alpha=1}^r \lambda_{\alpha}^2 |\alpha\rangle_A \langle\alpha|_A , \quad \rho_{A^C} = \sum_{\alpha=1}^r \lambda_{\alpha}^2 |\alpha\rangle_{A^C} \langle\alpha|_{A^C} . \quad (\text{I.31})$$

The von Neumann entanglement entropy (VNEE) is then computed from reduced density matrix ρ_{A/A^C}

$$\begin{aligned} S_{A/A^C} &\equiv -\text{tr} \left(\rho_{A/A^C} \ln \left(\rho_{A/A^C} \right) \right) \\ &= -\sum_{\alpha}^r \lambda_{\alpha}^2 \ln(\lambda_{\alpha}^2) . \end{aligned} \quad (\text{I.32})$$

If we consider the singlet state of two spin-1/2, $|\psi^{-}\rangle = \frac{1}{\sqrt{2}} (|\uparrow\downarrow\rangle - |\downarrow\uparrow\rangle)$, the total state can be written in matrix form

$$\begin{aligned} |\psi\rangle &= \sum_{a,b} \Sigma_{a,b} |ab\rangle \quad a, b \in \{\uparrow, \downarrow\} , \text{ with} \\ \Sigma &= \frac{1}{\sqrt{2}} \begin{pmatrix} 0 & 1 \\ -1 & 0 \end{pmatrix} . \end{aligned} \quad (\text{I.33})$$

A readout of the entanglement spectrum can be obtained by singular value decomposition

$$\begin{aligned} \Sigma &= U \Lambda V^{\dagger} = \frac{1}{\sqrt{2}} \begin{pmatrix} 0 & 1 \\ 1 & 0 \end{pmatrix} \begin{pmatrix} 1 & 0 \\ 0 & 1 \end{pmatrix} \begin{pmatrix} -1 & 0 \\ 0 & 1 \end{pmatrix} \\ &\Rightarrow -\Lambda^2 \ln(\Lambda^2) = \begin{pmatrix} 0.5 & 0 \\ 0 & 0.5 \end{pmatrix} \\ &\Rightarrow S = +1 , \end{aligned} \quad (\text{I.34})$$

which is the maximum entanglement entropy for this system. Since a singlet state is not separable, it is entangled and shows a nonzero VNEE. In contrary for separable states, e.g. $|\psi\rangle = \frac{1}{\sqrt{4}} (|\uparrow\rangle + |\downarrow\rangle) \otimes (|\uparrow\rangle + |\downarrow\rangle)$, the expression becomes

$$\Sigma = \frac{1}{\sqrt{4}} \begin{pmatrix} 1 & 1 \\ 1 & 1 \end{pmatrix} = U \Lambda V^{\dagger} = \frac{1}{\sqrt{4}} \begin{pmatrix} -1 & -1 \\ -1 & 1 \end{pmatrix} \begin{pmatrix} 1 & 0 \\ 0 & 0 \end{pmatrix} \begin{pmatrix} -1 & -1 \\ -1 & 1 \end{pmatrix} , \quad (\text{I.35})$$

which yields a **VNEE** $S = 0$. Thus, the **VNEE** is a direct measure for bipartite entanglement between subsystem A and A^C .

We will now compute the analytic version of the **VNEE** for a generic quadratic Hamiltonian to observe (possibly different) entanglement properties of the non-interacting system in Eq. I.3 between trivial and topological phases. To proceed, we have to determine the eigenvalues of the density matrix and calculate the entanglement spectrum. The starting point is an alternative formulation of the density operator, correctly defined at exactly *temperature zero*

$$\rho := \frac{e^{-\hat{H}}}{Z_H}, \quad (\text{I.36})$$

which is *not a thermal representation*, but instead a *highly nontrivial conclusion from careful observations about the ground states of quadratic Hamiltonians* [18]. Similarly, the form of the reduced density matrix of any subspace A containing the first l_A sites reads

$$\rho_A := \frac{\text{tr} \left(e^{-\hat{H}} \right)_A}{Z_A}, \quad (\text{I.37})$$

where the complementary states not living in A are traced out and Z_A is the partition function of subsystem A . The exponential of \hat{H} yields an infinite set of combinations of creators and annihilators, which makes its trace hard to evaluate directly. Fortunately, we can use the Wick-theorem which states for any correlation function that it can be expressed as a product of two-point correlators

$$C_{jk} := \langle a_j^\dagger a_k \rangle, \quad F_{jk} := \langle a_j a_k \rangle. \quad (\text{I.38})$$

Since \hat{H} conserves the number of particles, we know that any F_{ij} has to vanish. Moreover, the form of the trace can be simplified to

$$\text{tr} \left(e^{-\hat{H}} \right)_A = e^{-\hat{H}_A}, \quad (\text{I.39})$$

with \hat{H}_A being of a similar structure as \hat{H}

$$\hat{H}_A = \sum_i^{l_A} \sum_j^{l_A} a_i^\dagger h_{ij} a_j, \quad (\text{I.40})$$

but of course, $h_{ij} \neq H_{ij}$ in general. Using a unitary transformation V of dimension $l \times l$ that diagonalizes $h = V^\dagger \Lambda V$, we can further simplify Eq. I.41 to

$$\rho_A = \prod_{m=1}^{l_A} \frac{e^{-\epsilon_m d_m^\dagger d_m}}{Z_A}, \quad (\text{I.41})$$

where we introduced a set of new modes $d_m := (V\vec{a})_m$. The normalization through the partition function factors in a similar way to

$$Z_A = \prod_{m=1}^{l_A} Z_A(m) \quad Z_A(m) = 1 + e^{-\epsilon_m}. \quad (\text{I.42})$$

By definition, we can calculate any two-point correlator with help of the reduced density matrix via

$$C_{jk} := \langle a_j^\dagger a_k \rangle = \text{tr} \left(\rho_A a_j^\dagger a_k \right), \quad (\text{I.43})$$

which is the crucial point connecting two-point correlators of the whole system to the reduced density matrix of any subsystem A . When we use the expression for ρ_A , we have

$$C_{jk} = Z_A^{-1} \sum_{n=1}^{l_A} \sum_{p=1}^{l_A} V_{jn}^* V_{kp} \text{tr} \left(\prod_m e^{-\epsilon_m d_m^\dagger d_m d_n^\dagger d_p} \right). \quad (\text{I.44})$$

We distinct the factors carefully and simplify the trace from above to

$$\text{tr} \left(\prod_m e^{-\epsilon_m d_m^\dagger d_m d_n^\dagger d_p} \right) = Z_{A \setminus \{n,p\}} \text{tr} \left(e^{-\epsilon_n d_n^\dagger d_n} e^{-\epsilon_p d_p^\dagger d_p} d_n^\dagger d_p \right). \quad (\text{I.45})$$

We notice that for all cases $n \neq p$, the trace cancels to zero. This means we are left with a single factor where $n = p$ and have

$$Z_{A \setminus \{n\}} \text{tr} \left(e^{-\epsilon_n d_n^\dagger d_n} d_n^\dagger d_p \right) \delta_{np} = Z_{A \setminus n} e^{-\epsilon_n} \delta_{np}. \quad (\text{I.46})$$

Applying this to Eq. I.44, we achieve

$$C_{jk} = \sum_{n=1}^{l_A} \frac{Z_{A \setminus n}}{Z_A} V_{jn}^* V_{kn} e^{-\epsilon_n} = \sum_n \frac{1}{1 + e^{\epsilon_n}} V_{kn} V_{jn}^*. \quad (\text{I.47})$$

We know that V is self-orthogonal, which means that

$$\xi_n := (1 + e^{\epsilon_n})^{-1} \quad (\text{I.48})$$

are the eigenvalues of C_{jk} . Fortunately this expression is invertible for all $\xi_j > 0$, which means that the energies ϵ_j of subsystem A read

$$\epsilon_j = \ln \left(\frac{1 - \xi_j}{\xi_j} \right). \quad (\text{I.49})$$

Consequently, by diagonalization of C we are directly able to evaluate all $\epsilon_j \in \mathbb{R}$ [19]. Using a vector \vec{n} labelling the occupation of a local site $(\vec{n})_j = d_j^\dagger d_j$ we could systematically construct an analytic expression of ρ_A , but we are more interested in the systems entanglement properties. Throughout the history of quantum computation there was need for many different ways in how to quantify entanglement as almost every definition applies best for a certain set of problems and might be horribly suited for others.

In the community of one-dimensional tensor networks the most common quantity is the von Neumann entanglement entropy and the entanglement spectrum. In terms of quantum information, the [VNEE](#) represents a metric for the amount of information stored in the system. We are able to give an analytic expression for

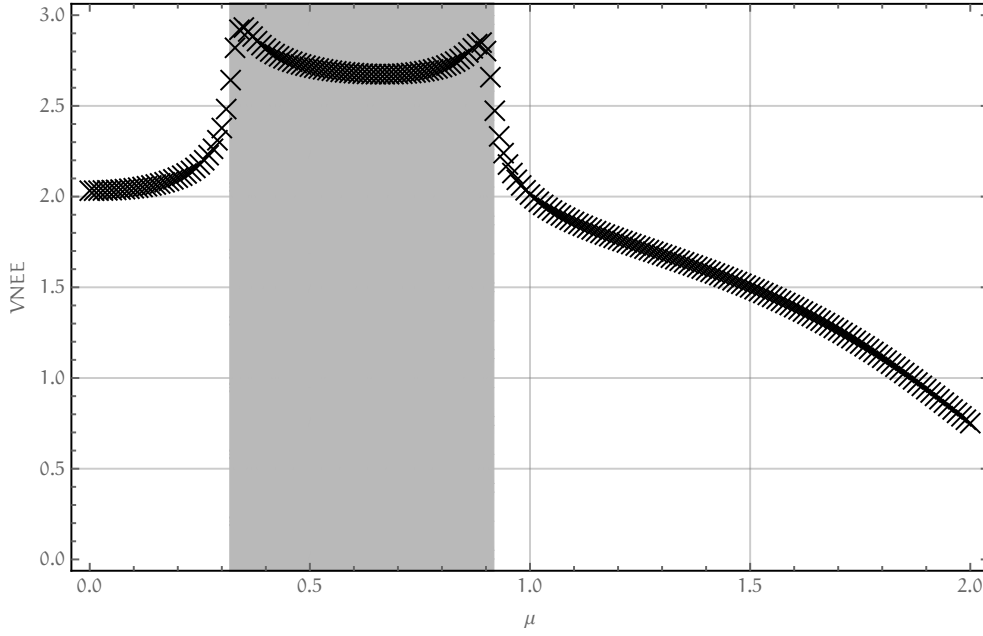


Figure 8: $L = 396$, $t = 1$, $B = 4\pi/5$, $J = 0.4$ and $\Omega = 0.5$. Von Neumann entanglement entropy with natural logarithm of the reduced system A assuming a size $l_A = L/2$. The plateau of maximum entropy in the topological region arises due to the four-fold degeneracy of the ground state (see also Fig. 9).

the von Neumann entanglement entropy and the spectrum that show non-trivial and distinct features between topological and trivial phase (see Fig. 8 and Fig. 9). Its definition relies on the eigenvalues $\lambda \in \mathcal{L}_A$ of the reduced density matrix

$$\mathcal{L}_A := \left\{ \lambda, \det(\lambda \mathbb{1} - \rho_A) = 0 \right\}. \quad (\text{I.50})$$

In entangled systems the set of eigenvalues can be very dense and it might be useful to analyze its (natural) logarithmic spectrum

$$\mathcal{S}_A := \{-\ln(\lambda), \lambda \in \mathcal{L}_A\}, \quad (\text{I.51})$$

that directly contributes to the von Neumann entanglement entropy defined as

$$S_A^{\text{VNEE}} := - \sum_{\lambda \in \mathcal{L}_A} \lambda \ln(\lambda). \quad (\text{I.52})$$

This dependence on the reduced density matrix and on its eigenvalues is exactly why the authority of the VNEE went hand in hand with the success of DMRG and other variational algorithms that rely on a truncation thereof.

Let \mathcal{N} be a set with 2^l elements, which are vectors that label all possible occupation configurations in subsystem A

$$\mathcal{N} := \{(n_j, j = 1, \dots, l), n_j \in \{0, 1\}\} \quad (\text{I.53})$$

Starting from Eq. I.41, we see that the density matrix has an operator representation with eigenvalues of the correlation matrix that depends on \vec{n}

$$\lambda(\vec{n}) = \prod_{m=1}^{l_A} \left(\frac{\xi_m}{1 - \xi_m} \right)^{n_m} (1 - \xi_m) =: \prod_{m=1}^{l_A} \alpha_m. \quad (\text{I.54})$$

The negative logarithm of this expression reads explicitly

$$S_A = - \sum_{m=1}^{l_A} \left(\ln \left(\frac{\xi_m}{1 - \xi_m} \right) n_m + \ln (1 - \xi_m) \right) =: - \sum_{m=1}^{l_A} \beta_m. \quad (\text{I.55})$$

Therefore, the von Neumann entanglement entropy becomes

$$S_A^{\text{VNEE}} = - \sum_{n_1=0}^1 \sum_{n_2=0}^1 \cdots \sum_{n_{l-1}=0}^1 \sum_{n_l=0}^1 \lambda(\vec{n}) \ln (\lambda(\vec{n})). \quad (\text{I.56})$$

Let us evaluate just one of all l_A sums

$$\begin{aligned} \sum_{n_j=0}^1 \lambda(\vec{n}) \ln (\lambda(\vec{n})) &= - \sum_{n_j=0}^1 \left(\prod_{m=1}^{l_A} \alpha_m \right) \left(\sum_{m=1}^{l_A} \beta_m \right) \\ &= - \prod_{m \neq j} \alpha_m \left(\sum_{m \neq j} \beta_m + (1 - \xi_j) \ln(1 - \xi_j) + \xi_j \ln \xi_j \right). \end{aligned} \quad (\text{I.57})$$

We know from Eq. I.41 and Eq. I.42 that α_j is normalized for a single site

$$\sum_{n_j=0}^1 \alpha_j = 1. \quad (\text{I.58})$$

Consequently, we are able to simplify all 2^{l_A} terms in the definition of the von Neumann entropy to only $2l_A$ constituents

$$S_A^{\text{VNEE}} = - \sum_{m=1}^{l_A} \left((1 - \xi_m) \ln(1 - \xi_m) + \xi_m \ln \xi_m \right). \quad (\text{I.59})$$

We have expressed analytically both the spectrum and the entropy in terms of eigenvalues of two-point correlation functions. In the following, we want to restrict subsystem A to contain sites $i_A = \{1, \dots, L/2\}$. This way, A is the leftmost half of the overall system and S_A is maximized. As a side mark, **VNEE** have become relevant also in experiments since there exist protocols to access them using local measurements to determine the overall and reduced density matrices [20].

In the von Neumann entropy S_A^{VNEE} exists a maximum entropy plateau in the topological phase, following from a supplemental amount of ground states. Looking at the spectrum for half of the system, we see that the largest eigenvalue is four-fold degenerate, in agreement with the overall degeneracy of the energy in *all* possible charge sectors. This seems contrary to the fact that we fix the total charge $N = 2L$, allowing only a two-fold degeneracy of the lowest energy. The reasoning behind this is due to the properties of the entanglement Hamiltonian \hat{H}_A of length l_A . When l_A is smaller than the total size of the system, the overall particle number is not a conserved quantity for subsystem A , $[\hat{H}, \hat{N}_A] \neq 0$. This allows for all four ground states in different charge sectors N to be ground states in the subsystem A , despite limiting the overall charge sector. As a consequence,

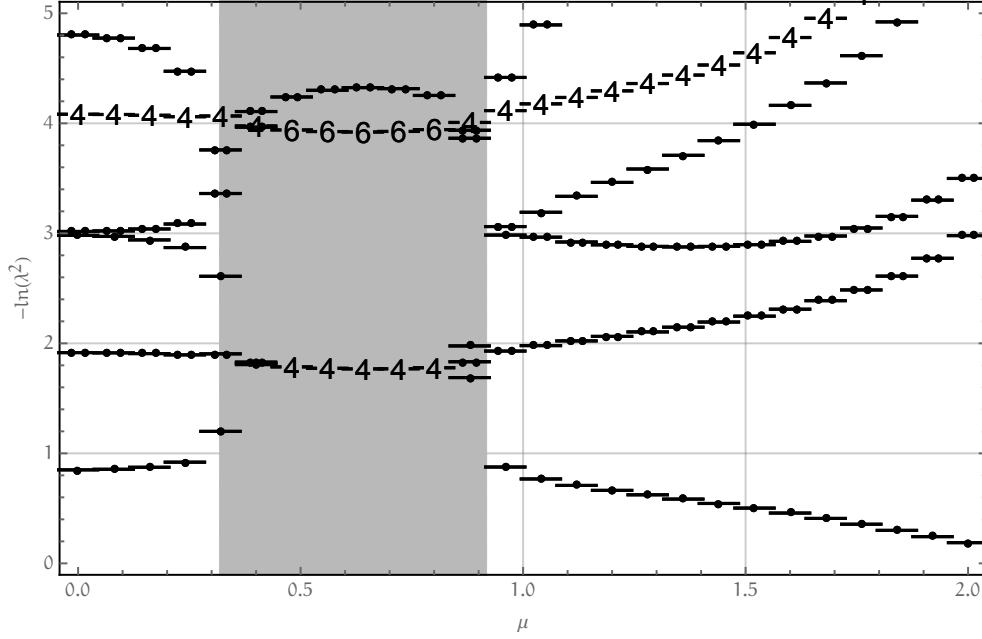


Figure 9: $L = 396$, $t = 1$, $B = 4\pi/5$, $J = 0.4$ and $\Omega = 0.5$. Eigenvalue spectrum of the reduced density matrix with $l_A = L/2$. For subsystem A , $[\hat{H}, \hat{N}_A] \neq 0$. This allows ground states of all charge sectors to be ground states of subsystem A , yielding a four-fold degeneracy of the energy spectrum and the entanglement spectrum as well. Imperfect degeneracy in the limiting regions of the topological regime are due to residual finite size effects which disappear in the thermodynamic limit.

the energy spectrum in subsystem A shows four-fold degeneracy, similarly the entanglement spectrum of \hat{H}_A .

The last part of this section is about general properties of entanglement entropy restricting to one-dimensional systems. Calabrese and Cardy studied the scaling of entanglement entropy in a (1+1)D (conformal) quantum field theory and proved that the continuum limit has a logarithmic dependence with respect to the size x of subsystem A [21].

For gapped, noncritical systems the entropy saturates when the subsystem size x approaches the finite correlation length ξ and stays constant for $x > \xi$ in leading order. Importantly, the scaling has an intrinsic dependence on the charge c of the conformal field theory that the model maps to at quantum critical points. The result is universal for all one-dimensional systems and reads

$$S_A(x) = \frac{c}{3b} \log \left(\frac{L}{\pi} \sin \left(x \frac{\pi}{L} \right) \right) + c' + \phi^c(x) \quad b = \begin{cases} 1 & \text{for PBC} \\ 2 & \text{for OBC} \end{cases} \quad (\text{I.60})$$

We account for oscillations in S caused by scattering of particles at impurities such as boundaries in finite size systems by introducing a bounded function $\phi^c(x)$. The conformal charge, roughly speaking, relates to the number of occupied bands in a model and hence quantifies the amount of Fermi points at a

given number of particles. In $c = 1$ theories, the leading oscillations run with frequency $2k_F$ [22] and contribute to the entanglement entropy via

$$\phi^1 = b_0 \cos(2k_f(x - L/2)) / \sin(x\pi/L)^{b_1}. \quad (\text{I.61})$$

By fitting the whole region in $c = 1$ theories, one can extract a reliable value of k_F . This is particularly useful in interacting cases when exact solutions of large clusters of particles are not available. For higher conformal charges, we have yet to elaborate the proper modulation of those oscillations that arises due to scattering of particles with different Fermi momenta. They are relevant here because the non-interacting four-leg ladder has gapless points with $c \in \{2, 4\}$. For large enough systems, it is possible to extract c by fitting just the asymptotic behavior of the entanglement spectrum neglecting the modulation $\phi^c(x)$. The procedure is usually elaborated introducing the scaled chord distance

$$d(x|L) := \frac{L}{\pi} \sin\left(x \frac{\pi}{L}\right) \quad (\text{I.62})$$

which maps the logarithmic scaling to a linear dependence on $\log(d(x|L))$. For the four-leg ladder, when we set $J = 0$ and $\Omega \ll t$, the system is gapless at half-filling. If we drive the system through different values μ , we face trivial and topological regions with $c = 2$ (topological) and $c = 4$ (trivial). Similarly, we want to regard asymptotic behavior of the two-leg ladder of $\tau = +$ species (neglect all $\tau = -$ contributions). For small spin-flip transitions $\Omega \ll t$, this system is critical everywhere. Screening all charge sectors, we encounter two distinct conformal charges, namely $c = 2$ for the trivial and $c = 1$ for the topological phase. Fig. 10 shows the asymptotic dependence of the entanglement entropies for both models at different points in n for a finite system of size $L = 256$. We see that the oscillations in the four-leg ladder are more dominant than in the two-leg ladder due to several scatterings on the enlarged border. We explicitly show that the non-interacting system features two different central charges corresponding to two distinct phases. These two regions will become important especially in Sec. 1.5, since the $c = 1$ phase corresponds to an integer quantum Hall (iQH) regime.

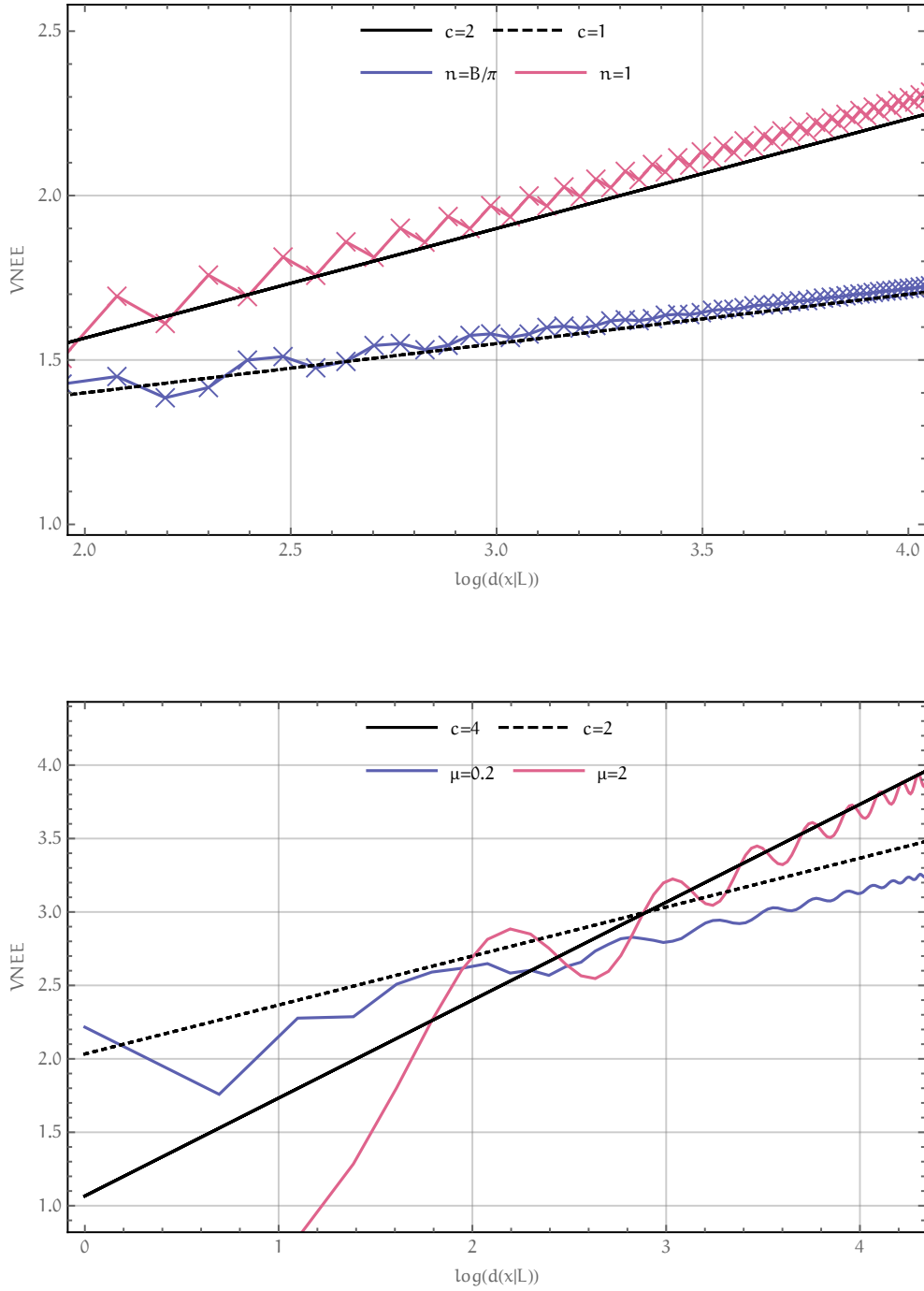


Figure 10: We included four entanglement scalings - the upper panel corresponds to the two-leg ladder, the bottom figure to the four-leg ladder. Screening the band structure with help of the asymptotic entanglement behavior, we see that the $c = 2|4$ scaling changes in the vicinity of $n = B/\pi$ to $c = 1|2$ due to the partial gap induced by nonzero Ω . We will elaborate suitable signatures of these two phases in detail in Sec. I.5.

1.5 CHIRAL CURRENTS

Recent works of Cornfeld and Sela show that chiral currents prove very useful when detecting QH phases. In particular, they use the chiral current as probe for the presence of topological states and show that it is possible to obtain fractional QH states via simple two-body interactions. They focus on a Hamiltonian considering a two-species ladder system of the form

$$\hat{H}_{\text{Single}} = \hat{H}_{\perp} + \hat{H}_{=} + \hat{H}_{\text{int}}, \quad (\text{I.63})$$

restricting to nearest neighbor hoppings with flux per plaquette B . The two constituents \hat{H}_{\perp} and $\hat{H}_{=}$ read explicitly

$$\hat{H}_{\perp} := \Omega \sum_j e^{iBj} \hat{a}_j^{\dagger} \sigma_x \hat{a}_j \quad \hat{H}_{=} := t \sum_j \hat{a}_j^{\dagger} \hat{a}_{j+1} + \text{H.c.} \quad (\text{I.64})$$

Here, we do not want to discuss the fractional cases (see instead Ch. II), and characterize the integer current resonance, which we obtain in both the non-interacting four- and two-leg ladder model. For fractional QH phases, the introduction of proper interactions is necessary, but for now we want to set $\hat{H}_{\text{int}} = 0$. This model considers only two fermionic species $\hat{a}_j = (\hat{c}_{r,+}, \hat{c}_{r,-})$ that distinct in a spin degree of freedom σ . \hat{H}_{Single} acquires the Peierl's phase along perpendicular hoppings as written in Eq. I.64. But one may change the gauge to \hat{H}'_{Single} , using a transformation $\hat{c}_{j,\sigma} \rightarrow e^{\sigma z i B / 2 \cdot j} \hat{c}_{j,\sigma}$ that yields

$$\begin{aligned} H'_{\perp} &= \Omega \sum_j e^{iBj} \hat{a}'_j{}^{\dagger} \sigma_x \hat{a}'_j = \Omega \sum_j \hat{a}'_j{}^{\dagger} \sigma_x \hat{a}'_j \\ H'_{=} &= t \sum_j e^{i\sigma z B / 2} \hat{a}'_j{}^{\dagger} \hat{a}'_{j+1} + \text{H.c.} \end{aligned} \quad (\text{I.65})$$

We note that this type of Hamiltonian is a special case of the four-leg ladder. If we assume inter-chain coupling to be $J = 0$ and set the potential difference $\mu = 0$, Eq. I.3 is an extension of Eq. I.63, representing two exact copies at two different degrees of freedom τ .

We will start to give a motivation about how to define currents in second quantization theories assuming only one species of fermions.

The current is defined as partial derivative of the total charge N with respect to time. Whenever N is a conserved quantity, the total time derivative $\frac{d}{dt}N = 0$ and we may apply the Ehrenfest theorem

$$\frac{\partial N}{\partial t} = \left\langle \frac{\partial \hat{N}}{\partial t} \right\rangle = i \left\langle [\hat{N}, \hat{H}] \right\rangle + \frac{dN}{dt} = i \left\langle [\hat{N}, \hat{H}] \right\rangle. \quad (\text{I.66})$$

Let us proceed assuming only *one* species of fermions \hat{a}_i^{\dagger}

$$i \left\langle \left[\hat{N}, \sum_l \hat{a}_l^{\dagger} \hat{a}_{l+1} e^{iB} + \text{H.c.} \right] \right\rangle = i \sum_j \left\langle \left[\hat{a}_j^{\dagger} \hat{a}_j, \sum_l \hat{a}_l^{\dagger} \hat{a}_{l+1} e^{iB} + \text{H.c.} \right] \right\rangle, \quad (\text{I.67})$$

We will focus on a single term

$$\begin{aligned} \left[\hat{a}_k^\dagger \hat{a}_k, \sum_l \hat{a}_l^\dagger \hat{a}_{l+1} e^{iB} + \text{H.c.} \right] &= it \left(\hat{a}_k^\dagger \hat{a}_{k+1} e^{iB} - \hat{a}_{k-1}^\dagger \hat{a}_k e^{iB} - \text{H.c.} \right) \\ &=: -\hat{j} \left(k + \frac{1}{2} \right) + \hat{j} \left(k - \frac{1}{2} \right), \end{aligned} \quad (\text{I.68})$$

and define local currents \hat{j}

$$\hat{j} \left(k + \frac{1}{2} \right) := -it \left(\hat{a}_k^\dagger \hat{a}_{k+1} e^{iB} - \text{h.c.} \right). \quad (\text{I.69})$$

By observation, \hat{j} is the negative partial derivative of \hat{H} with respect to B . This is the motivation for a more general definition of the chiral current which reads

$$j_c := -\frac{1}{L} \frac{\partial E}{\partial B} = -\frac{1}{L} \left\langle \frac{\partial \hat{H}}{\partial B} \right\rangle, \quad (\text{I.70})$$

where B is the flux per plaquette. The chiral current is a gauge-independent quantity and results from persistent charge fluxes in states as a consequence of nonzero magnetic fields.

We are particularly interested in features of this quantity, as it is shown in [12] to be sensitive to QH phases. I.e. for fQH and iQH regions at a certain density n_{res} , the chiral current shows a unique behavior. Because of the outstanding shape at small $\Omega \ll t$ with two peaks in the vicinity of $j_c(n_{\text{res}}) = 0$, we call those interesting points *current resonances*.

The dispersion of the free Hamiltonian visualized in Fig. 5 assuming $J = 0$ shows a current resonance at density $n = \frac{B}{\pi}$. This is due to Eq. I.3 being a system composed of two identical copies of Eq. I.63 in each τ -chain. This can be explained due to the topology of the energy bands. At density $n_F = \frac{B}{\pi}$, Ω induces a partial gap and the system remains critical. In this phase, the amount of Fermi points $\pm k_F$ reduces to one pair and the system shows a central charge $c = 1$. Outside of this partial gapped phase, $c = 2$ and there are two pairs of Fermi momenta (we already confirmed the central charges in Fig. 10). If $\Omega \ll t$, the model can be mapped to a Luttinger Liquid [12] with iQH phases at partial gapped fillings. It has been shown [12] that the chiral current and its resonances are consequences of the partial gap, induced by $\Omega \ll t$. The dependence of j_c in the non-interacting case reads explicitly

$$j_c \propto \left(n - \frac{B}{\pi} \right), \quad (\text{I.71})$$

with density n and flux per plaquette B . To verify this prediction, we have evaluated j_c both in the two-leg ladder assuming $\Omega \ll t$ and the four-leg ladder at $\Omega \ll t$ and $J \ll \Omega$

$$j_c^{4\text{leg}} = -\frac{t}{L} \text{Im} \left(\left\langle \sum_r \hat{a}_r^\dagger \tau_z \otimes \sigma_z e^{iB/2\sigma_z} \hat{a}_{r+1} \right\rangle \right). \quad (\text{I.72})$$

In two leg ladder systems exist only two components instead of four (neglect all $\tau = -1$ contributions)

$$j_c^{2\text{leg}} = -\frac{t}{L} \text{Im} \left(\left\langle \sum_r \hat{a}_r^\dagger \sigma_z e^{iB/2\sigma_z} \hat{a}_{r+1} \right\rangle \right). \quad (\text{I.73})$$

It is a quantity that measures a transition probability with respect to a specific type of particle. E.g. the electric current is defined as the direction to which a positron moves. Similarly, we define the chiral current with respect to $\tau\sigma = ++$ particles and have to introduce phases ± 1 to account for contributions from different types of species. We prepared figures that visualize the nearest neighbor hopping probabilities $\text{Im} \left\langle \hat{c}_{j,\tau\sigma}^\dagger \hat{c}_{j+1,\tau\sigma} e^{iB/2\sigma_z} \right\rangle$ for a small system in Fig. 11 and large systems in Fig. 13. The disks visualize the occupation of lattice vortices with label $(x, y) = (j, \tau\sigma)$. More transparency means less occupied. In between, the arrows correspond to the direction and amplitude of the intra-species transition probability. The color-code of plots and disks which distincts $\tau\sigma$ species coincide.

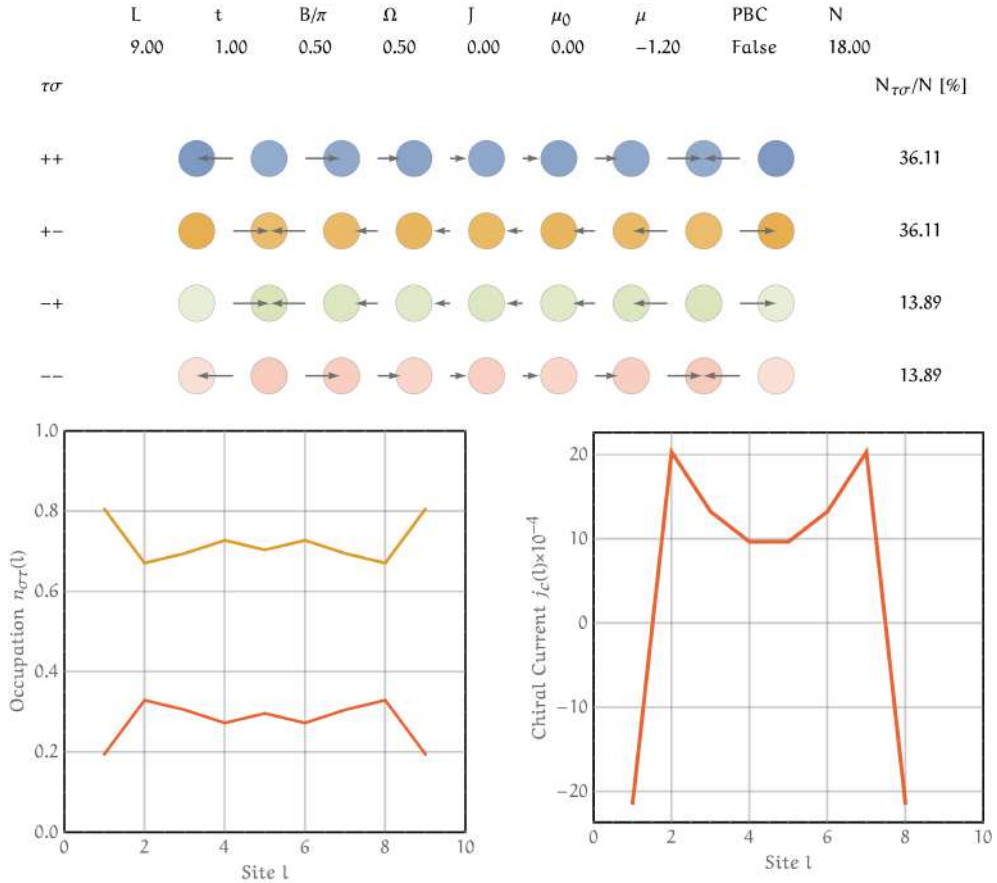


Figure 11: Visualization of expectation values of nearest neighbor hoppings and their contribution to the chiral current. For convenience, the two insets show the overall occupation per species $\hat{n}_{j,\tau\sigma} = \hat{c}_{j,\tau\sigma}^\dagger \hat{c}_{j,\tau\sigma}$, and the expectation value of the local current operator $j_c(j) = -\frac{t}{L} \left\langle \hat{a}_j^\dagger \tau_z \otimes \sigma_z e^{iB/2\sigma_z} \hat{a}_{j+1} \right\rangle$.

Both Hamiltonians are exactly solvable, and we can vary the total number of modes to be considered in order to elaborate different densities. A small system size (if not considering PBC) shows large oscillations in the current - see Fig. 11. For larger system sizes, the bulk shows a persistent current for both PBC and OBC.

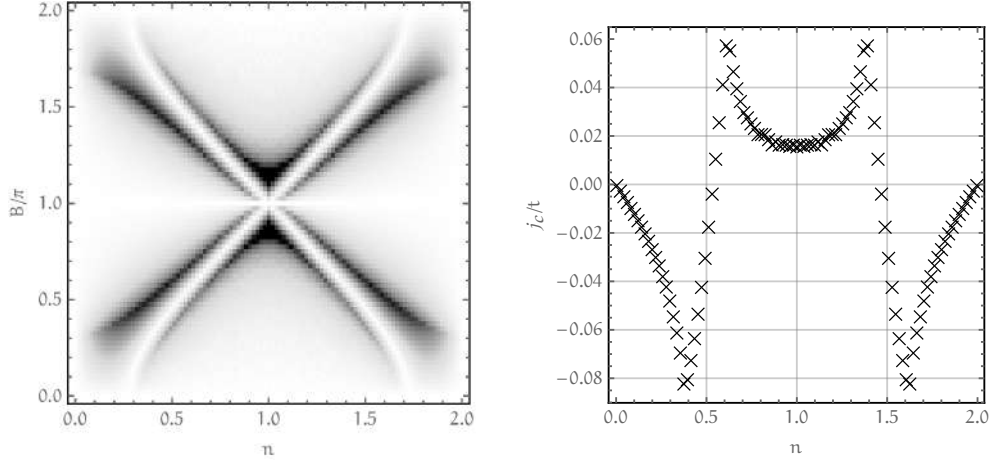


Figure 12: The figure on the left displays the absolute amplitude of the chiral current of the noninteracting two-leg ladder Hamiltonian in Eq. I.63 at $L = 256$ and $\Omega = 0.5$. The current shape for a horizontal slice at $B = 0.5\pi$ shows a resonance at density $n = B/\pi$ and is displayed on the right. Both figures are symmetric w.r.t $n = 1$ and we notice that the cases $n < 1$ and $\frac{B}{\pi} < 1$ are sufficient.

In case of the four leg ladder, it exists an explicit control of occupation imbalance between $\tau = +$ and $\tau = -$ chains using the potential difference μ . This becomes clear when we take the partial derivative of \hat{H} with respect to μ

$$\left\langle \frac{\partial \hat{H}}{\partial \mu} \right\rangle = \left\langle \sum_{\mathbf{r}} \hat{a}_{\mathbf{r}}^{\dagger} \tau_z \otimes \mathbb{1} \hat{a}_{\mathbf{r}} \right\rangle = N_{\tau=+} - N_{\tau=-} \quad (\text{I.74})$$

which returns exactly the overall difference in the number of τ -species. When we consider the case of half filling, the chiral symmetry exploited in Sec. I.2 provides a particle-hole character. This is clear for the limits $\mu \rightarrow \pm\infty$ which results in either one of the two τ chains being empty and the other one completely filled, meaning one may interpret occupation of sites in one chain as particles and particles in the other chain as holes. Keeping $J = 0$ and $N = 2L$ at half filling, this allows for varying through μ to observe in each τ chain exactly the same properties of the noninteracting Hamiltonian I.63 when varying through N . We prepared further visualizations of the local currents in Fig. 13.

Finally, the Hellman-Feynman theorem gives a relation between dispersion relation and expectation value of $\partial_{\mu} \hat{H}$

$$\frac{\partial E_{GS}}{\partial \mu} = \left\langle \partial_{\mu} \hat{H} \right\rangle, \quad (\text{I.75})$$

which we use to show the dependence of particle imbalance on Ω and J in Fig. 14.

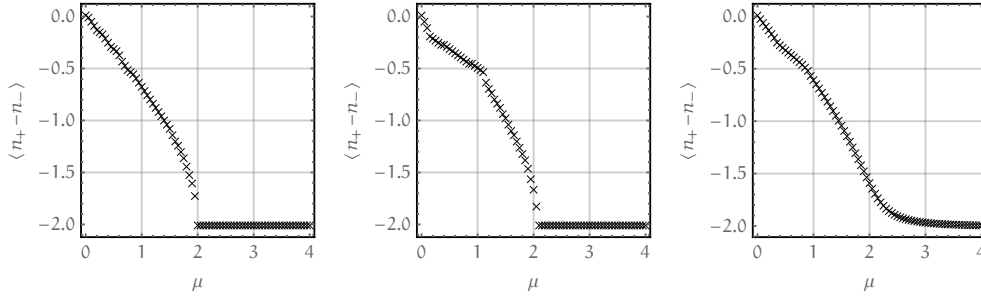


Figure 14: We control the density imbalance between τ_+ and τ_- chains with the effective potential μ . The left figure shows the bare imbalance control when $J = \Omega = 0$, the figure at the center shows $\Omega = 0.5$ and the right picture visualizes $J = 0.4$ and $\Omega = 0.5$, each one at fixed flux $B = 4\pi/5$ and $L = 198$.

This allows a map between density and effective potential $n \rightarrow \mu$, to express the position of current resonances for perturbative $\Omega \ll t$ and $J = 0$ in terms of μ

$$\mu_{\text{res}} = \pm 2 \cos\left(\frac{B}{2}\right). \quad (\text{I.76})$$

We prepared a plot that shows this equivalence in Fig. 17.

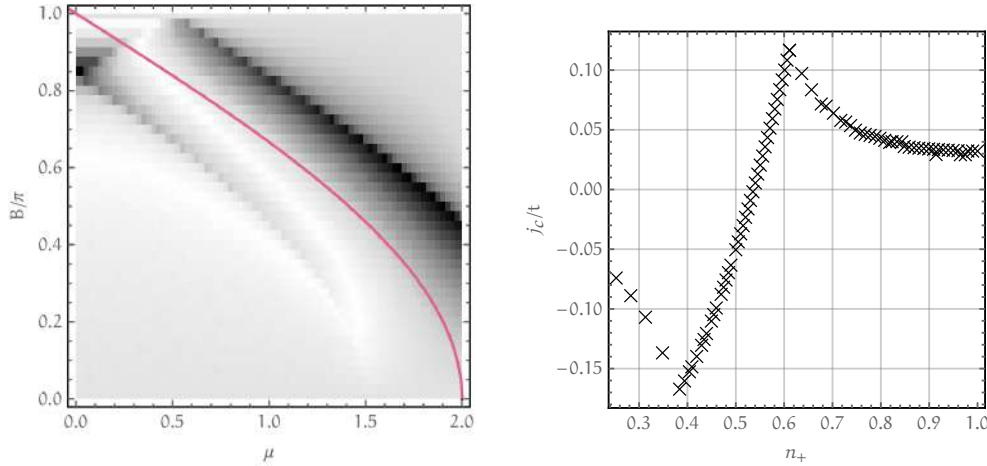


Figure 15: The figure on the left displays the absolute amplitude of the chiral current of the noninteracting four-leg ladder Hamiltonian in Eq. I.3 at $L = 198$ and $\Omega = 0.5$. The red line corresponds to the bare resonance condition of Eq. I.76. Translating back to local densities (right), it matches to twice the current in the corresponding two-leg ladder system.

We notice for intra-chain tunnelings $J = 0$, chiral currents in the four-leg ladder coincide apart a factor two to results in [12]. For $J = 0$, the four-leg ladder consists of two chains that are two-leg ladders, obeying an additional symmetry $[\hat{H}, \hat{N}_\tau] = 0$. This allows to factor \hat{H} into two individual commuting parts $\hat{H}_{\tau=+}$ and $\hat{H}_{\tau=-}$ that have distinct densities n_+ and n_- , controlled via μ . At half filling,

$$n_- = 2 - n_+ = \frac{2}{\pi} \arccos\left(-\frac{\mu}{2}\right). \quad (\text{I.77})$$

Due to the chiral nature of the current, $j_c(n_+) = j_c(2 - n_+)$ and because we are in the half-filling case, $2 - n_+ = n_-$, such that the sum $j_c(n_+) + j_c(n_-) = 2j_c(n_+)$.

Varying μ equidistantly, we naturally obtain a coarse grained resolution for small densities and a fine grained resolution for densities in the vicinity of 1. If necessary, a possible workaround is to choose $\cos(\mu\pi)$ equidistantly.

We now elaborate the current in the extended model with nonzero J . We know from solutions in momentum space, that J closes the partial gap induced from Ω when $J > \Omega$. This is why we conclude that the current persists for cases $J < \Omega$ and vanishes otherwise. We have prepared a detailed overview of the persistent chiral current in analogy to the previous pictures but for different values of J to visualize the predicted influence.

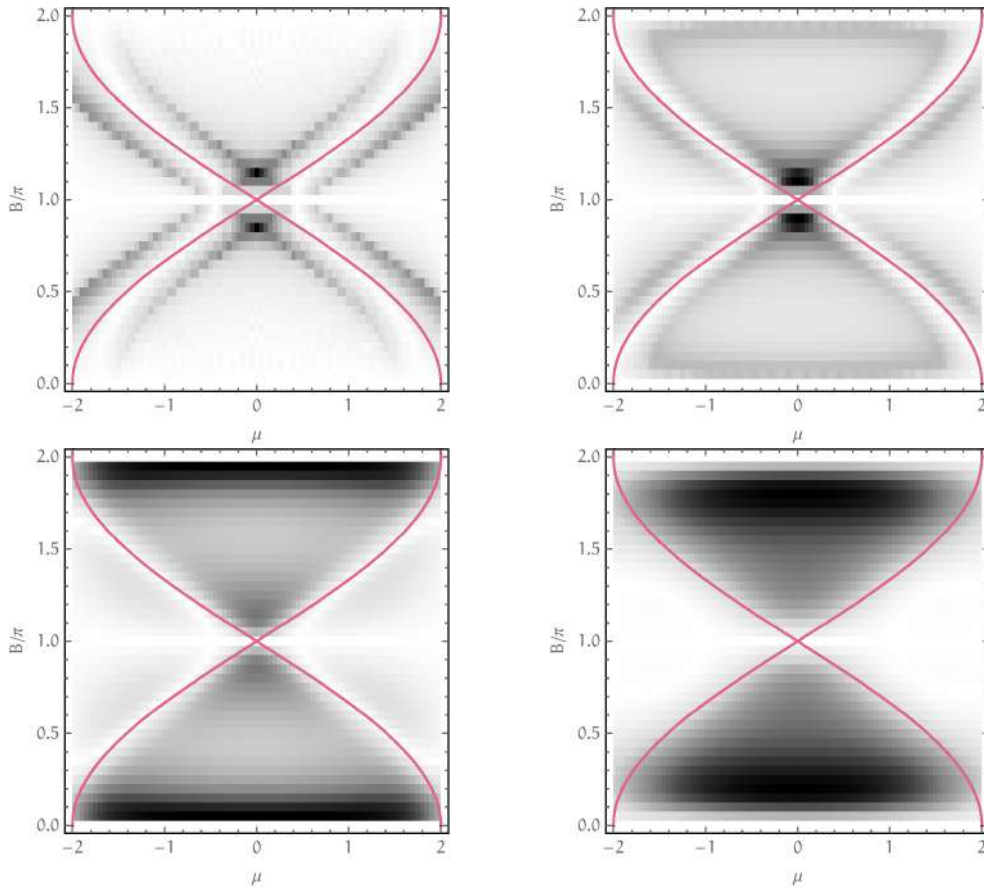


Figure 16: $L = 32, \Omega = 0.5$ and J varied from 0.01 (top left) to 0.3 (top right), 0.5 (bottom left) and 1.0 (bottom right). The typical double-cusp signature of the currents vanishes completely when $J \geq \Omega$.

A remarkable result is, if we utilize j_c as indicator for Luttinger liquid phases, it becomes "easy" to validate *iQH* phases numerically - even for system sizes that are far too small to see the asymptotic behavior of the entanglement entropy! This is why we hope, using the chiral current as a probe to observe similar fea-

tures in other setups, we might be able to "measure" the presence of fQH phases.

While we analyzed properties of the chiral current, we noticed a peculiar signature of a single contribution in momentum space, which we want to specifically expose in the next section.

I.6 MOMENTUM ZERO CURRENT

We observe that the chiral current operator, i.e. the momentum zero component serves as topological order parameter to distinguish iQH from trivial phases.

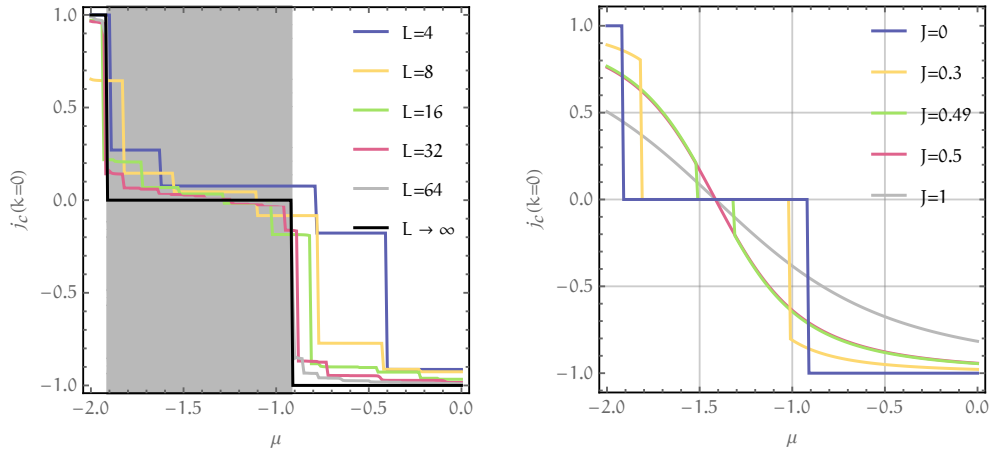


Figure 17: $L = 32$, $\Omega = 0.5$, $B = \pi$. The left and right figures show that the current serves as a topological order parameter in the thermodynamic limit when we assume $J \ll \Omega$. If J increases, we still have a jump of this current contribution when we enter the topological phase.

We can give an analytic expression in terms of eigenvalues of τ_z . Let us recall the explicit form of the momentum-zero component of the four-leg Hamiltonian in momentum space (assuming $\mu_0 = 0$ and $t = 1$)

$$\hat{H}(k=0) = \Omega\sigma_x + J\tau_x + \left(\mu + 2 \cos\left(\frac{B}{2}\sigma_z\right) \right) \tau_z. \quad (\text{I.78})$$

The partial derivative with respect to B yields

$$\hat{j}_c(k=0) = \frac{1}{2}\tau_z \otimes \sin\left(\frac{B}{2}\right), \quad (\text{I.79})$$

When we assume half-filling, the expectation value of \hat{j}_c is obtained by summing the ground state components of $\langle \hat{j}_c(k=0) \rangle$. From aspects of Sec. I.2 we notice that the ground state components in momentum space are indeed the ones occupying the two lowest bands. Since σ_z does not matter in the cosine, σ_x serves as quantum number. We may transform $\hat{H}(k=0)$ onto the eigenbasis of σ_x , such that the eigenvalues of σ_x become $\lambda(\sigma_x) = \pm 1$. Hence, the two lowest energy states $|\psi(k=0)\rangle_{1/2}$ are a product state of

$$|\psi(k=0)\rangle_i = |\varphi_{\pm}\rangle \otimes |\sigma_x = \pm 1\rangle. \quad (\text{I.80})$$

When apply a unitary transformation $U = e^{i\frac{\pi}{4}\tau_x}$, we have

$$U\hat{H}(k=0)U^\dagger = \Omega\sigma_x + J\tau_x + \left(\mu + 2\cos\left(\frac{B}{2}\right)\right)\tau_y \quad (\text{I.81})$$

and find two eigenstates upon diagonalization

$$|\varphi_\pm\rangle = \frac{1}{\sqrt{2}} \frac{1}{\sqrt{J^2 + (\mu + 2\cos(\frac{B}{2}))^2}} \begin{pmatrix} J - i(\mu + 2\cos(\frac{B}{2})) \\ \mp\sqrt{J^2 + (\mu + 2\cos(\frac{B}{2}))^2} \end{pmatrix}. \quad (\text{I.82})$$

We use the previous expression to evaluate $j_c(k=0)$ in the new basis

$$j_c(k=0)/\sin(B/2) = \frac{1}{2} (\langle\tau_y\rangle_1 + \langle\tau_y\rangle_2), \quad (\text{I.83})$$

finally arriving at

$$\langle\tau_y\rangle_\pm = \mp \frac{\mu + 2\cos(B/2)}{\sqrt{J^2 + (\mu + 2\cos(B/2))^2}}. \quad (\text{I.84})$$

The sign of $\langle\tau_y\rangle_\pm$ coincides with the sign of $|\varphi_\pm\rangle$. Since the eigenstates have energies $\pm\sqrt{J^2 + (\mu + 2\cos(B/2))^2} \pm \Omega$, we must distinguish between trivial and topological phases (without loss of generality, $\Omega > 0$, $\mu < 0$, $\cos(B/2) > 0$ and $J^2 < \Omega^2$):

- If we are in the topological phase, the two lowest energy eigenstates are $|\psi\rangle_{1/2} = |\varphi_\pm\rangle|\sigma_x = -1\rangle$. This means $j_c(k=0) = 0$.
- If we are in one of the two trivial phases, the lowest energy eigenstates are $|\psi\rangle_{1/2} = |\varphi_\pm\rangle|\sigma_x = \pm\rangle$. This means $j_c(k=0)/\sin(B/2) \neq 0$.

We stress, that this ansatz is in perfect agreement with outcomes of exact diagonalization as can be seen in Fig. I.6. Exact diagonalization evaluates the expectation value of the following operator

$$j_c(k=0)/\sin\left(\frac{B}{2}\right) = \frac{1}{2}\hat{a}_{k=0}^\dagger\tau_z \otimes \mathbb{1}\hat{a}_{k=0} = \frac{1}{2L} \sum_{rr'} \hat{a}_r^\dagger\tau_z \otimes \mathbb{1}\hat{a}_{r'}. \quad (\text{I.85})$$

I.7 SIMULATION FEASIBILITY

In the next chapter we want to insert interactions and analyze their interplay with the non-interacting Hamiltonian. We make explicit use of density-density interactions which immediately turn the overall Hamiltonian into a non-integrable system.

Nevertheless, there are many tools to access observables and approximate the ground state numerically. One of them is the very successful **DMRG** method introduced in 1992 by Stephen White [23]. It is an algorithm that approximates ground state energies by variationally optimizing entries in the reduced density matrix. In the past 20 years a huge progress in entanglement theory has provided upper bounds in entanglement for quantum critical systems which is in the end the reason why **DMRG** works so well in one-dimensional systems [21, 24].

For our purposes, we use a variational **MPS** method that respects the **U(1)** symmetry of particle conservation. The program on which our computation is based on has been written in advance and makes use of a very convenient form of the Hamiltonian in the context of **MPS** - a local Hamiltonian that is usually called Matrix Product Operator (**MPO**). We consider implementation aspects of an **MPS** program respecting a global **U(1)** symmetry out of scope for this thesis and refer the interested reader to [11, 14, 25].

In this section we estimate if **MPS** are suited to tackle the non-interacting problem and elaborate restrictions to guarantee reliability of results for a fixed setup of $L = 32$, $\Omega = 0.2$, $J = 0.1$ and $B = \pi/2$.

The variational **MPS** method is based on truncation of elements of the reduced density matrix. This truncation corresponds to a cutoff probability that provides a reasonable quantity of convergence which we call truncated probability. In tensor networks, this truncation is a consequence of restricting the dimension of local tensors - which we call bond dimension. We show in Fig. 18 the truncated probability at the central sites at given bond dimensions up to $M = 500$. It becomes clear that we are not able to push the simulation with reasonable computation time to a better accuracy than $\mathcal{O}(10^{-6})$.

We compare numerical outcomes with the exact solutions and they coincide very well, considering that the truncation error is still quite large. This is explicitly remarkable for non-local measurements that rely on the full space of two-point correlations such as the chiral currents and the momentum zero current as shown in Fig. 19.

For local measurements such as core energy or occupation probability, we find strikingly accuracies with errors below $\mathcal{O}(10^{-5})$. Even Friedel oscillations of the occupation pattern caused by scattering on the boundaries [26] remain correct with an error smaller than 1% (see Fig. 21).

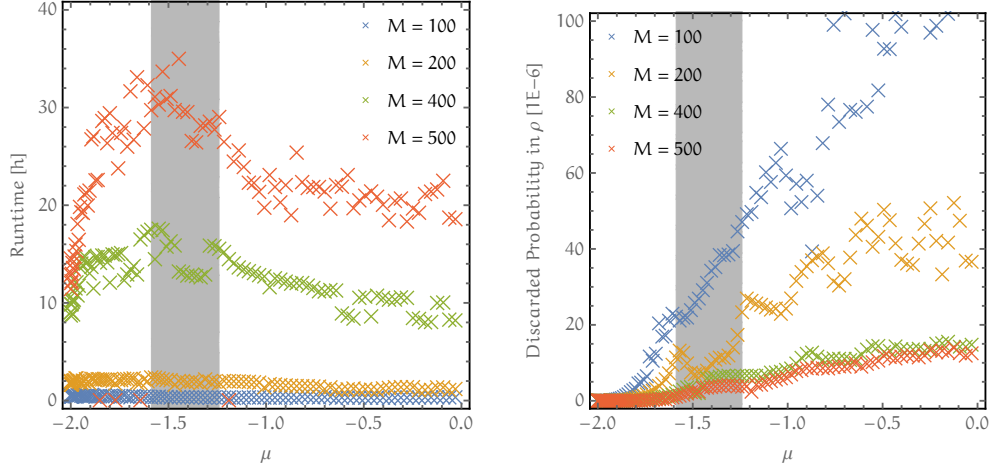


Figure 18: Left figure: Runtime for four sweeps. Right figure: Truncated probability in units of 1×10^{-6} .

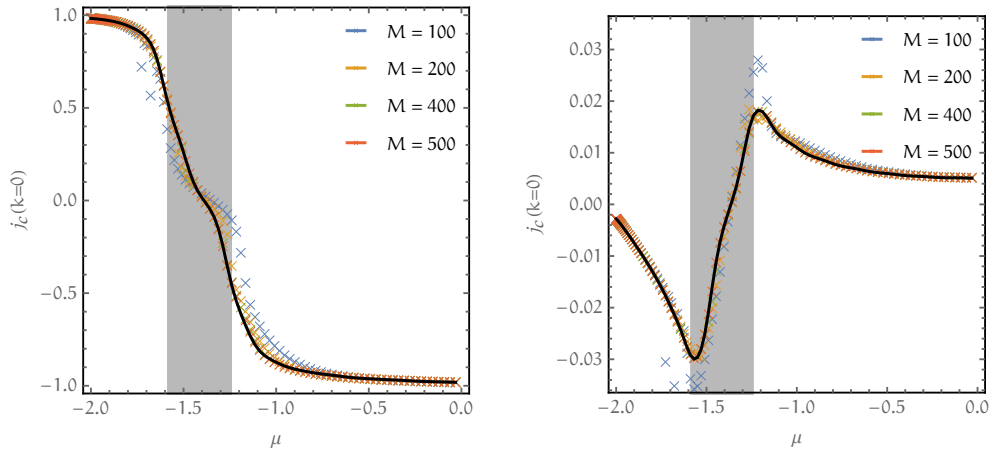


Figure 19: Momentum zero current (left) and chiral current (right) for the non-interacting problem dealing with variational MPS (colored crosses). For $M = 500$, they are perfectly aligned to the exact solutions (black line).

For short systems of sizes $L = 32$, the parameter space remains trivial everywhere (since the two boundary modes do not show up). As a consequence, the ground state energy is unique and we do not see any degeneracies in both energy and entanglement spectrum (see Fig. 23 and Fig. 24).

We did provide the generic expression to compute the VNEE of any quadratic Hamiltonian, which shows for large enough systems a plateau of maximal entanglement in the topological regime of the four-leg ladder system (see Fig. 8). An explanation for the origin of this plateau is the degeneracy of ground states caused by two boundary modes.

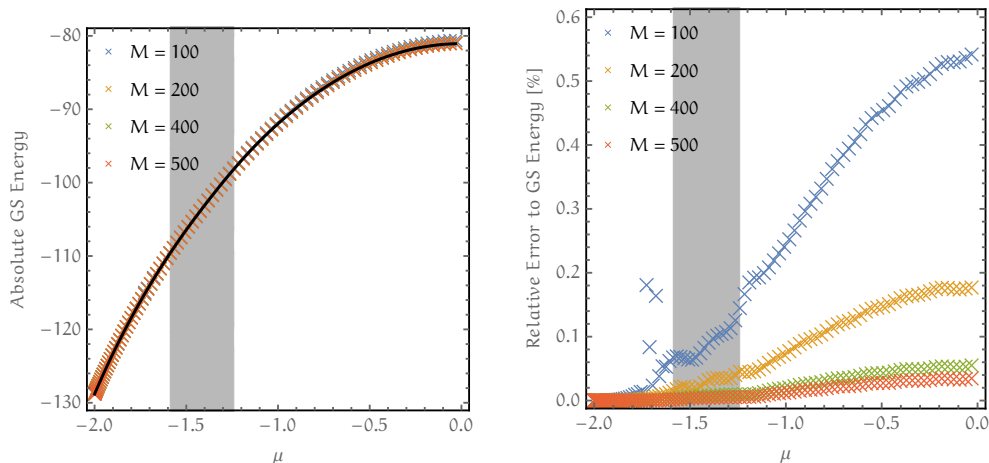


Figure 20: The ground states converge delicately to the exact value when we increase the bond dimension. The error is already below 10^{-2} for small $M = 100$.

When we increase the size of the system to close the splitting of the two boundary zero modes, the MPS does not capture the correct ground states. This degeneracy is hard to resolve in simulations, as we explain in this paragraph. Variational MPS limits the amount of entanglement between subsystem A and its complement A^C by neglecting the Schmidt values below a certain limit, which relates to a truncation of states contributing to A with low probability. This procedure is repetitive for all possible sizes of subsystem A . For open systems we already showed the existence of two boundary modes in the topological region, as explicitly shown in the right plot of Fig. 6. In analog to localized impurity modes in similar models [27], one may understand the two orthogonal ground states $|\Psi\rangle_{\pm} = \frac{1}{\sqrt{2}} (|\phi\rangle_L \pm |\phi\rangle_R)$ as a superposition of two fermionic states $|\phi\rangle_{R/L}$ that distinct completely and solely in the occupation of the right or left boundary mode. These modes occur only with vanishing probability in the vicinity of one of the impurities and are exponentially localized at the other. Since the encoding of such a cat state costs an extra $\ln 2$ in the entanglement entropy with respect to a single localized state, we expect the MPS algorithm to collapse onto one of the latter ones (thus to a minimally entangled state), as soon as the energy splitting between the two modes is small enough. In a sense, this exchange of low entanglement versus energy accuracy will take place whenever possible.

For overall gapped phases, as we observe in all cases of small systems, we do not have an exact degeneracy of the ground state. But even there we observe an excess of entanglement in the topological phase that we miss in the simulation for $M < 400$ (see Fig. 22).

But, the algorithm does capture important bulk-states and as a result, local expectation values remain reliable, since relative errors can be brought to order $\mathcal{O}(10^{-3})$ and below quite easily. On the other hand, we cannot obtain the correct entanglement spectrum in topological regimes by simulating the fixed half filling charge sector. Instead, it is possible to simulate simply the next charge sector

$N = 2L \pm 1$ to capture the physics of both boundary modes (since for $N = 2L + 1$, both boundary modes have to be occupied and for $N = 2L - 1$ none is occupied), which indeed suffices to find missing parts in the entanglement spectrum.

We conclude from the analysis of numerical observations in this section that we need a lower limit for the system size of order $\mathcal{O}(100)$ to be able to numerically access any boundary modes present in the (non-)interacting case. To additionally guarantee reliability of expectation values, we have to restrict the bond dimension to cases $M \geq 200$. In summary, variational MPS respecting $U(1)$ symmetry are exceptionally suited for this specific problem.

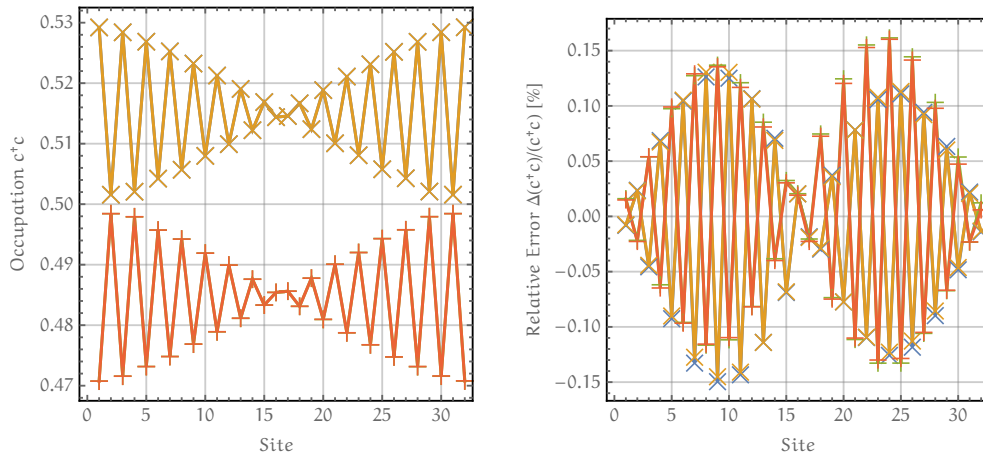


Figure 21: Occupation pattern (left) and relative error to exact solutions (right). Even the oscillations caused by the ladder's finite size are reproduced in the simulation with errors that remain far below 1%. Their behavior can be described with Friedel oscillations, that occur in simple band structures with only one pair of Fermi points as $n \propto \cos(2k_F(x - L/2))$ caused by scattering on the edges on the system. For two pairs of Fermi points, the resulting modulation is a superposition of multiple scatterings with different momenta.

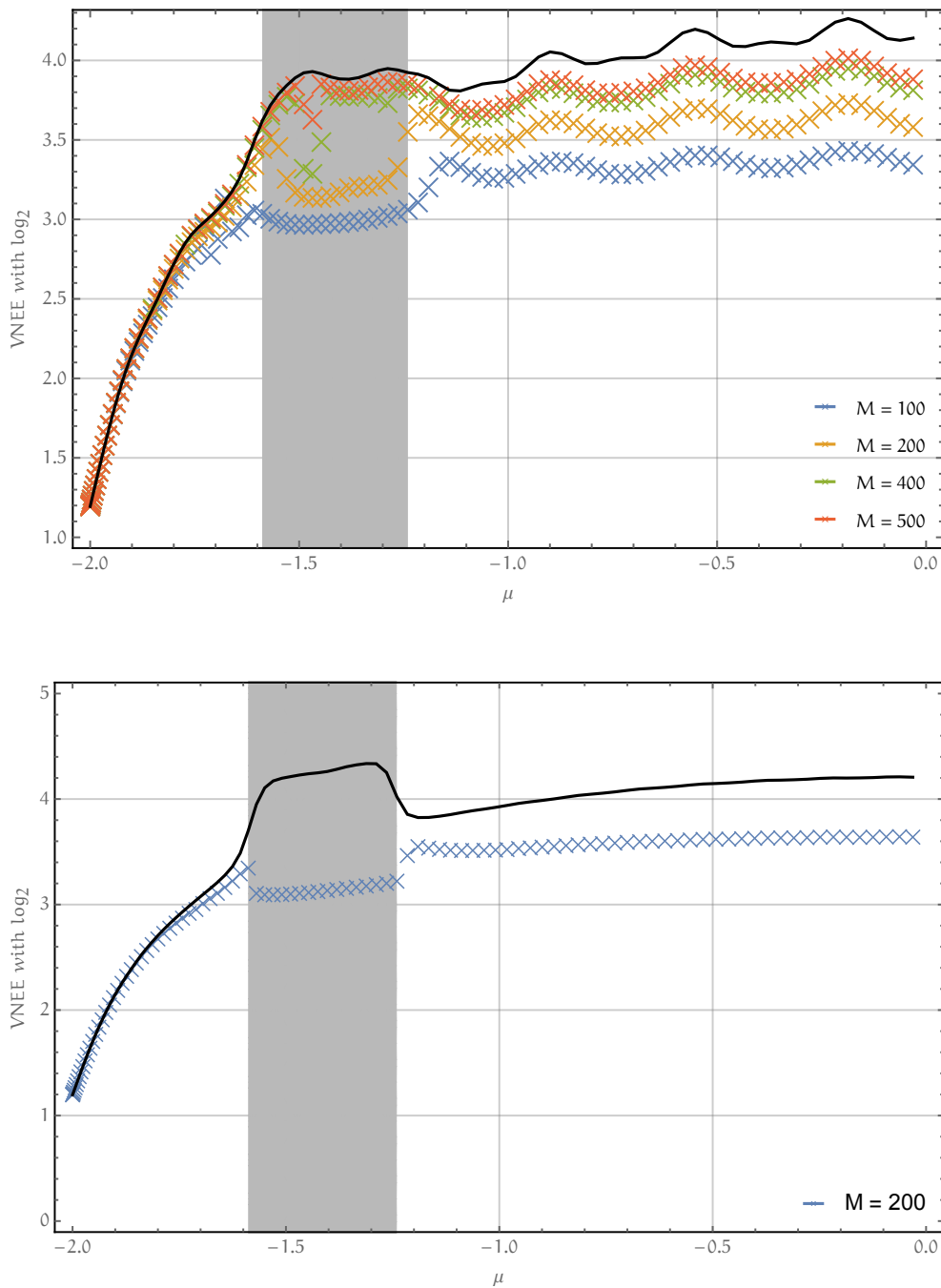


Figure 22: Top: We notice for a system of $L = 32$ sites that in the topological regime, there exists a plateau in the von Neumann entanglement entropy that cannot be resolved numerically until we reach a bond dimension $M = 500$. When the system size is $L = 32$, the ground state unique, but the approximative wave function collapses for $M < 500$ to a lower entangled state anyway. We see that the entanglement entropy for $\mu \rightarrow 0$ is not completely approached by MPS since they show a noticeable offset for all bond dimensions. Bottom (80 sites): Same scenario but for a system of $L = 80$ sites. The system deviates by a factor $\log(2)$ from exact solutions in the topo. region thus the routine collapses to a minimally entangled state at the topo. borders.

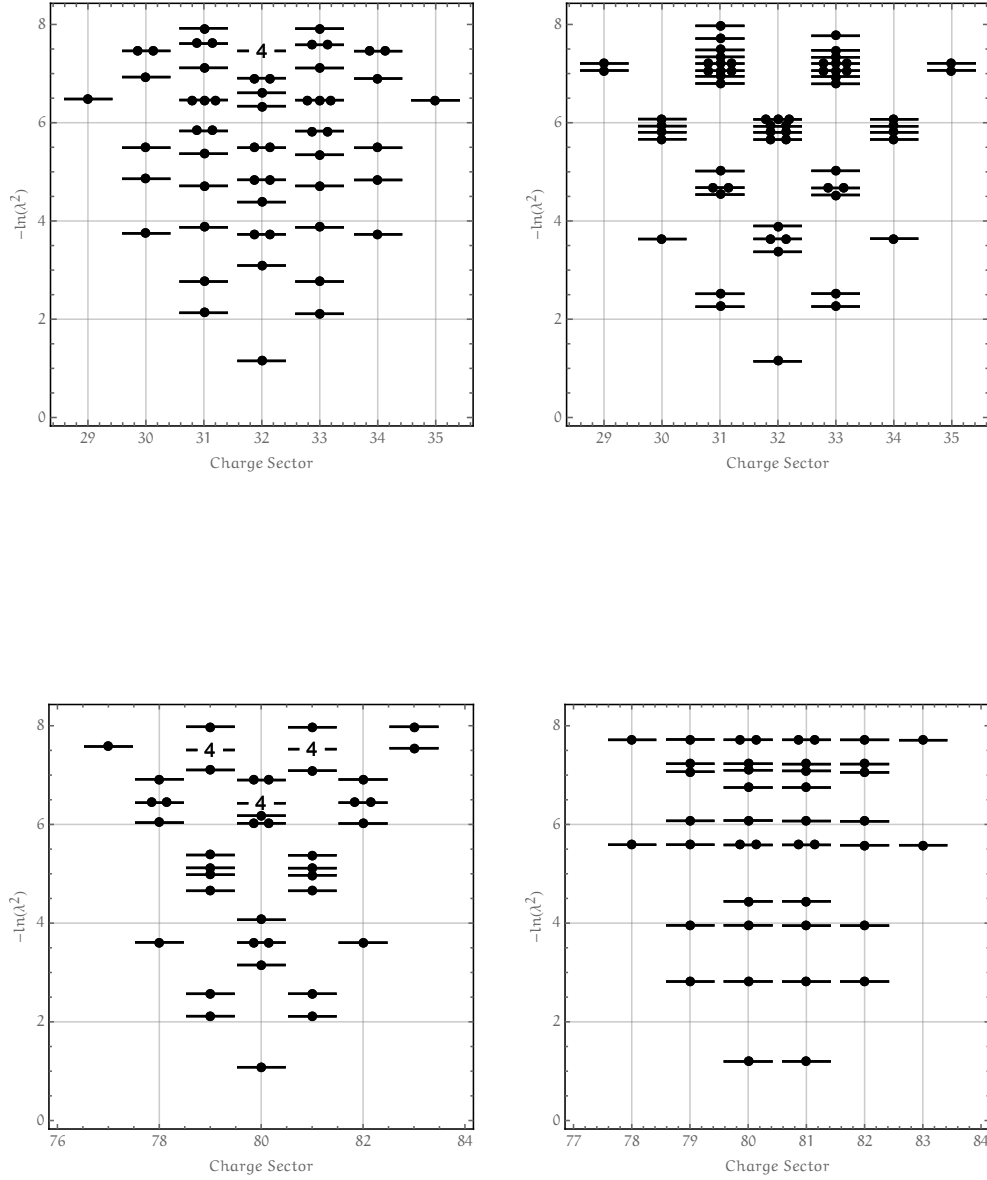


Figure 24: Top row: Slice of Fig. 23 at $\mu = -1.0$ (left) and $\mu = -1.5$ (right) phase for $L = 32$ sites. The lowest spectral lines correspond, since there is still a net energy gap everywhere and no energy zero modes whatsoever. This means that the ground state is unique everywhere, and the phase remains trivial. Bottom: Same parameter space, but $L = 80$ sites. The system is obviously in a nontrivial phase due to the doubly degenerate entanglement spectrum. Nevertheless, as already discussed, the simulation collapses to a minimally entangled state.

II

HUBBARD INTERACTION

After a careful discussion of the single particle physics, we implement Hubbard interactions with different ranges on top of the non-interacting four- and two-leg ladder model. We have the aim to find numerical evidence for fQH regimes based on analytic predictions from a Bosonization approach [12].

We start with a motivation of the Hubbard interaction before we analyze the four-leg model with nearest neighbor interactions and find that the potential μ suffers from their repulsive nature. Considering a simple mean-field approximation provides an explanation for adjustments within the scope of weak-coupling regimes.

We revise predictions in [12] and analyze the constraints on K_ρ which allow for the emergence of fractional QH phases. We conclude that it could be possible to observe emergent $\nu = 1/3$ Laughlin states in a system with nearest neighbor interactions, but a final answer remains to be given in future works.

As a highlight, we present numerical evidence for *emergent $\nu = 1/2$ fQH phases in purely fermionic environments*. Furthermore, we state operators in terms of bosonized fields which might be relevant for the emergence of such states, but a satisfying proof still remains to be completed.

For next-to-nearest interactions, we verify the presence of a $\nu = 1/3$ fQH phase.

II.1 MOTIVATION

The Hubbard model has been introduced to describe correlation phenomena in transition metals that have narrow energy bands [28]. Despite being an oversimplified version of interacting quantum particles, it already includes a vast amount of physical phenomenon such as superconductivity, ferro- and antiferromagnetism.

In the following, we first derive the model and motivate the appearing interaction term, before we discuss approximate solutions for special cases.

A solid consists of electrons and ions being condensed in a three-dimensional structure. Since electrons have much lower mass than ions, their movement is on a faster time-scale. This is the reason for a first assumption: A static lattice for the positions of ions - the Born-Oppenheimer approximation [29]. The most generic Hamiltonian for such a system is given by

$$H^{\text{BO}} = \sum_i^N \frac{\vec{p}_i^2}{2m} + V_I(\vec{x}_i) + \sum_{1 \leq i < j \leq N} V_C(\vec{x}_i, \vec{x}_j), \quad (\text{II.1})$$

with N being the number of electrons, V_I being the potential of the ions and V_C describing the Coulomb repulsion

$$V_C(\vec{x}_i, \vec{x}_j) = \frac{e^2}{|\vec{x}_i - \vec{x}_j|}. \quad (\text{II.2})$$

The resulting differential equations for the dynamics of the electrons are not analytically solvable due to the complexity of V_I . This justifies the use of further approximations. Most of these assumptions rely on effective mean-fields by means of auxiliary potentials V_A that transform the potential to

$$H^{\text{BO}} = \sum_i^N \frac{\vec{p}_i^2}{2m} + V(\vec{x}_i) + \sum_{1 \leq i < j \leq N} U(\vec{x}_i, \vec{x}_j). \quad (\text{II.3})$$

In this picture V is a one- and U a two-body potential of the form

$$V(\vec{x}) := V_A(\vec{x}) + V_I(\vec{x}), \quad (\text{II.4})$$

$$U(\vec{x}, \vec{y}) := V_C(\vec{x}, \vec{y}) - \frac{1}{N-1} (V_A(\vec{x}) + V_A(\vec{y})), \quad (\text{II.5})$$

and the two-body potential U is considerably reduced in range and magnitude with respect to the bare Coulomb interaction. A physical justification for those auxiliary fields is the answer to the following question: What potential does an additional charge feel in the structure? An additional electron does not only feel the potential of the ions, but also an effective potential proportional to the density of all other electrons. This potential comes with opposite sign, but has the same symmetry as the ion potential. One may argue that this is only partially true since local, additional charges change the ground state density. But in the thermodynamic limit the effect of a single charge is negligible. The introduction

of those fields determines the matrix elements of \mathbb{U} expressed in eigenfunctions of the single-particle part

$$h_1(\vec{x}, \vec{p}) := \frac{\vec{p}^2}{2m} + V(\vec{x}). \quad (\text{II.6})$$

These eigenfunctions are typically Bloch functions that respect translational invariance of a periodic function V and have the general form

$$\varphi_{\vec{k}\alpha}(\vec{x}) = e^{i\vec{k}\vec{x}} u_{\vec{k}\alpha}(\vec{x}). \quad (\text{II.7})$$

satisfying

$$h_1(\vec{x}, \vec{p}) \varphi_{\vec{p}\alpha}(\vec{x}) = \epsilon_{\vec{p}\alpha} \varphi_{\vec{p}\alpha}(\vec{x}). \quad (\text{II.8})$$

More convenient for discretized systems are Wannier functions, which provide mutually orthogonal eigenfunctions $\Phi_\alpha(\vec{x} - \vec{R}_i)$ for different bands α and different grid positions i ,

$$\Phi_\alpha(\vec{x} - \vec{R}_i) := \frac{1}{\sqrt{L}} \sum_{\vec{k}} \varphi_{\vec{k}\alpha}(\vec{x} - \vec{R}_i). \quad (\text{II.9})$$

Since the Bloch functions provide an orthogonal basis, we can easily solve for the φ 's in the previous expression,

$$\varphi_{\vec{k}\alpha}(\vec{x} - \vec{R}_i) = \frac{1}{\sqrt{L}} \sum_i e^{i\vec{k}\vec{R}_i} \Phi_\alpha(\vec{x} - \vec{R}_i). \quad (\text{II.10})$$

The Hamiltonian introduced in Eq. II.3 can be expressed in terms of Wannier functions, when we introduce fermionic creation operators $\hat{c}_{\vec{k},\alpha\sigma}^\dagger$ that create a Bloch state $\varphi_{\vec{k},\alpha}$ with spin σ . We further need the operator representation for an electron with spin σ at position \vec{x} ,

$$\Psi_\sigma^\dagger(\vec{x}) := \sum_{\vec{k}\alpha} \varphi_{\vec{k}\alpha}^*(\vec{x}) \hat{c}_{\vec{k},\alpha\sigma}^\dagger = \sum_{\alpha i} \Phi_\alpha^*(\vec{x} - \vec{R}_i) \hat{c}_{i,\alpha\sigma}^\dagger, \quad (\text{II.11})$$

with the Fourier transform

$$\hat{c}_{i,\alpha\sigma}^\dagger = \frac{1}{\sqrt{L}} \sum_{\vec{k}} e^{-i\vec{k}\vec{R}_i} \hat{c}_{\vec{k},\alpha\sigma}^\dagger. \quad (\text{II.12})$$

Upon the continuous formulation and the introduction of overlap integrals, [30] yields

$$\begin{aligned} H^H = & \sum_{\sigma \in \{\uparrow, \downarrow\}} \int d\vec{x}^3 \Psi_\sigma^\dagger(\vec{x}) h_1(\vec{x}) \Psi_\sigma(\vec{x}) + \\ & \frac{1}{2} \sum_{\sigma\sigma'} \int d\vec{x}^3 d\vec{y}^3 \Psi_\sigma^\dagger(\vec{x}) \Psi_{\sigma'}^\dagger(\vec{y}) U(\vec{x}, \vec{y}) \Psi_{\sigma'}(\vec{y}) \Psi_\sigma(\vec{x}). \end{aligned} \quad (\text{II.13})$$

This procedure makes it possible to use Eq. II.11, introduce parameters instead of evaluating overlap integrals of Wannier functions and transfer the Hamiltonian to the language of second quantization

$$\hat{H}^H = \sum_{ij\alpha\sigma} t_{ij} \hat{c}_{i,\alpha\sigma}^\dagger \hat{c}_{j,\alpha\sigma} + \frac{1}{2} \sum_{\alpha\beta\gamma\delta} \sum_{ijkl} \sum_{\sigma\sigma'} U_{ijkl}^{\alpha\beta\gamma\delta} \hat{c}_{i,\alpha\sigma}^\dagger \hat{c}_{j,\beta\sigma'}^\dagger \hat{c}_{k,\gamma\sigma'} \hat{c}_{l,\delta\sigma}. \quad (\text{II.14})$$

Now the complexity is contained in the single particle hopping matrix t_{ij} and the interaction tensor $U_{ijkl}^{\alpha\beta\gamma\delta}$. Both explicit forms depend on the auxiliary field V_Λ and the choice of Wannier functions $\Phi_\alpha(\vec{x} - \vec{R}_i)$. Up to this point, the model corresponds exactly to Eq. II.13.

With control over the auxiliary field V_Λ , it is possible to reduce off-diagonal terms in such a manner that the dominating interactions are intra-band processes. This motivates an effective single-band approximation. In this picture transitions between different sites and different kinds of fermions are small compared to density-density repulsions, which yields

$$\hat{H}^H = \sum_{ij\alpha\sigma} t_{ij} \hat{c}_{i,\alpha\sigma}^\dagger \hat{c}_{j,\alpha\sigma} + \sum_{\sigma\sigma'} \sum_{ij} U_{ij} \hat{\rho}_i \hat{\rho}_j. \quad (\text{II.15})$$

In this expression, $\rho_i = \hat{c}_{i,\alpha\sigma}^\dagger \hat{c}_{i,\alpha\sigma}$ and the matrix U_{ij} controls the range and strength of the interaction between the two densities at sites i and j . In general, connecting values of U_{ij} to tunable parameters in experiments is difficult, but not impossible. Following the motivation of this Hamiltonian, the physics explored by means of this model should at least qualitatively capture some behavior of real transition materials. For atoms in optical lattices, the noninteracting physics consists of similar hopping terms dictated by a matrix t_{ij} , which is why we might (at least for the following considerations) substitute t_{ij} here with the noninteracting Hamiltonian of Eq. I.3. We want to assume that the τ chains are well separated such that interactions between the two chains are small compared to interchain processes. This yields the interacting Hamiltonian

$$\hat{H}^I = \hat{H} + \hat{V}^H, \quad (\text{II.16})$$

with \hat{H} being the single particle Hamiltonian analyzed in Ch. I, motivated and introduced in App. C. The Hubbard interaction of generic range ξ for several species at a single physical site depends on $\hat{\rho}_i$, $\hat{\rho}_j$ and ξ . If we want to have the equivalence of Eq. II.15 in each of the τ chains of the four-leg ladder, we consider $\hat{\rho}_\tau := \sum_\sigma \hat{\rho}_{\tau\sigma}$ and require

$$\begin{aligned} \hat{V}^H(\xi) &:= \sum_{ij} \tilde{U}_{ij}(\rho_i, \rho_j, \xi) \\ \tilde{U}_{ii} &:= \frac{U}{2} \sum_\tau \hat{\rho}_{i,\tau} (\hat{\rho}_{i,\tau} - 1) \quad \tilde{U}_{i(i+\xi)} := U \sum_\tau \hat{\rho}_{i,\tau} \hat{\rho}_{i+\xi,\tau} \end{aligned} \quad (\text{II.17})$$

All other matrix elements of \tilde{U} are set to zero, which means that $\hat{V}^H = \hat{V}^H(\xi)$. In analogue to the densities in Eq. II.15, $\rho_{i,\tau}$ reads explicitly

$$\hat{\rho}_{i,\tau} = \sum_{\sigma \in \{\pm 1\}} \hat{c}_{i,\tau\sigma}^\dagger \hat{c}_{i,\tau\sigma}, \quad (\text{II.18})$$

which is the sum of all occupied spin species at lattice position r in subchain τ .

II.2 MEAN FIELD APPROXIMATION

In this section, we compute a shift of the effective potential difference μ caused by the Hubbard interactions in the four-leg ladder. Since this shift enlarges the parameter space which needs to be scanned, it enlarges the overall computational cost. Since we do decouple the τ chains via setting $J = 0$, we restrict further analysis of the Hubbard interactions on a single-chain $\tau = +$ system, neglecting all $\tau = -$ contributions and continue with the search for fractional phases of matter.

The nearest neighbor case restricts the range of interactions to nearest neighbor lattice sites, in other words $\xi = 1$ in Eq. II.17

$$\hat{H}^I = \hat{H} + \hat{V}^H(\xi = 1) = \hat{H} + U \sum_{i,\tau} \left(\frac{\hat{\rho}_{i,\tau}(\hat{\rho}_{i,\tau} - 1)}{2} + \hat{\rho}_{i,\tau} \hat{\rho}_{i+1,\tau} \right). \quad (\text{II.19})$$

We want to open the partial gap with Zeeman splitting Ω , which yields a system with **iQH** phase at density $n_\tau = \frac{B}{\pi}$. The phase transition between trivial and **iQH** phases with respect to the chain filling n_τ has been analyzed using the chiral current in Sec. I.5. For the noninteracting case without chain- and spin-flips $J = 0$ and $\Omega = 0$, we know that the expectation value of the density operator $\hat{\rho}_{i,\tau}$ has a direct relation to the effective potential μ driving the imbalance between the two $\tau = \pm$ chains, namely

$$\langle \hat{\rho}_{i,-} \rangle = \rho_{i,-} = \frac{2}{\pi} \arccos \left(-\frac{\mu}{2} \right). \quad (\text{II.20})$$

This remains approximately valid for small spin-flip contributions ($\Omega \ll t$) (see Fig. 14). When we scan the region of μ to detect current resonances for $U > 0$ we notice that the **iQH** resonance shifts to smaller values of μ which still correspond to the same filling $n = \frac{B}{\pi}$.

To confirm this effect more rigorously, we try an effective mean-field approach. In order to minimize the interaction at small values U , it is tempting to assume half filling $N = 2L$ and approximate the real density with mean values

$$\bar{\rho}_\tau := \frac{1}{L} \left\langle \sum_{i\sigma} \hat{c}_{i,\tau\sigma}^\dagger \hat{c}_{i,\tau\sigma} \right\rangle. \quad (\text{II.21})$$

We then reformulate the expectation value of the Hubbard interaction in terms of $\bar{\rho}_\tau$

$$\begin{aligned} \langle \hat{V}^H \rangle &\approx LU \left(\frac{1}{2} \bar{\rho}_+ (\bar{\rho}_+ - 1) + \frac{1}{2} \bar{\rho}_- (\bar{\rho}_- - 1) + \bar{\rho}_+^2 + \bar{\rho}_-^2 \right) \\ &= LU \left(-\frac{1}{2} (\bar{\rho}_+ + \bar{\rho}_-) + \frac{3}{4} (\bar{\rho}_+ + \bar{\rho}_-)^2 + \frac{3}{4} (\bar{\rho}_+ - \bar{\rho}_-)^2 \right). \quad (\text{II.22}) \\ &= LU \left(2 + \frac{3}{4} (\bar{\rho}_+ - \bar{\rho}_-)^2 \right) \end{aligned}$$

The first two terms do not contribute since we explicitly require a homogeneous particle distribution, i.e. $\bar{\rho}_+ + \bar{\rho}_- = 2$. The remaining task is now to minimize

the overall energy with respect to this mean field and estimate the resulting shift in μ . For this, we need to estimate the kinetic energy at $N^+ = L\bar{\rho}_+$ and $N^- = L\bar{\rho}_-$ particles. The density of states in either $\tau = \pm$ can be written as

$$D^\sigma(E) = \frac{1}{V} \int_{1.BZ} dk \delta(E - \omega^\sigma(k_i)). \quad (\text{II.23})$$

V is introduced for proper normalization and ω is the dispersion relation (special case $J = 0$ of Eq. 1.27),

$$\omega^\sigma(k) = -2 \cos \left(k + \frac{B}{2} \sigma \right). \quad (\text{II.24})$$

Since the integral considers all momenta inside the first Brillouin zone, a substitution $k \rightarrow k + \frac{B}{2} \sigma$ does not change the integral - i.e. the density of states is the same for different spin-species. Let us introduce a function $g(k) := E - \omega(k)$ which simplifies

$$D(E) = \frac{1}{V} \int_{1.BZ} dk \sum_{k_0 \in \ker(g(k))} \frac{\delta(k - k_0)}{|g'(k_0)|} = \frac{1}{V} \frac{1}{\sqrt{1 - \frac{E^2}{4}}}, \quad (\text{II.25})$$

since the kernel of $g(k)$ is explicitly

$$\ker(g(k)) = \pm \arccos \left(\frac{E}{2} \right). \quad (\text{II.26})$$

The volume of the Brillouin zone is $V = \frac{2\pi}{L}$, which normalizes the density of states to

$$M = \int_{-\infty}^{E(M)} dE' D(E') = L \left(\frac{\arcsin(E(M)/2)}{\pi} + \frac{1}{2} \right), \quad (\text{II.27})$$

such that the M^{th} particle has an energy

$$E(M) = 2 \sin \left(M \frac{\pi}{L} - \frac{\pi}{2} \right). \quad (\text{II.28})$$

Hence the total kinetic energy of M particles in such a band is

$$T(M) = \int_{-\infty}^{E(M)} dE' E' D(E') = -\frac{2L \sin(\frac{M\pi}{L})}{\pi}. \quad (\text{II.29})$$

The overall expectation value of the Hamiltonian is then approximated by taking the average of $\bar{\rho}_-$ and considering the results for the kinetic part,

$$\begin{aligned} E &= 2T(N_+) + 2T(N_-) + 2LU + \frac{3U}{4L} (N_+ - N_-)^2 + \mu(N_+ - N_-) \\ &= L(1 - \bar{\rho}_-) (3U(1 - \bar{\rho}_-) - 2\mu) - \frac{8L}{\pi} \sin \left(\frac{\pi \bar{\rho}_-}{2} \right) + 2LU. \end{aligned} \quad (\text{II.30})$$

We arrive at the shift of μ when we minimize the expression above

$$0 = \frac{\partial E(\bar{\rho}_-)}{\partial \bar{\rho}_-} = -\mu - 2 \cos \left(\frac{\pi \bar{\rho}_-}{2} \right) - 3U(1 - \bar{\rho}_-). \quad (\text{II.31})$$

The result is that the interval of μ we need to scan in order to obtain a full picture in densities $\bar{\rho}_-$ grows linearly with the interaction strength. In the i QH phase, we know that the resonance for the chiral current exists at $\bar{\rho}_- = \frac{B}{\pi}$ which becomes in the limit of weak coupling becomes

$$\mu_{\text{res}} = -2 \cos \frac{B}{2} - 3U \left(1 - \frac{B}{\pi}\right). \quad (\text{II.32})$$

To verify the shift, we plot the position of the integer resonance, $\bar{\rho}_- = \frac{B}{\pi}$ (translated in the picture of the imbalance parameter μ) against different values of U .

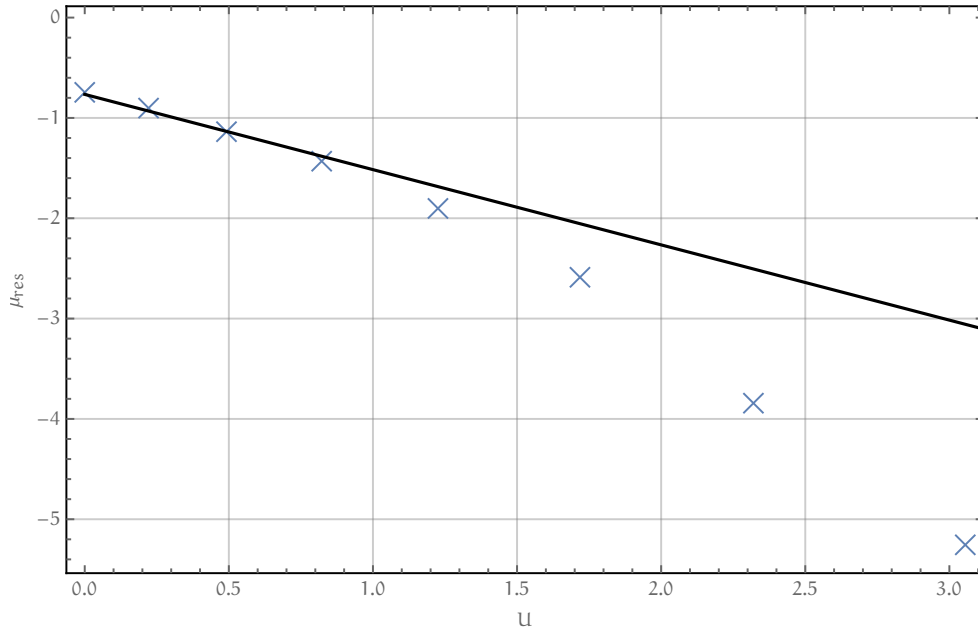


Figure 25: Blue crosses represent simulation outcomes for the position of the i QH phase detected with the chiral current resonance at μ_{res} at $B = \frac{3\pi}{4}$, $\Omega = 0.05$ and $L = 72$. The black solid line is a plot of the mean field analysis that matches very well the simulation results up to $U < t = 1$.

This analysis is only valid for very weak interaction strengths U . For strong couplings, the relation between μ and $\bar{\rho}_-$ remains unclear. From outcomes visualized in Fig. 25, the region of μ we need to scan grows more rapid than linear for $U > 1$. This entails a substantially higher computational cost. A more intuitive visualization of this consequence shows the particle occupation per chain n_τ versus effective potential μ in Fig. 26.

In the following, we assure the effect of chain mixing $J \ll \Omega \ll t$ to be negligible. Then the τ_- -chain is simply a copy of the τ_+ -chain with different particle filling. Therefore we can restrict the analysis to $\tau = +$ species for the confirmation of f QH phases. We expect that, if we find further phases by simulating just one chain, we can easily transfer the interaction strength of interest to the four-leg ladder system and find adapted μ intervals with much less computational effort than exploring the whole parameter space of U and μ in the generalized model. Considering only one chain, we lose the filling control with μ and need to vary

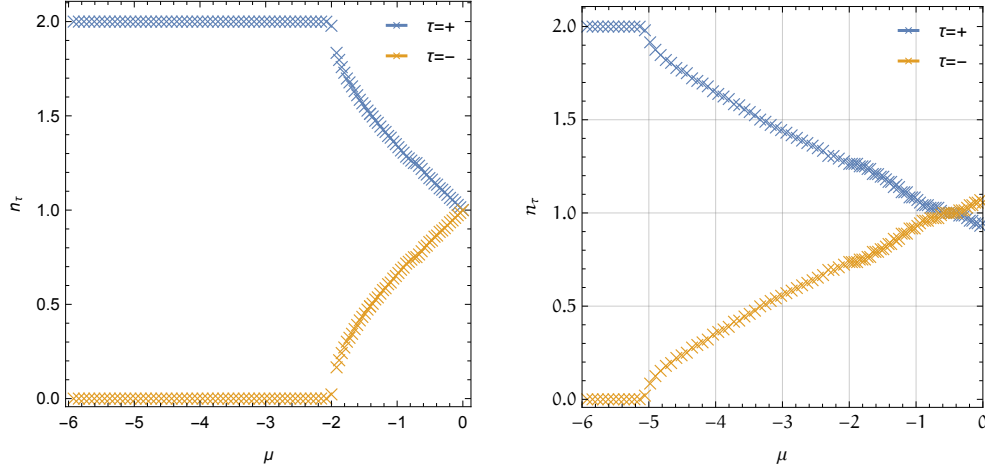


Figure 26: The impact of nearest neighbor Hubbard interactions on the effective potential μ . A nonzero interaction (rhs: $U = 1.2$) increases the interval of μ we need to scan in order to vary the occupation in n_- . For the left case, we might as well stop the simulations at $\mu = -2$, whereas for the right case we must scan up to $\mu \approx -5$ to capture all the different chain densities and therefore, the features of the chiral current.

the density manually by explicitly setting the charge sector, which in turn does not suffer from any of the effects analysed before.

II.3 RESTRICTIONS FROM BOSONIZATION

Via the effective mean field approximation we found that the four-leg ladder suffers from a shift in μ that we do not control for intermediate to strong coupling regimes of the interaction. This is why we decided to perform simulations of the Hamiltonian

$$\begin{aligned} \hat{H}_{\tau=+}^I = & \Omega \sum_{\mathbf{r}} \hat{a}_{\mathbf{r},+}^\dagger \sigma_x e^{iB\mathbf{r}} \hat{a}_{\mathbf{r},+} + t \sum_{\mathbf{r}} \left(\hat{a}_{\mathbf{r}+1,+}^\dagger \hat{a}_{\mathbf{r},+} + \text{H.c.} \right) \\ & + \sum_{\mathbf{r}} \frac{U}{2} \hat{\rho}_{\mathbf{r},+} (\hat{\rho}_{\mathbf{r},+} - 1) + U \sum_{\mathbf{j}=1}^{\xi} \hat{\rho}_{\mathbf{r},+} \hat{\rho}_{\mathbf{r}+\mathbf{j},+} \end{aligned} \quad (\text{II.33})$$

$\hat{a}_{i,+}^\dagger = \left(\hat{c}_{i,++}^\dagger, \hat{c}_{i,++}^\dagger \right)$ is the two-component vector of spin-creation operators in the context of a combination of on-site and nearest neighbor interactions as in Eq. II.17. Since we restrict our investigation to a single chain, the $\tau = +$ label becomes redundant for the rest of this chapter and we will leave it out. This system is a lattice realization of fQH states in a one-dimensional ladder [12]. The requirements to resolve fractional modes in the numerics are constraints on Luttinger liquid parameters, the density n and the maximum range of repulsive interactions ξ . In this section, we briefly recapitulate the process to arrive at the bosonic picture (for further details, [12]).

Suppose there are two types of fields that capture the low-energy fluctuations of the system, namely

$$\sum_{\sigma} \hat{c}_{j,\sigma}^{\dagger} \hat{c}_{j,\sigma} \propto n - \sqrt{2}\pi \nabla \vartheta_{\rho}(x_j) \quad \hat{c}_{j,+}^{\dagger} \hat{c}_{j,+} - \hat{c}_{j,-}^{\dagger} \hat{c}_{j,-} \propto \nabla \vartheta_{\Sigma}(x_j). \quad (\text{II.34})$$

In Eq. II.34, ϑ_{ρ} captures low energy charge-density variations and ϑ_{Σ} describes spin fluctuations with respect to σ_z . Together with some artificial fields Π_{ν} , the spin and charge fluctuations satisfy

$$[\vartheta_{\mu}(x), \Pi_{\nu}(x')] = i\delta_{\mu\nu} \delta(x' - x). \quad (\text{II.35})$$

It is possible to rewrite the noninteracting Hamiltonian in terms of spin $\nabla \vartheta_{\Sigma}$ and charge $\nabla \vartheta_{\rho}$ fluctuations

$$H_B = \sum_{\mu=\rho,\Sigma} \frac{1}{2\pi} \int dx \left(v_{\mu} K_{\mu} (\pi \Pi_{\mu})^2 + \frac{v_{\mu}}{K_{\mu}} (\nabla \vartheta_{\mu})^2 \right). \quad (\text{II.36})$$

We can physically understand this procedure as a change of basis from position and momentum operators $[\hat{x}, \hat{p}] = i$ to charge/spin-density ϑ_{μ} and charge/spin-momentum Π_{μ} . As a side note, $K_{\rho} = 1$ non-interacting case and $SU(2)$ symmetric Hamiltonians respect $K_{\Sigma} = 1$ (the spin degree of freedom remains free). For attractive interactions, K_{ρ} increases - for repulsive ones, K_{ρ} decreases.

We may perform a change of basis to a different set of fields $\vartheta_{\mu} \rightarrow \theta_{\sigma}$ and $\Pi_{\mu} \rightarrow \nabla \phi_{\sigma}$, where σ corresponds to the spin degrees of freedom. In the same way as charge-density and spin-density are connected to the fermionic creation and annihilation operators, the map from charge/spin fields to spin-species fields reads

$$\begin{pmatrix} \theta_{+} \\ \theta_{-} \end{pmatrix} = \frac{1}{\sqrt{2}} \begin{pmatrix} 1 & 1 \\ 1 & -1 \end{pmatrix} \begin{pmatrix} \vartheta_{\rho} \\ \vartheta_{\Sigma} \end{pmatrix}, \quad \begin{pmatrix} \nabla \phi_{+} \\ \nabla \phi_{-} \end{pmatrix} = \frac{\pi}{\sqrt{2}} \begin{pmatrix} 1 & 1 \\ 1 & -1 \end{pmatrix} \begin{pmatrix} \Pi_{\rho} \\ \Pi_{\Sigma} \end{pmatrix}. \quad (\text{II.37})$$

In the integrated picture, these operators satisfy

$$[\phi_{\mu}(x), \theta_{\nu}(x')] = i\pi \delta_{\mu\nu} \Theta(x' - x), \quad (\text{II.38})$$

with the Heaviside function $\Theta(x' - x)$. For a more detailed background about Luttinger liquid theory, we refer to App. A.2. It is possible to express creation and annihilation operators in terms of bosonic fields

$$\hat{c}_{j,\sigma}^{\dagger} \rightarrow \Psi_{\sigma}^{\dagger}(x) \sim \sum_{\mathbf{p}} \Psi_{\sigma,\mathbf{p}}(x), \quad (\text{II.39})$$

$$\Psi_{\sigma,\mathbf{p}}^{\dagger}(x) = e^{i\mathbf{p}(k_F x - \theta_{\sigma}(x)) - i\phi_{\sigma}(x)}. \quad (\text{II.40})$$

We can use Eq. II.40 to rewrite all spin-flip contributions

$$\hat{c}_{j,+}^{\dagger} \hat{c}_{j,-} e^{iBj} + \text{H.c.} \sim \sum_{\text{odd } \mathbf{p}', \mathbf{p}} \Psi_{+, \mathbf{p}'}^{\dagger}(x) \Psi_{-, \mathbf{p}}(x) e^{iBx} + \text{H.c.} \quad (\text{II.41})$$

Evaluating $\Psi_{+,p'}^\dagger(x)\Psi_{-,p}(x)e^{iBx} + \text{H.c.}$ yields operators of the kind

$$\mathcal{O}_{p,p'} \sim 2 \cos((p' - p)k_F x + Bx - p'\theta_+ + p\theta_- - \phi_+ + \phi_-). \quad (\text{II.42})$$

We want to stick to cases in which $\mathcal{O}_{p,p'}$ commutes (with itself) at different position, which demands $p' = -p$.

$$\mathcal{O}_p \sim 2 \cos(-p2k_F x + Bx + p(\theta_+ + \theta_-) - \phi_+ + \phi_-). \quad (\text{II.43})$$

These operators are slowly oscillating for cases $B = 2pk_F$ which is met if the density satisfies

$$2k_F = n\pi = \frac{B}{p} =: \nu B \quad (\text{II.44})$$

with a fractional filling factor $\nu = 1/p$. \mathcal{O}_p generates states that correspond to fQH Laughlin-states (see [31]). This implies that ν is the fractional QH filling factor - the reciprocal of an even integer for bosons and the reciprocal of an odd integer for fermions. In fact, \mathcal{O}_p gives rise to additional resonances in the signature of j_c for the interacting case. It is possible [12] to generalize Eq. 1.71 to

$$j_c \propto \left(n - \nu \frac{B}{\pi} \right). \quad (\text{II.45})$$

The appearance of the current kink depends on the relevance of $\mathcal{O}_{p,-p}$ with respect to competing operators. This relevance can be determined by the scaling dimension x_p of $\mathcal{O}_{p,-p}$,

$$x_p = \frac{1}{2} \left(\frac{1}{K_\sigma} + \frac{K_\rho}{\nu^2} \right) < 2. \quad (\text{II.46})$$

Since $K_\sigma \approx 1$ for $\Omega \ll t$,

$$K_\rho < 3\nu^2. \quad (\text{II.47})$$

The strong coupling limit $U \rightarrow \infty$ provides a lower limit for K_ρ [32],

$$K_\rho > \frac{1}{2} (1 - n\xi)^2. \quad (\text{II.48})$$

It is obvious that we need at least nearest neighbor interactions $\xi \geq 1$ to simulate a nontrivial phase for fermions.

In order to observe a stabilized fQH phase in numerical simulations or experimental setups, the strength of interactions has to be tuned such that K_ρ is inside a certain interval. Let \mathcal{L} be that interval, satisfying both Eq. II.47 and Eq. II.48,

$$\mathcal{L}(\nu, n, \xi) := \left[\frac{1}{2} (1 - n\xi)^2, 3\nu^2 \right]. \quad (\text{II.49})$$

For $U \rightarrow \infty$, the energy per site is only defined for all fillings

$$n < \frac{1}{1 + \xi}. \quad (\text{II.50})$$

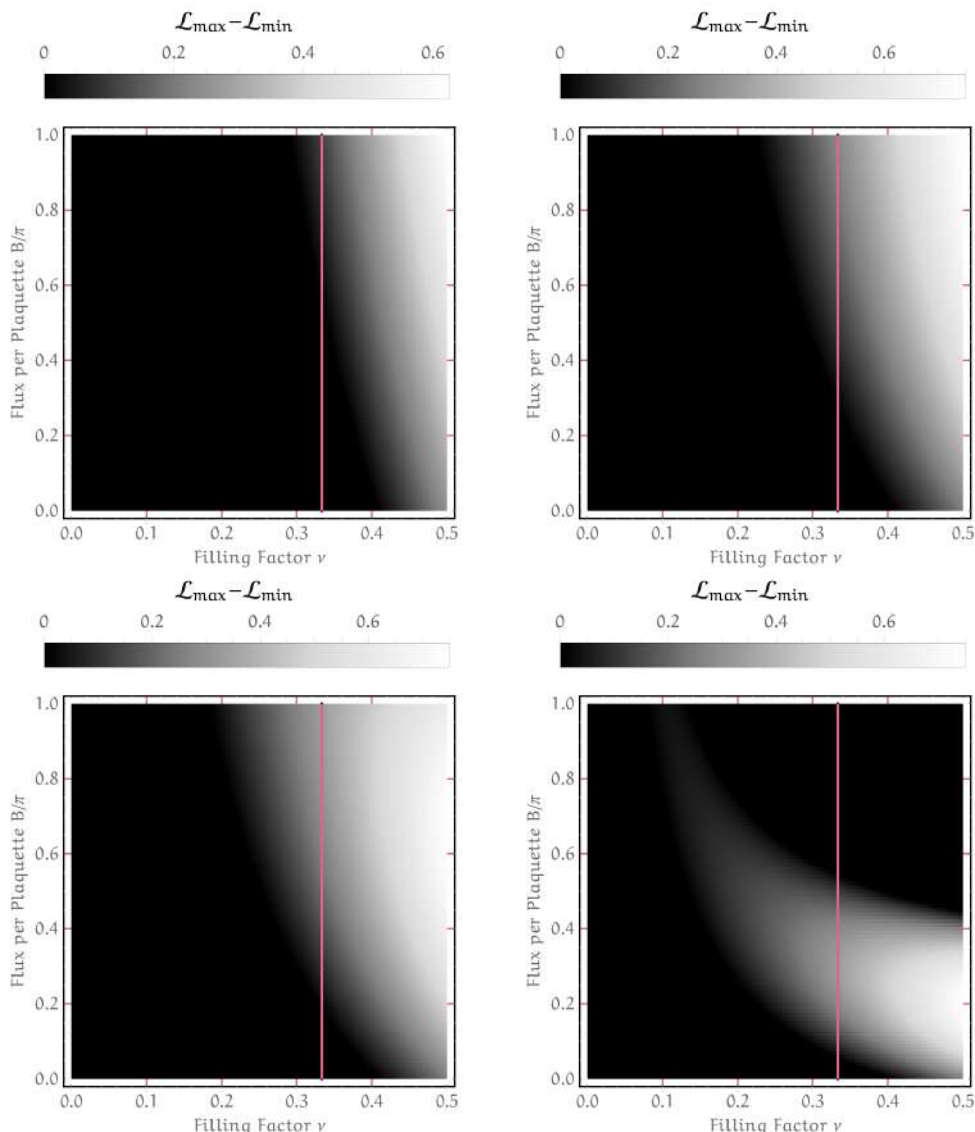


Figure 27: From top left to bottom right, we change the range of the interaction $\xi = 1, 2, 3, 10$ and study the influence on the size of the interval $\mathcal{L}(\nu, n = \nu \frac{B}{\pi}, \xi)$. The red line marks the $\nu = 1/3$ filling factor that we are particularly interested in. For nearest neighbor interactions (top left), the interval for $K_\rho \in \mathcal{L}$ barely allows a region for fractional fermionic phases. This changes in the case of next-to-nearest neighbor interactions (top right), where we have a much larger region for B that respects restrictions from Bosonization.

As shown in Eq. II.44, one may utilize B to shift n_{res} to values that respect Eq. II.50. For the implementation of nearest neighbor interactions, even for the maximum flux per plaquette $B = \pi$, the interval for K_ρ is very small. In other words, U/t has to be large to reduce K_ρ to a value that resides inside \mathcal{L} . Moreover, we want to simulate a system with $B < \pi$ since we are interested in keeping both **iQH** and **fQH** phases visible in the numerics. On the other hand, if we consider large values U/t , the interaction results in a large band gap for fill-

ings $\nu > \frac{1}{1+\xi}$. This destroys all chiral modes and consequently any QH currents.

The recapitulation of proposals in [12] allows for three important technical conclusions:

1. $\xi = 1$ interactions might be suitable for fractional phases, but it will become hard to resolve any relevant signatures. This is due to the divergent interaction strength occurring for sufficiently small values of the density Luttinger parameter K_ρ .
2. Next-to-nearest neighbor interactions will yield a larger interval for $K_\rho \in \mathcal{L}$, but the insulating phase for $\nu > \frac{1}{3}$ destroys iQH phases at smaller values U/t with respect to $\xi = 1$ simulations.
3. Any further interactions $\xi \geq 4$ dramatically restrict \mathcal{B} (concluding ν) and are not suited to obtain both iQH and fQH chiral current signatures for scans along the ν plane simultaneously.

II.4 NUMERICAL RESULTS

The following section about numerical results contains an interesting comparison between numerical results and predictions from Bosonization. We do not find the predicted $\nu = 1/3$ Laughlin states for nearest neighbor interactions, but instead exotic $\nu = 1/2$ phases which do not appear in any literature so far (see Fig. 29).

A second exciting conclusion is that we really observe in the case of next-to-nearest neighbor hubbard interactions all three topological $\nu \in \{1/3, 1/2, 1\}$ QH phases altogether in one phase diagram (see Fig. 31). We provide results for both nearest neighbor and next-to-nearest neighbor interactions by means of variational MPS. We present simulations after 20 sweeps and with bond dimension 200. The truncated probability is of order $\mathcal{O}(10^{-6})$.

NEAREST NEIGHBOR INTERACTION

For a system of length $L = 99$, $t = 1$ and $\Omega = 0.01$, we try to identify regions for U that stabilize $\nu = 1/3$ Laughlin fQH phases. We choose a flux per plaquette of $B = \frac{3\pi}{4}$ and expect the integer QH phase at $n_{\text{res}} = \frac{B}{\pi} = \frac{3}{4}$.

We stress that $L = 99$ is not arbitrarily chosen. A careful analysis of j_c for open

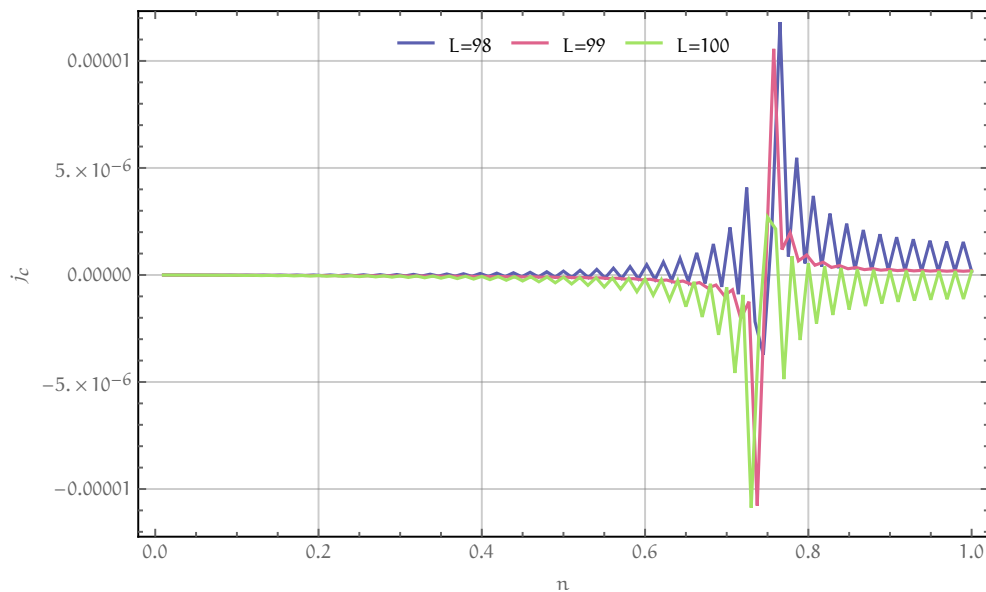


Figure 28: Finite size effects in signatures of j_c at $L = 98, 99, 100$. The parameter space is set to $\Omega = 0.01$, $t = 1$ and $B = \frac{3\pi}{4}$. We want finite size oscillations to be minimal since they might prevent us from recognizing fractional current resonances.

systems yields distinct oscillation patterns that reoccur after period $L \rightarrow L + 8$. In the vicinity of $L = 100$, one finds the systemsize for minimized amplitude of oscillations to be $L = 99$. We want oscillations caused by (obvious) finite size effects to be minimal because they might prevent us from recognizing interesting

emergent current resonances. Fig. 28 displays exact solutions of $j_c(n)$ for the three cases $L = 99$ and $L = 99 \pm 1$.

The chiral current at $\nu = \frac{1}{3}$ is expected to elaborate resonances in the vicinity of $n_{\text{res}}(\nu = 1/3) = \frac{B}{3\pi} = \frac{1}{4}$ at fixed flux $B = \frac{3\pi}{4}$. Numerical data is plotted with black crosses and black joint lines, plus we highlight the numerical data to mark some positions of (possibly) emergent fractional cases. The exact, non-interacting solution for the current is displayed in gray since we observe that the position in the interacting cases slightly deviates.

Fig. 29 shows signatures of j_c for different interaction strengths. The integer resonance is prominent in domains of $U \in [0, 5]$ at the expected density $n_{\text{res}}(\nu = 1) = \frac{B}{\pi} = 3/4$. For $U = 0$, we do not expect to see further resonances, which we verify explicitly in the top panel of Fig. 29. The simulation coincides perfectly with the analytic solution (gray line). Predictions for fermionic systems provide fQH phases that are expected to appear at filling factors $\nu = 1/p$, where p is an odd number (comp. [12]). For $U \in [3, 5]$, we find an unexpected, emergent $\nu = \frac{1}{2}$ phase. This is precisely why the $\nu = 1/2$ phase is particularly interesting in this setup. From the previous recapitulation, especially in Eq. II.43, we conclude this phase to emerge from interactions which satisfy $p' \neq -p$. To be more specific, the resonance condition for relevant operators in this specific setting has to satisfy

$$(p - p')k_F = B \xrightarrow{k_F = \frac{B}{2\nu}} (p - p') \stackrel{!}{=} 4 \quad (\text{II.51})$$

which is valid, if $p = 1$ and $p' = -3$ or $p = 3$ and $p' = -1$. We compute the explicit form of $\mathcal{O}_{p,p'}$ for these specific situations

$$\begin{aligned} \mathcal{O}_{-3,1} &\sim 2 \cos(3\theta_+ + \theta_- - \phi_+ + \phi_-) \\ \mathcal{O}_{-1,3} &\sim 2 \cos(\theta_+ + 3\theta_- - \phi_+ + \phi_-). \end{aligned} \quad (\text{II.52})$$

For deviations of the condition $p \neq -p$, the two different $\mathcal{O}_{p,p'}$ do not commute anymore and both interactions compete. This is why analytic predictions about opening a gap remain unanswered and we must postpone a theoretic conclusion to future works. To understand more about the physics of the observed $\nu = 1/2$ phase, it would be interesting to find their presence in the setting of repulsive on-site interactions. Moreover, on-site interactions do not impose density constraints for $U \rightarrow \infty$ (at least for the interesting region from $0 \leq n \leq 1$).

At values $0 < U/t \leq 5$ we do not see emergent $\nu = 1/3$ Laughlin states. This is why we want to continue our search either by approaching the thermodynamic limit $L \rightarrow \infty$, allowing for a better resolution of any partial gaps, or by approaching the hard-core $U \rightarrow \infty$ limit. Any numerical results for $U/t > 6$ lack sufficient reliability due to phase separation. Currently, we elaborate an effective model for densities $n \leq \frac{1}{2}$ in the limit $t/U \rightarrow 0$ by means of perturbation theory. At half filling $n = \frac{1}{2}$, this approach maps the Hamiltonian to an effective spin-1/2 model with Dzyaloshinskii-Moriya interaction.

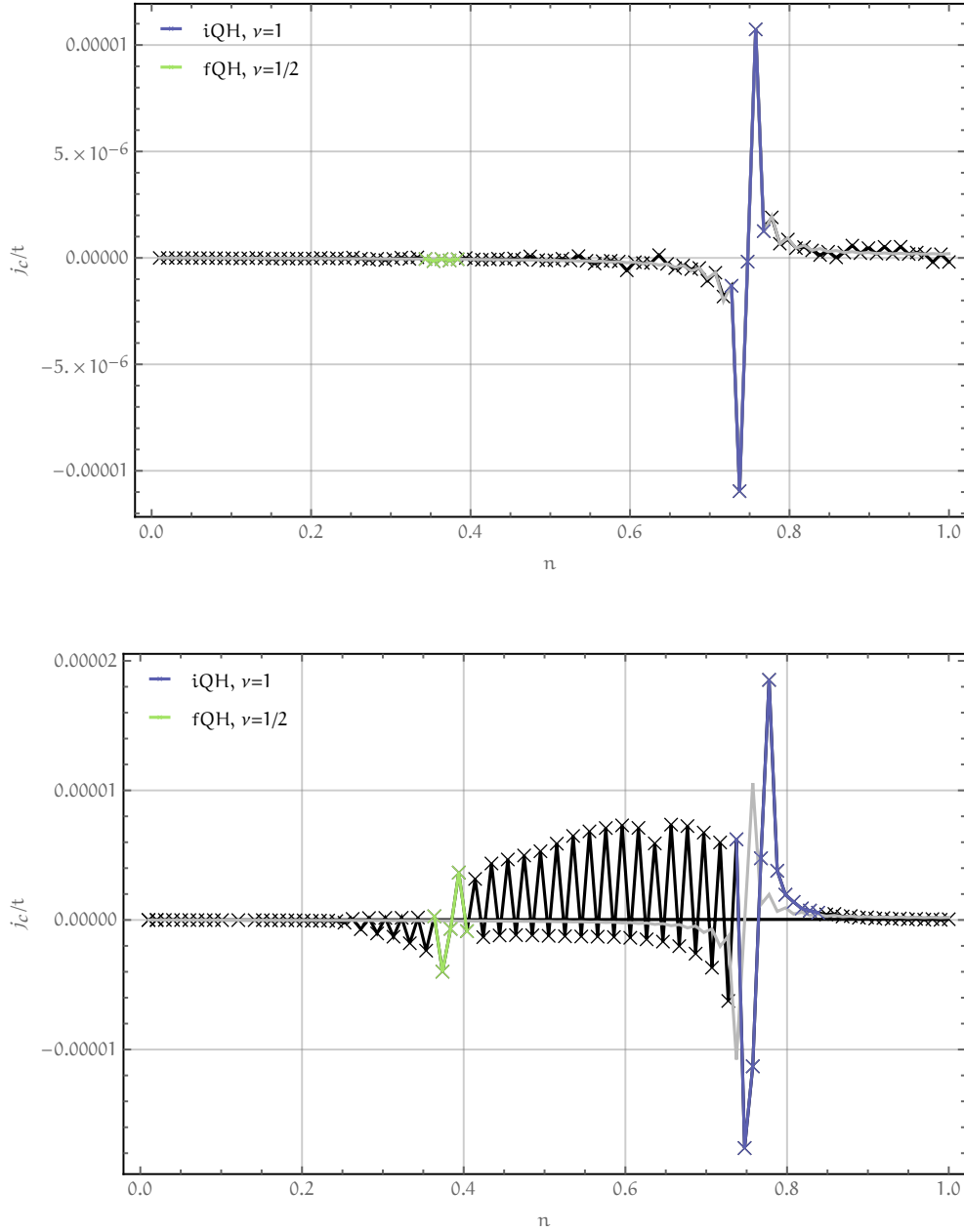


Figure 29: $B = \frac{3\pi}{4}$, $\Omega = 0.01$. Top: $U = 0$. Bottom: $U = 4$. The numerical result of the current (black) for $U = 0$ shows a delicate agreement with exact solutions (gray line). We highlight the position in numerical data of (possible) resonances with adequate labels and discuss their presence (or absence) within this section. For all interactions, the **iQH** phase stays at the expected density $n_{\text{res}} = 3/4$. We observe over a wide range for $U \in [3, 5]$ a stable resonance at $n_{\text{res}} = 3/8$ that corresponds to a **QH** filling factor $\nu = 1/2$ as indicated by the green double-cusp feature. In the language of Luttinger liquid theory, this phase corresponds to states which are (probably) stabilized by exotic operators, dictated by Eq. II.52.

NEXT-TO-NEAREST NEIGHBOR INTERACTION

The absence of $\nu = 1/3$ **fQH** phases for nearest neighbor interactions can be explained with arguments at the end of Sec. II.3 and motivates to include next-to-

nearest neighbor interactions. For coupling $U/t \in [3, 4]$, we observe a prominent $\nu = 1/3$ current, confirming the presence of fractional Laughlin states.

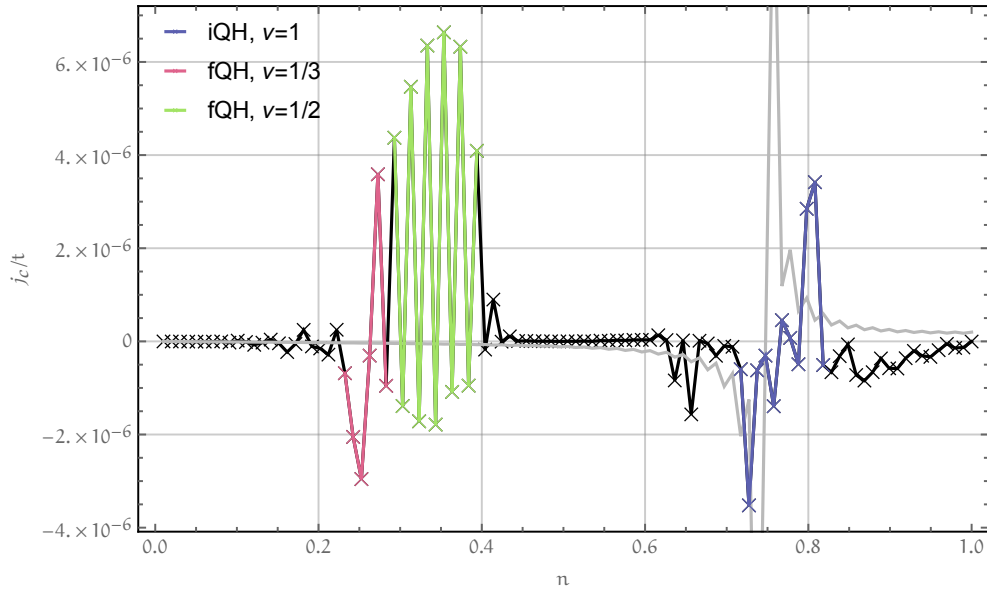


Figure 30: $B = \frac{3\pi}{4}$, $\Omega = 0.01$ and $U = 3$. Grey line: solutions in the noninteracting case. Black lines are numerical simulations, again colorized for regions of interest. The integer $\nu = 1$ cusps of the current start to vanish, whereas the resonance at $\nu \approx 1/3$ becomes more prominent. The extinction of the integer current is expected since densities restrict to $n \leq 1/3$ in the hard-core limit of $U \rightarrow \infty$. This is why we expect a deformation of the integer QH resonance for intermediate regions of U . We must verify, if a phase transition at $n = 1/3$ induces oscillations in the current. In the presented setting, this transition coincides with a possible resonance at $\nu = \frac{1}{2}$.

We observe for the cusps of the integer QH (blue highlight) a deformed shape and decreased amplitude in contrast to the noninteracting case (gray lines). In the limit $U \rightarrow \infty$, we expect an insulating, crystalline phase with three particles per site. This is why we face a phase transition along n when U is strong enough to stabilize crystalline structures. We still have to identify, whether this transition shows a signature in the chiral current or not. This prevents from any conclusion for resonances in the vicinity of $n = 1/3$ (green highlight) for next-to-nearest neighbor interactions or $n = 1/2$ for nearest neighbor interactions. While we marked regions for tentative $\nu = 1/2$ phases in Fig. 30 and 31, we must simulate further runs to decide, if oscillations in the vicinity of $n = 1/3$ indicate the phase transition (unrelated to ν), or, if they are indeed the signatures of the already observed exotic phase.

For $U/t = 2$ (see Fig. 31), we observe a double-cusp signature in the vicinity of $\nu = 1/2$ and $\nu = 1/3$, but, the data is very tentative. Different values for the flux per plaquette $B' < B = \frac{3\pi}{4}$ shift the density n_{res} for all current resonances. We can verify, if the tentative cusps really correspond to fQH states, when we simulate different fluxes to validate the prediction of this shift numerically. If the position of fractional phases in the n plane changes according to $j_c(n_{\text{res}}) = 0$,

we confirm their presence.

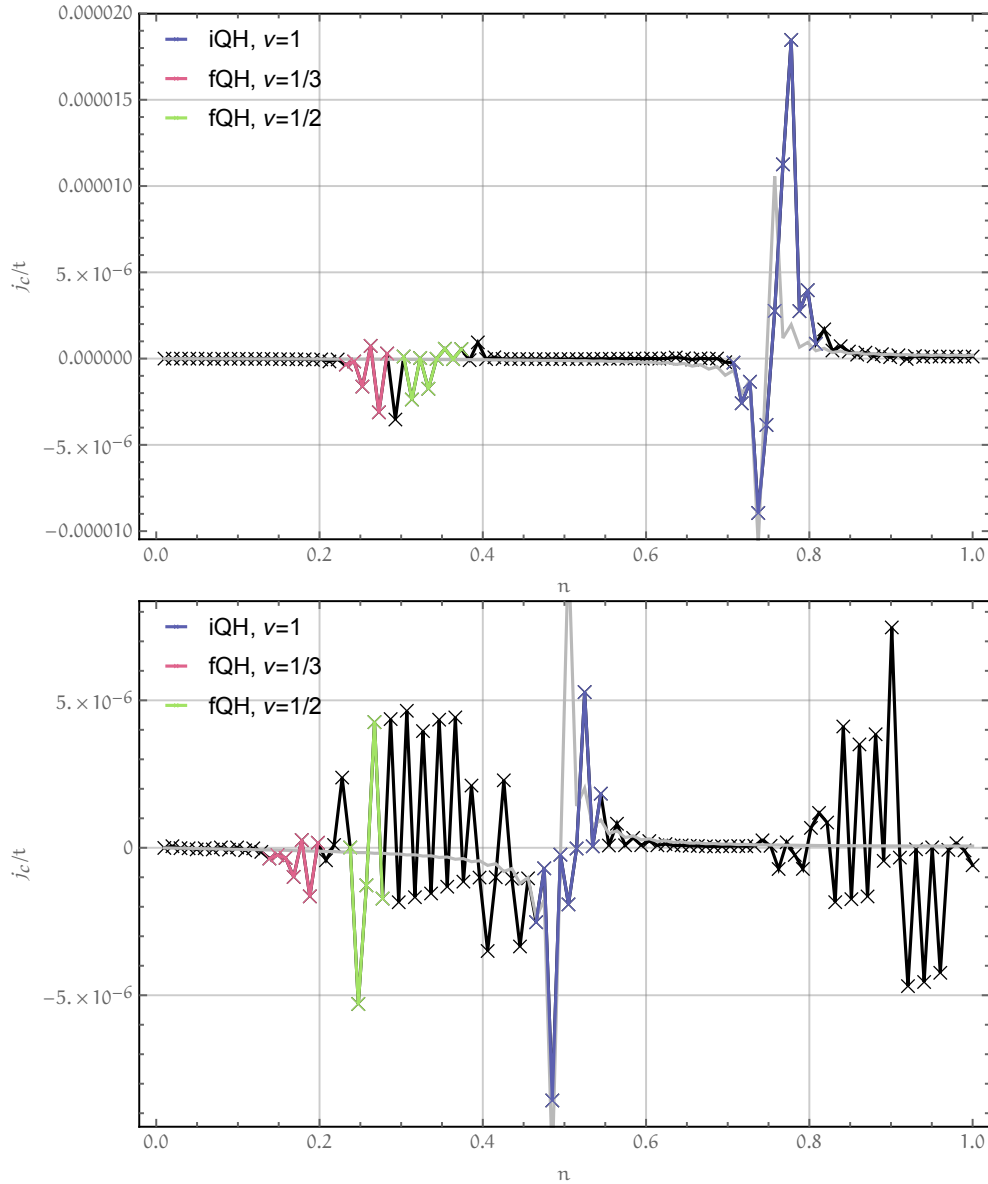


Figure 31: $\Omega = 0.01$. Top: $U/t = 2, B = \frac{3\pi}{4}$. Bottom: $U/t = 2, B = \frac{\pi}{2}$. Grey shapes mark exact noninteracting solutions. We see indeed some nonzero current in a region $\nu \approx 1/3, 1/2$. Both integer and fractional QH resonances are visible. Since current features at densities $n \approx 3/8$ (top) and $n \approx 1/4$ correspond to the shift induced by different fluxes, we conclude that these features belong to the fQH phase.

First results of this approach are visible in the lower panel of 31. The two tentative $\nu = 1/2$ peaks are quite different and we need further runs for a reliable conclusion. In contrary, we do find for $U/t = 2$ and $B \in \{\frac{\pi}{2}, \frac{3\pi}{4}\}$ two similar signatures (highlighted in red), which satisfy the resonance condition for $\nu = 1/3$ Laughlin states.

III

PERSPECTIVES

In this chapter we motivate more exotic interactions and discuss very briefly their relevance for non-Abelian anyons in one-dimensional lattices, including first numerical results in the interplay with the noninteracting two- and four-leg ladder. In this paragraph, I would like to acknowledge M. Burrello's contribution to the ideas presented and in particular to the design of the "experimental setup" for our numerical analysis. Due to the ongoing nature of our work, we mostly refer to results in the literature which constitute the basis for the definition of the exotic interactions, but we leave out several details which will be elaborated in future works.

The interactions are motivated from perspectives of Luttinger liquids. In the four-species ladder, following Eq. II.40, the generalized fermionic operators in the four-leg ladder are expressed in terms of bosonic fields as

$$\hat{c}_{x,\tau\sigma}^\dagger \rightarrow \psi_{\tau\sigma}^\dagger(x) \sim \sum_{\text{odd } p} e^{ip(\tau k_F x + \theta_{\tau\sigma}(x))} e^{-i\phi_{\tau\sigma}(x)}. \quad (\text{III.1})$$

Here, we consider four instead of two different species and consequently need eight dual bosonic fields $\phi_{\tau\sigma}$, $\theta_{\tau\sigma}$, satisfying

$$[\phi_{\tau\sigma}(x), \theta_{\tau'\sigma'}(x')] = i\pi \delta_{\tau\tau'} \delta_{\sigma\sigma'} \Theta(x' - x), \quad (\text{III.2})$$

with Heaviside function Θ . This expressions are only valid for $\Omega \ll t$ and $J \ll t$ to ensure the condition imposed for the Fermi momentum $k_F = \frac{\pi}{2}n$. Up to operators that guarantee correct commutation relations (Klein factors), all subterms in III.1 which satisfy $p > 0$ correspond to so-called right-movers, whereas $p < 0$ terms refer to left-movers at the Fermi level. Let

$$\psi_{\tau\sigma,p}^{L/R\dagger}(x) := e^{\pm ip(\tau k_F x - \theta_{\tau\sigma}(x))} e^{-i\phi_{\tau\sigma}(x)} \quad (\text{III.3})$$

be a shorthand operator for these modes. For convenience, we express the following operators in the language of Luttinger liquids. Consider the spin-flip

transition of σ from $- \rightarrow +$ at constant τ , we find the equivalent expression of $\mathcal{O}_{p,p'}$ in Eq. II.43 which is diagonal in both τ components.

$$\hat{a}_{r,\tau+}^\dagger \hat{a}_{r,\tau-} \cdot e^{iB\tau} \rightarrow \sum_{\substack{\text{odd } p', p \\ \nu, \nu' \in \{L/R\}}} \psi_{\tau+,p'}^{\nu\dagger}(r) \psi_{\tau-,p}^{\nu'}(r) e^{iB\tau}. \quad (\text{III.4})$$

Here, we use explicitly the gauge of Eq. I.64. The same expression is obtained, when we apply the U(1) symmetry (U(1)) transformation of Eq. I.65 to the fermionic field operators and calculate $\hat{a}_j^\dagger \sigma_x \hat{a}_j$. Similarly, the chain-flip transitions are

$$\left(\hat{a}_j^\dagger \tau_x \otimes \mathbb{1} \hat{a}_j \right)_\sigma \rightarrow \sum_{\substack{\text{odd } p', p \\ \nu, \nu' \in \{L/R\}}} \psi_{+\sigma,p'}^{\nu\dagger} \psi_{-\sigma,p}^{\nu'}. \quad (\text{III.5})$$

For the purpose of studying Laughlin states, the relevant interactions impose a condition $p = p'$ [4, 31]. This yields one remaining sum over odd values of p with the following constituents

$$\begin{aligned} \psi_{\tau+,p}^{L\dagger} \psi_{\tau-,p}^L e^{iBx} + \text{H.c.} &\approx 2 \cos(p(+\theta_{\tau+} - \theta_{\tau-}) + Bx - \phi_{\tau+} + \phi_{\tau-}) \\ \psi_{\tau+,p}^{R\dagger} \psi_{\tau-,p}^R e^{iBx} + \text{H.c.} &\approx 2 \cos(p(-\theta_{\tau+} + \theta_{\tau-}) + Bx - \phi_{\tau+} + \phi_{\tau-}) \\ \psi_{\tau+,p}^{L\dagger} \psi_{\tau-,p}^R e^{iBx} + \text{H.c.} &\approx 2 \cos(p(+2\tau k_F x + \theta_{\tau+} + \theta_{\tau-}) \\ &\quad + Bx - \phi_{\tau+} + \phi_{\tau-}) \\ \psi_{\tau+,p}^{R\dagger} \psi_{\tau-,p}^L e^{iBx} + \text{H.c.} &\approx 2 \cos(p(-2\tau k_F x - \theta_{\tau+} - \theta_{\tau-}) \\ &\quad + Bx - \phi_{\tau+} + \phi_{\tau-}) \end{aligned} \quad (\text{III.6})$$

to the earlier, and,

$$\begin{aligned} \psi_{+\sigma,p}^{L\dagger} \psi_{-\sigma,p}^L + \text{H.c.} &\approx 2 \cos(p(+2k_F x + \theta_{+\sigma} - \theta_{-\sigma}) - \phi_{+\sigma} + \phi_{-\sigma}) \\ \psi_{+\sigma,p}^{R\dagger} \psi_{-\sigma,p}^R + \text{H.c.} &\approx 2 \cos(p(-2k_F x - \theta_{+\sigma} + \theta_{-\sigma}) - \phi_{+\sigma} + \phi_{-\sigma}) \\ \psi_{+\sigma,p}^{L\dagger} \psi_{-\sigma,p}^R + \text{H.c.} &\approx 2 \cos(p(+\theta_{+\sigma} + \theta_{-\sigma}) - \phi_{+\sigma} + \phi_{-\sigma}) \\ \psi_{+\sigma,p}^{R\dagger} \psi_{-\sigma,p}^L + \text{H.c.} &\approx 2 \cos(p(-\theta_{+\sigma} - \theta_{-\sigma}) - \phi_{+\sigma} + \phi_{-\sigma}). \end{aligned} \quad (\text{III.7})$$

to the later. The third and fourth transition in Eq. III.6 correspond to the cases we already discussed in Ch. II. All the interesting physics we observe for nearest and next-to-nearest neighbor interactions is due to this transitions between left- and right-movers. References [4, 31, 33, 34] contain detailed discussions about the importance of such transitions to obtain fQH states, and we observed explicitly the emergence of $\nu = 1/3$ Laughlin states for next-to-nearest neighbor interac-

tions. More generally, fractional states can also be obtained by multi-particle interactions which are combinations of left \leftrightarrow right-mover transition operators like

$$\begin{aligned} \mathcal{O}_{\tau=+,p_1,\dots,p_6}^F &= \left(\psi_{++ , p_1}^{L\dagger} \psi_{++ , p_2}^R \right) \cdot \left(\psi_{+- , p_3}^{L\dagger} \psi_{+- , p_4}^R \right) \\ &\quad \cdot \left(\psi_{++ , p_5}^{L\dagger} \psi_{+- , p_6}^R e^{-iBx} \right) , \\ \mathcal{O}_{\tau=-,p_1,\dots,p_6}^F &= \left(\psi_{-+ , p_1}^{L\dagger} \psi_{-+ , p_2}^R \right) \cdot \left(\psi_{-- , p_3}^{L\dagger} \psi_{-- , p_4}^R \right) \\ &\quad \cdot \left(\psi_{-- , p_5}^{L\dagger} \psi_{-+ , p_6}^R e^{+iBx} \right) . \end{aligned} \quad (\text{III.8})$$

If we take $p_1 = p_2 = \dots = p_6$ due to arguments which allow proper commutation at different position, we find the lowest resonance of such interactions at $B = \pm 6k_F$

$$\mathcal{O}_{\tau,1}^F \propto e^{i(\tau(\phi_{\tau-} - \phi_{\tau+}) + 3(\theta_{\tau+} + \theta_{\tau-}))} . \quad (\text{III.9})$$

It is possible to formulate a similar type of interaction when we consider chain-transitions (the ones dictated by J)

$$\begin{aligned} \mathcal{O}_{\sigma,1}^T &= \left(\psi_{+\sigma,1}^{L\dagger} \psi_{+\sigma,1}^R \right) \left(\psi_{-\sigma,1}^{L\dagger} \psi_{-\sigma,1}^R \right) \left(\psi_{+\sigma,1}^{L\dagger} \psi_{-\sigma,1}^R \right) , \\ \mathcal{O}_{\sigma,1}^{T'} &= \left(\psi_{+\sigma,1}^{R\dagger} \psi_{+\sigma,1}^L \right) \left(\psi_{-\sigma,1}^{R\dagger} \psi_{-\sigma,1}^L \right) \left(\psi_{+\sigma,1}^{R\dagger} \psi_{-\sigma,1}^L \right) , \end{aligned} \quad (\text{III.10})$$

which does not require any resonance condition to achieve relevant contributions. Such multi-particle operators are typical candidates to obtain parafermionic operators in interacting nanowires [33, 35].

We must emphasize that the previous operators for $p > 1$ are all irrelevant in the renormalization group meaning for non-interacting systems. Therefore, in the thermodynamic limit, the effect of interaction terms can be seen only through the introduction of suitable interactions which decrease the value of the K_ρ Luttinger parameter in Eq. II.46. In solid state systems, usually, the interactions cannot be tuned and correspond to screened versions of the Coulomb potential. For ultracold atom setups, though, one may envision systems in which it is possible to vary the amplitude and, in certain cases, even the range of the interactions involved. In the following we move even a step forward and we try to design (3-body) interactions whose effect should be as close as possible to the operators that we discussed in Eq. III.8 (and eventually Eq. III.10). For this $p = 1$ component in both operators, we try to devise three-body interactions on the lattice whose field theoretical description includes the previous operators as relevant terms.

$$\begin{aligned} \widehat{V}_{SF}^1 &= U_\Omega \sum_{j,\tau} \hat{\rho}_{j,\tau+} \hat{\rho}_{j,\tau-} \left(\hat{a}_{j+1,\tau}^\dagger (\cos(4k_F)\sigma_x - \tau \sin(4k_F)\sigma_y) \hat{a}_{j+1,\tau} \right) \\ &\quad + \left(\hat{a}_{j,\tau}^\dagger (\cos(4k_F)\sigma_x + \tau \sin(4k_F)\sigma_y) \hat{a}_{j,\tau} \right) \hat{\rho}_{j+1,\tau+} \hat{\rho}_{j+1,\tau-} , \end{aligned} \quad (\text{III.11})$$

$$\widehat{V}_{\text{SF}}^2 = U_{\Omega} \sum_{j,\tau} \hat{\rho}_{j-1,\tau+} \left(\hat{a}_{j,\tau}^{\dagger} \sigma_x \hat{a}_{j,\tau} \right) \hat{\rho}_{j+1,\tau-+} + \hat{\rho}_{j-1,\tau-} \left(\hat{a}_{j,\tau}^{\dagger} \sigma_x \hat{a}_{j,\tau} \right) \hat{\rho}_{j+1,\tau+} \quad (\text{III.12})$$

and

$$\widehat{V}_{\text{CF}} = U_J \sum_{j,\sigma} \hat{\rho}_{j,+ \sigma} \hat{\rho}_{j,- \sigma} \left(\hat{a}_{j-1,\sigma}^{\dagger} \tau_x \hat{a}_{j-1,\sigma} + \hat{a}_{j+1,\sigma}^{\dagger} \tau_x \hat{a}_{j+1,\sigma} \right). \quad (\text{III.13})$$

In terms of the four-leg ladder, we expect the density assisted spin-flip interactions to induce a "Laughlin-like" fractional QH phase with fractional filling factor $\nu = 1/3$ in both the chains τ [36, 4, 34]. This is why we are motivated to search a current resonance, corresponding to these states.

We observe, that such interactions yield phase separation at half filling for both $U_J/\Omega > 1$. Exemplarily, we display different phases caused by the interaction dictated by U_J in Fig. 32. We find in the simulation results four different coexisting, crystalline phases, two pairs of them even living in different charge sectors. This yields dramatically more computational complexity because the overall ground state's degeneracy is very high. We are able to explore this crystalline phases explicitly, when we simulate systems with densities $n \in \{3/8, 3/4\}$.

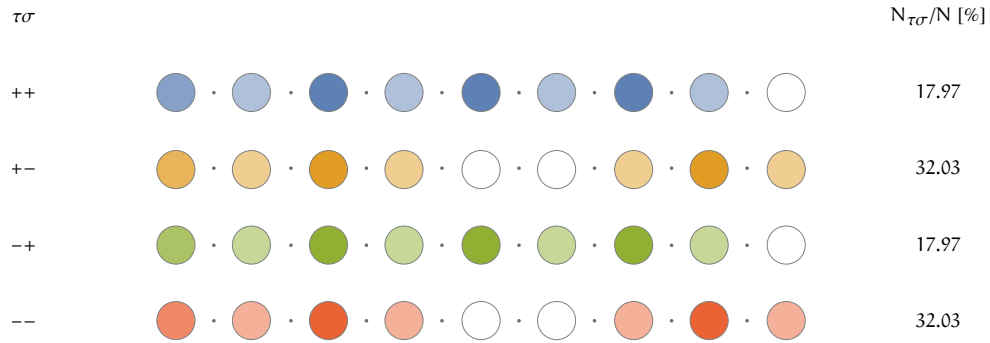


Figure 32: We display the density pattern of all four species σ along the bulk of a system of $L = 32$ sites at $U_J/t = 100$. When the interaction is the dominating process, we observe four different and coexisting crystalline patterns in the bulk of a half-filled chain. Intra-species hopping vanish completely (no arrows in between sites).

DENSITY-DEPENDENT CHAIN-FLIPS

We want to understand the emergence of phase separation for interactions like Eq. III.11, III.12 and Eq. III.13 in the numerical results. We observe that the simulation converges to energetically degenerate states with different recurrent density patterns. This motivates a closer investigation of these crystalline structures in the limit of strong interactions at zero flux B .

We investigate the strong coupling limit of the density-dependent chain-flip interactions $U_J/t \gg 1$ ($J = 0, \Omega/t = 0, \mu = 0$) and restrict the system size to even numbers ($L \in 2\mathbb{N}$). Each two-site configuration contributes to the energy, if and only if the hopping terms $\hat{a}_{j,\sigma}^\dagger \tau_x \hat{a}_{j,\sigma}$ are "enabled" by occupation of right or left nearest-neighbors of the same species as those taking place in the transition, i.e. the densities at $j \pm 1$ satisfy $n_{j+1,+\sigma} n_{j+1,-\sigma} \neq 0$ or $n_{j-1,+\sigma} n_{j-1,-\sigma} \neq 0$. τ_x -processes are minimized by local eigenstates $|\tau_x = -1\rangle_j$ and therefore $n_{j,\tau\sigma} = 1/2$ in the τ_z basis. These transitions contribute with $-2U_J$ when both $n_{j\pm 1,+\sigma} n_{j\pm 1,-\sigma} = 1$.

Indeed, for $N = 3/8L$, we find such staggered configurations along j in the τ chains in the numerical simulations (e.g. Eq. III.14). There are two pairs of degenerate bulk configurations. Since physical states in this setting are given by local densities (up to phases due to the τ_x eigenstates), we may characterize the many-body wavefunction in terms of local bulk occupation patterns. These density patterns will be depicted as disk-patterns, for which the opacity of colors corresponds to $\langle \hat{c}_{j,\tau\sigma}^\dagger \hat{c}_{j,\tau\sigma} \rangle \in \{0, 0.5, 1\}$:

$$|\Psi\rangle \in \left\{ \begin{array}{l} \left| \begin{array}{cccccccc} \circ & \circ \\ \bullet & \bullet \\ \circ & \circ \\ \bullet & \bullet \end{array} \right\rangle, \left| \begin{array}{cccccccc} \circ & \circ \\ \bullet & \bullet \\ \circ & \circ \\ \bullet & \bullet \end{array} \right\rangle \\ , \left| \begin{array}{cccccccc} \bullet & \bullet \\ \circ & \circ \\ \bullet & \bullet \\ \circ & \circ \end{array} \right\rangle, \left| \begin{array}{cccccccc} \bullet & \bullet \\ \circ & \circ \\ \bullet & \bullet \\ \circ & \circ \end{array} \right\rangle \end{array} \right\}. \quad (\text{III.14})$$

The overall lowest ground state has a particle number $N = 3/4L$ (see Eq. III.15). Due to $\Omega = 0$, σ -species do not interact, allowing all possible combinations of two different ground state configurations of the $N = 3/8L$ sector (see Eq. III.14) to form a $N = 3/4L$ ground state (see Eq. III.15). Indeed, we find the following two pairs of degenerate states for numerical simulations in charge sector $n = 3/4$:

$$|\Psi\rangle \in \left\{ \begin{array}{l} \left| \begin{array}{cccccccc} \bullet & \bullet \\ \bullet & \bullet \\ \bullet & \bullet \\ \bullet & \bullet \end{array} \right\rangle, \left| \begin{array}{cccccccc} \bullet & \bullet \\ \bullet & \bullet \\ \bullet & \bullet \\ \bullet & \bullet \end{array} \right\rangle \\ , \left| \begin{array}{cccccccc} \bullet & \bullet \\ \bullet & \bullet \\ \bullet & \bullet \\ \bullet & \bullet \end{array} \right\rangle, \left| \begin{array}{cccccccc} \bullet & \bullet \\ \bullet & \bullet \\ \bullet & \bullet \\ \bullet & \bullet \end{array} \right\rangle \end{array} \right\}. \quad (\text{III.15})$$

For a system of even length, the two contributions of each pair (top/bottom) are "chiral" in the sense that they map into each other under mirroring over the center ($\frac{1}{2} + j \leftrightarrow \frac{1}{2} + 1 - j$ for all j). For a system of odd length, this property is lost and the pairs live in different particle number sectors. Under center-mirroring, each state then maps to itself. This is seen in Eq. III.15, if the extract is assumed to be centered around the center of the chain.

For a total number of particles $N < 3/8L$, the particles agglomerate into a single cluster of local density $n = 3/8$, thus showing an attractive nature.

For $3/8L < N < 3/4L$, we observe patterns with local densities $n = 3/8$ resp. $n = 3/4$ which seem to be energetically favorable with respect to other densities in between. The ground state is then highly degenerate due to the many different possible combinations of such clusters.

DENSITY-DEPENDENT SPIN-FLIPS

We consider the situation in analog to the previous section, but with density-dependent spin-flip interactions $U_\Omega/t \gg 1$ ($J = 0, \Omega/t = 0, \mu = 0$). If we consider the formulation in Eq. III.12 without oscillations in k_F , the main difference to U_J is that we find the degeneracy in τ instead of σ :

$$|\Psi\rangle \in \left\{ \begin{array}{l} \left| \begin{array}{cccccccc} \bullet & \bullet \\ \bullet & \bullet \\ \circ & \circ \\ \circ & \circ \end{array} \right\rangle, \left| \begin{array}{cccccccc} \bullet & \bullet \\ \bullet & \bullet \\ \circ & \circ \\ \circ & \circ \end{array} \right\rangle \\ , \left| \begin{array}{cccccccc} \circ & \circ \\ \circ & \circ \\ \bullet & \bullet \\ \bullet & \bullet \end{array} \right\rangle, \left| \begin{array}{cccccccc} \circ & \circ \\ \circ & \circ \\ \bullet & \bullet \\ \bullet & \bullet \end{array} \right\rangle \end{array} \right\}. \quad (\text{III.16})$$

In charge sector $N = 3/4L$, we find also the three pairs of two degenerate chiral states that assume the same occupation pattern:

$$|\Psi\rangle \in \left\{ \begin{array}{l} \left| \begin{array}{cccccccc} \bullet & \bullet \\ \bullet & \bullet \\ \bullet & \bullet \\ \bullet & \bullet \end{array} \right\rangle, \left| \begin{array}{cccccccc} \bullet & \bullet \\ \bullet & \bullet \\ \bullet & \bullet \\ \bullet & \bullet \end{array} \right\rangle \\ , \left| \begin{array}{cccccccc} \bullet & \bullet \\ \bullet & \bullet \\ \bullet & \bullet \\ \bullet & \bullet \end{array} \right\rangle, \left| \begin{array}{cccccccc} \bullet & \bullet \\ \bullet & \bullet \\ \bullet & \bullet \\ \bullet & \bullet \end{array} \right\rangle \end{array} \right\}. \quad (\text{III.17})$$

For incommensurate N , we again observe a highly degenerate ground state sector with clusterization.

FURTHER PRELIMINARY OBSERVATIONS

We know from the non-interacting system that the spin-transitions give rise to topological behavior whereas chain transitions open a trivial gap. In a similar way, we believe that $\widehat{V}_{\text{SF}}^{1/2}$ give both rise to topologically interesting phases, whereas \widehat{V}_{CF} should not. The definition of the topological phases, however, requires a precise interplay between the single-particle parameters and the interactions, as suggested, for example, by the resonance condition in Eq. II.44 and by the necessity of not gapping out all the chiral modes of the system as required by the Laughlin-like states. The results presented here refer instead to the effect of the interaction terms alone, and must be considered only preparatory future complete analyses.

To really obtain parafermionic modes in the end, we have to add further geometrical prospects by means of both interactions, namely, interfaces. This is why we need to analyse physical properties of both interactions separately, before we try to combine them. The first step is to stabilize a stable fractional QH phase for at least one of the promising interactions $V_{SF}^{1/2}$. To simplify numerical calculations, we consider the two leg ladder and neglect all $\tau = -$ species, which is what we did for both nearest and next-to-nearest neighbor Hubbard interaction. The full model of this assumption reads

$$\hat{H}_{\tau=+}^I = \Omega \sum_r \hat{a}_{r,+}^\dagger \sigma_x \hat{a}_{r,+} + t \sum_r \left(\hat{a}_{r+1,+}^\dagger \hat{a}_{r,+} e^{-iB/2\sigma_z} + \text{H.c.} \right) + \hat{V}_{SF}^{1/2}. \quad (\text{III.18})$$

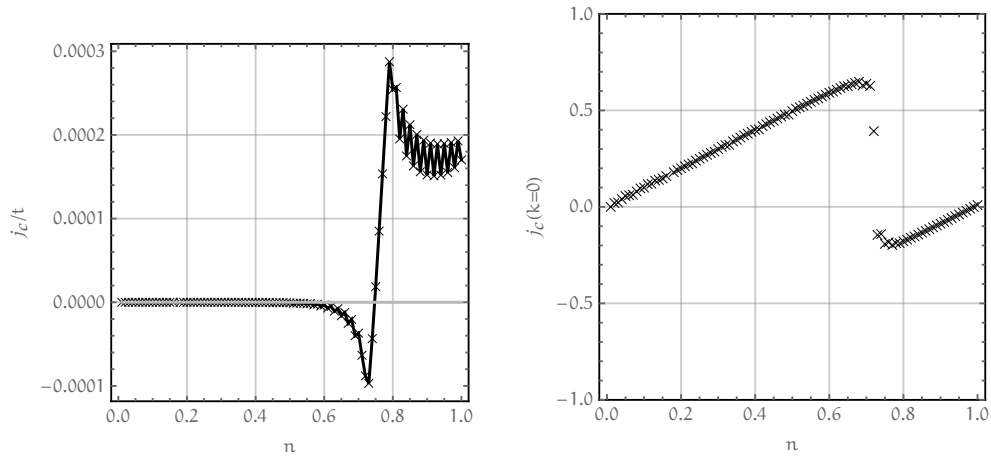


Figure 33: Numerical simulation of noninteracting Hamiltonian and density-assisted spin-flip at $\Omega = 0$, $t = 1$, $B = \frac{3\pi}{4}$ and $U_\Omega = 0.5$. Left: Chiral current of the latter interaction proposal for \mathcal{O}^F , Eq. III.12. Right: Momentum zero current $j_c(k=0)$, introduced in Ch. I.6.

For small $U_\Omega = 0.5$, $\Omega = 0$ and $t = 1$, we face a clear signature of an *iQH* phase - without the non-interacting spin-flip term (see Fig. 33). We notice that the signature of the chiral current is slightly different from non-interacting phases. The momentum zero current deviates significantly from results obtained in Ch. I.6. Instead of $j_c(k=0) \neq 0$ in trivial phases, here it starts and even finishes at exactly zero. When we elaborate $U_\Omega > 1$, we face phase separation issues which we already discussed in this chapter which prevents the numerical methods to explore regions promising for additional phases.

We already have ideas for possible workarounds to avoid phase separation issues: The introduction of small on-site repulsions prevents particles from clus-terization of different local densities. This way we obtain as numerical results slightly alternating occupation patterns dictated from the interactions. On the other hand, by applying simultaneously repulsive and attractive interactions, we actively suppress the emergence of crystalline structures which could be important for topological states. For future works, we need to analyze carefully, if such states are important or not.

IV

SUMMARY

We analyzed properties of a non-interacting fermionic ladder and observed features of the chiral current in a two- and four-leg ladder. We have shown that a special component of the current in momentum space, in particular the momentum zero component, gives rise to a topological order parameter, distinguishing between trivial and nontrivial (QH) phases. In case of the two-leg ladder, we used asymptotic entanglement scaling to verify the central charges $c = 2$ in trivial gapless phases and $c = 1$ for the iQH phase, which is a Luttinger liquid. We explicitly evaluated the reliability of numerical simulations by comparing to analytic solutions.

For the interacting model, a mean-field approximation for nearest neighbor Hubbard interactions predicts additional contributions from the interaction to the chemical potential μ thus "smearing" the interval relevant to numerical observations. For nearest neighbor Hubbard interactions, we observe the emergence of $\nu = 1/2$ phases in a purely fermionic environment. First numerical results for next-to-nearest neighbor interactions verify the emergence and simultaneous coexistence of three resonances $\nu \in \{1/3, 1/2, 1\}$.

We present first numerical results about interaction candidates for the microscopical description of multi-particle operators in Luttinger liquid theory, promising to give rise to emergent fractional QH states in one-dimensional lattices. Observations about the Hubbard model yield fractional phases at the vicinity $U \approx 2 - 5$, but phase separation prevents from numerically accessing regions $U_J, U_\Omega > 2$. We manage to explain the emergence of crystalline phases for density dependent chain- and spin-flip by exploring density profiles of different charge sectors. This observation concludes an effectively attractive character and hence clusterization of particles for low-density sectors in case of both interaction types. Exploring weak-coupling regimes for density dependent spin-flip and chain-flip interactions, the emergence of an additional stable iQH phase has been verified. Signatures in the chiral current and the momentum-zero current show that this topological phase differs from the noninteracting iQH phase.

The emergence of peculiar $\nu = 1/2$ phases might be caused by strange $(p, p') = (1/3, -3/4 - 1)$ operators in Luttinger liquid theory, but we must postpone a careful and detailed theoretical explanation to future work. We plan on simulating a $\nu = 1/3$ Laughlin phase in vicinity of the hard-core limit ($U \rightarrow \infty$) of two-body, nearest neighbor Hubbard interactions. In order to test the intervals given for K_ρ by Bosonization, we have to simulate a larger regime for both nearest and next-to-nearest neighbor Hubbard interaction. Extrapolation of numerical results to the limits $L \rightarrow \infty$ and $M \rightarrow \infty$ will clean the data from tentative finite-size oscillations.

We plan to explore further coupling-regions of the proposed multi-particle operators to find kinks of the chiral currents at the expected resonance $\nu = 1/3$. If we find that the problem resides in simulation of finite-sized systems, we could plan to use algorithms with periodic boundary conditions, or with certain infinite-MPS routines.

A

LUTTINGER LIQUIDS

Whereas we explicitly use Bosonization in Ch. II and Ch. III to identify operator identities which give rise to topological behavior, we hereby want to introduce the reader more into the concept itself. This chapter serves as introductory part to give an idea about Bosonization and Luttinger liquid approaches in general. The first section is a rigorous derivation of the Bosonization identity. We try to focus on book-keeping all fermionic operators and understand, that Bosonization is a very clever way to rewrite fermionic operators in terms of bosonic operators, which are quadratic in fermionic creation and annihilation operators [37, 38, 39, 40, 41].

We then focus on field theoretic arguments which yields more phenomenological Bosonization and the concept of Luttinger liquids, which are the one-dimensional version of Fermi liquids [42].

A.1 CONSTRUCTIVE BOSONIZATION

Let us start with a model of spinless, free fermions with dispersion relation $\epsilon_k = \frac{k^2}{2} + \mu_0$ that reside on a equidistant lattice of size L . Depending on μ_0 and L , the overall ground state is a many-body state of N fermions which occupy all negative energy levels up to a certain momentum where $\epsilon_{k_F} = 0$. This momentum is called the Fermi momentum k_F .

In Fock space excitations are collective single-mode excitations $\hat{c}_{k+q}^\dagger \hat{c}_k |GS\rangle$ that can be expressed with respect to the ground state. These single-mode excitations are particle-hole states and have an excited energy $\Delta E(q)$ with respect to the ground state. Fig. 34 visualizes such particle-hole states $\hat{c}_{k+q}^\dagger \hat{c}_k |GS\rangle$ after momentum-transfer q .

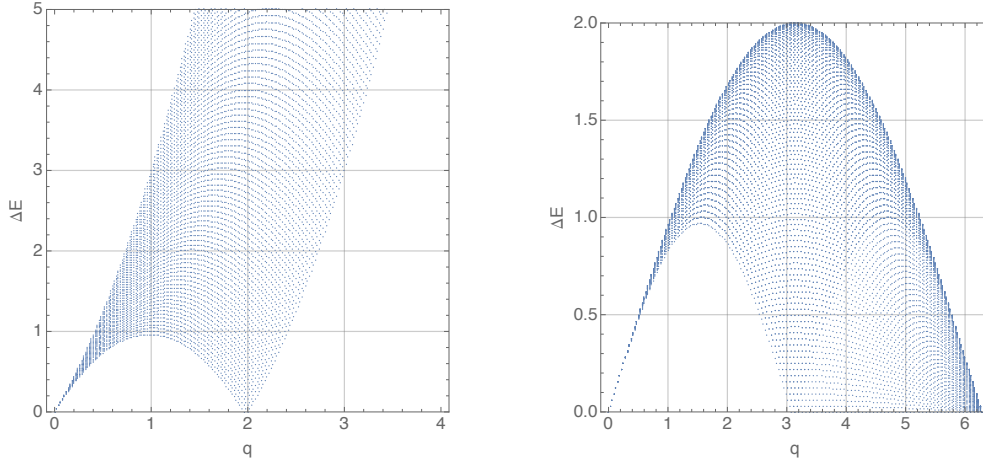


Figure 34: Energy difference $\Delta E(q)$ of single-mode excitations with respect to the ground state energy. Left figure: quadratic dispersion relation. Right figure: cosine dispersion relation.

This allows a reorganization of the overall Fock space with respect to particle-hole operators. Since those operators are quadratic in fermionic operators, they have a bosonic statistics. Before we elaborate details, we have to introduce a certain terminology.

TERMINOLOGY

Let

$$\hat{\Psi}_\eta(x) = \left(\frac{2\pi}{L}\right)^{1/2} \sum_{k=-\infty}^{\infty} e^{-ikx} \hat{c}_{k\eta} \quad (\text{A.1})$$

represent a set of $\eta \in \{1, \dots, M\}$ fermion fields with creation and annihilation operators $\{\hat{c}_{k\eta}, \hat{c}_{k'\eta}^\dagger\} = \delta_{\eta\eta'} \delta_{kk'}$ and introduce boundary conditions to quantize the momenta k

$$\hat{\Psi}_\eta(x + L/2) = e^{i\pi\delta_b} \hat{\Psi}_\eta(x - L/2) \Rightarrow k = \frac{2\pi}{L}(n_k - \delta_b/2). \quad (\text{A.2})$$

In Bosonization it is useful to introduce a different normalization

$$\left\{ \hat{\Psi}_\eta(x), \hat{\Psi}_{\eta'}^\dagger(x') \right\} = \delta_{\eta\eta'} 2\pi \delta(x - x') \quad (\text{A.3})$$

which provides in the end of this introduction convenient commutations for the bosonic fields.

We can relabel the k -space, such that ground states correspond to all $k \leq 0$ modes being occupied. This way, we may define a "vacuum" state

$$\begin{array}{l}
|\vec{0}\rangle_0 \\
\text{-----} 5 \\
\text{-----} 4 \\
\text{-----} 3 \\
\text{-----} 2 \\
\text{-----} 1 \\
\bullet \text{-----} 0 \\
\bullet \text{-----} -1 \\
\bullet \text{-----} -2 \\
\bullet \text{-----} -3 \\
\bullet \text{-----} -4 \\
\bullet \text{-----} -5
\end{array}
\quad
\begin{array}{l}
c_{k\eta} |\vec{0}\rangle_0 = 0 \quad k > 0 \\
c_{k\eta}^\dagger |\vec{0}\rangle_0 = 0 \quad k \leq 0
\end{array}
\tag{A.4}$$

All excitations must be understood with respect to this vacuum state to prevent divergent expressions. The fermion normal order \odot is defined for functions A of compositions of c and \hat{c}^\dagger 's

$$\odot(A) := A -_0 \langle \vec{0} | A | \vec{0} \rangle_0 \tag{A.5}$$

The particle number \vec{N} is the eigenvalue of

$$\hat{N}_\eta := \sum_k \odot(\hat{c}_{k\eta}^\dagger \hat{c}_{k\eta}) = \sum_k \left(\hat{c}_{k\eta}^\dagger \hat{c}_{k\eta} -_0 \langle \vec{0} | \hat{c}_{k\eta}^\dagger \hat{c}_{k\eta} | \vec{0} \rangle_0 \right) \tag{A.6}$$

and gives the amount of particle-hole excitations in a certain state. Since the particle number is well-defined in fermionic environments, it is possible to decompose the Hilbert space in direct sums of subspaces with different particle number

$$\mathcal{F} = \bigoplus_{\vec{N}} \mathcal{H}_{\vec{N}}. \tag{A.7}$$

The \vec{N} particle Hilbert space $\mathcal{H}_{\vec{N}}$ is spanned with vectors of the same \hat{N}_η eigenvalues $\vec{N} = (N_1, \dots, N_M)$. We fix the notation of all ground states to

$$\begin{aligned}
|\vec{N}\rangle_0 &:= (\hat{C}_1)^{N_1} \dots (\hat{C}_M)^{N_M} |\vec{0}\rangle_0 \\
(\hat{C}_\eta)^{N_\eta} &:= \begin{cases} \hat{c}_{N_\eta\eta}^\dagger \hat{c}_{(N_\eta-1)\eta}^\dagger \dots \hat{c}_{1\eta}^\dagger & \text{for } N_\eta > 0 \\ \hat{c}_{(N_\eta+1)\eta} \hat{c}_{(N_\eta+2)\eta} \dots \hat{c}_{0\eta} & \text{for } N_\eta < 0 \\ 1 & \text{for } N_\eta = 0 \end{cases}.
\end{aligned}
\tag{A.8}$$

All excited states in $\mathcal{H}_{\vec{N}}$ can be regarded as particle-hole excitations built on the ground state $|\vec{N}\rangle_0$. Let

$$\hat{b}_{q\eta}^\dagger := \frac{i}{\sqrt{n_q}} \sum_k \hat{c}_{k+q\eta}^\dagger \hat{c}_{k\eta} \quad \hat{b}_{q\eta} := \frac{-i}{\sqrt{n_q}} \sum_k \hat{c}_{k-q\eta}^\dagger \hat{c}_{k\eta} \tag{A.9}$$

with $q := \frac{2\pi}{L} n_q$ and $n_q \in \mathbb{N}$ account for all particle-hole operators that represent a superposition of all possible single-mode excitations with momentum q . In Fig. 35 we show the action of different compositions of b on a spinless $M = 1$

BOSON FIELDS

Providing basic terminology, we are ready to define boson fields in real space

$$\left. \begin{aligned} \hat{\phi}_\eta(x) &:= - \sum_{q>0} \frac{1}{\sqrt{n_q}} e^{-iqx} \hat{b}_{q\eta} e^{-\alpha q/2} \\ \hat{\phi}_\eta^\dagger(x) &:= - \sum_{q>0} \frac{1}{\sqrt{n_q}} e^{iqx} \hat{b}_{q\eta}^\dagger e^{-\alpha q/2} \end{aligned} \right\} \hat{\Phi}_\eta(x) := \hat{\phi}_\eta(x) + \hat{\phi}_\eta^\dagger(x). \quad (\text{A.14})$$

$\alpha > 0$ is a small regularization parameter, necessary to control divergent momentum sums. These divergent sums may occur for commutation relations of boson fields at the same spacial position $x' = x$, e.g.

$$\begin{aligned} [\hat{\phi}_\eta(x), \hat{\phi}_{\eta'}(x')] &= [\hat{\phi}_\eta^\dagger(x), \hat{\phi}_{\eta'}^\dagger(x')] = 0 \\ [\hat{\phi}_\eta(x), \hat{\phi}_{\eta'}^\dagger(x')] &= -\delta_{\eta\eta'} \ln \left(1 - e^{-i\frac{2\pi}{L}(x-x'-\alpha)} \right). \end{aligned} \quad (\text{A.15})$$

It is possible to express the overall electron density in terms of these boson fields

$$\begin{aligned} \rho_\eta(x) &= \odot(\hat{\psi}_\eta^\dagger(x)\hat{\psi}_\eta(x)) = \frac{2\pi}{L} \sum_{k'/k} e^{ix(k'-k)} \odot(\hat{c}_{k'\eta}^\dagger \hat{c}_{k\eta}) \\ &= \frac{2\pi}{L} \sum_{q>0, q<0, q=0} e^{-iqx} \sum_k \odot(\hat{c}_{k-q\eta}^\dagger \hat{c}_{k\eta}) \\ &= \frac{2\pi}{L} \sum_{q>0} i\sqrt{n_q} \left(e^{-iqx} \hat{b}_{q\eta} - e^{iqx} \hat{b}_{q\eta}^\dagger \right) + \frac{2\pi}{L} \sum_k \odot(\hat{c}_{k\eta}^\dagger \hat{c}_{k\eta}) \\ &= \sum_{q>0} \frac{iq}{\sqrt{n_q}} \left(e^{-iqx} \hat{b}_{q\eta} - e^{iqx} \hat{b}_{q\eta}^\dagger \right) + \frac{2\pi}{L} \sum_k \odot(\hat{c}_{k\eta}^\dagger \hat{c}_{k\eta}) \\ &= \partial_x \hat{\phi}_\eta(x) + \frac{2\pi}{L} \hat{N}_\eta \quad (\alpha \rightarrow 0) \end{aligned} \quad (\text{A.16})$$

Using the following commutators

$$\left. \begin{aligned} [\hat{b}_{q\eta'}, \hat{\psi}_\eta(x)] &= \delta_{\eta\eta'} \alpha_q(x) \hat{\psi}_\eta(x) \\ [\hat{b}_{q\eta'}^\dagger, \hat{\psi}_\eta(x)] &= \delta_{\eta\eta'} \alpha_q^*(x) \hat{\psi}_\eta(x) \end{aligned} \right\} \alpha_q(x) = \frac{i}{\sqrt{n_q}} e^{iqx}, \quad (\text{A.17})$$

to find $\hat{b}_{q\eta'} \hat{\psi}_\eta(x) |\vec{N}\rangle_0 = \delta_{\eta\eta'} \alpha_q(x) \hat{\psi}_\eta(x) |\vec{N}\rangle_0$, we can express the action of fermionic fields on ground states in terms of these fields

$$\begin{aligned} \hat{\psi}_\eta(x) |\vec{N}\rangle_0 &= \exp \left(\sum_{q>0} \alpha_q(x) \hat{b}_{q\eta} \right) F_\eta \hat{\lambda}_\eta(x) |\vec{N}\rangle_0, \\ &= e^{-i\hat{\phi}_\eta^\dagger(x)} F_\eta \hat{\lambda}_\eta(x) |\vec{N}\rangle_0 \end{aligned} \quad (\text{A.18})$$

with $\hat{\lambda}_\eta(x) = \sqrt{\frac{2\pi}{L}} e^{-i\frac{2\pi}{L}(N_\eta - \delta_b/2)x}$. We visualize this action in Fig. 36.

$$\begin{aligned}
\psi(x)|0\rangle_0 &= \begin{array}{c} \text{---} \\ \text{---} \\ \text{---} \\ \bullet \\ \text{---} \\ \text{---} \\ \text{---} \\ \text{---} \\ \text{---} \\ \text{---} \end{array} + e^{i\frac{2\pi}{L}x} \begin{array}{c} \text{---} \\ \text{---} \\ \text{---} \\ \bullet \\ \text{---} \\ \text{---} \\ \text{---} \\ \text{---} \\ \text{---} \\ \text{---} \end{array} + e^{i\frac{4\pi}{L}x} \begin{array}{c} \text{---} \\ \text{---} \\ \text{---} \\ \bullet \\ \text{---} \\ \text{---} \\ \text{---} \\ \text{---} \\ \text{---} \\ \text{---} \end{array} + \dots \\
e^{-i\varphi^\dagger(x)}F|0\rangle_0 &= \begin{array}{c} \text{---} \\ \text{---} \\ \text{---} \\ \bullet \\ \text{---} \\ \text{---} \\ \text{---} \\ \text{---} \\ \text{---} \\ \text{---} \end{array} - e^{i\frac{2\pi}{L}x} \begin{array}{c} \text{---} \\ \text{---} \\ \text{---} \\ \bullet \\ \text{---} \\ \text{---} \\ \text{---} \\ \text{---} \\ \text{---} \\ \text{---} \end{array} + \frac{e^{i\frac{4\pi}{L}x}}{2} \left(\begin{array}{c} \text{---} \\ \text{---} \\ \text{---} \\ \bullet \\ \text{---} \\ \text{---} \\ \text{---} \\ \text{---} \\ \text{---} \\ \text{---} \end{array} + \begin{array}{c} \text{---} \\ \text{---} \\ \text{---} \\ \bullet \\ \text{---} \\ \text{---} \\ \text{---} \\ \text{---} \\ \text{---} \\ \text{---} \end{array} - \begin{array}{c} \text{---} \\ \text{---} \\ \text{---} \\ \bullet \\ \text{---} \\ \text{---} \\ \text{---} \\ \text{---} \\ \text{---} \\ \text{---} \end{array} - \begin{array}{c} \text{---} \\ \text{---} \\ \text{---} \\ \bullet \\ \text{---} \\ \text{---} \\ \text{---} \\ \text{---} \\ \text{---} \\ \text{---} \end{array} \right) + \dots
\end{aligned}$$

Figure 36: We show different actions of the particle-hole operators defined in Eq. A.9. Bottom figure: explicit construction of a single-mode excitation with a composition of particle-hole operators, acting on a spinless fermionic ground state $N = 0$.

In general, one can prove [37] the Bosonization identity

$$\begin{aligned}
\hat{\psi}_\eta(x)|\vec{N}\rangle &= \hat{\psi}_\eta(x)f\left(\left\{\hat{b}_{q\eta'}^\dagger\right\}\right)|\vec{N}\rangle_0 \stackrel{\text{some commutation relations}}{=} \\
&= F_\eta \sqrt{\frac{2\pi}{L}} e^{-i\frac{2\pi}{L}(\hat{N}_\eta - \delta_b/2)x} e^{-i\hat{\varphi}_\eta^\dagger(x)} e^{-i\hat{\varphi}_\eta(x)} |\vec{N}\rangle \\
&= \frac{F_\eta}{\sqrt{a}} e^{-i\hat{\Phi}_\eta(x)} |\vec{N}\rangle
\end{aligned} \tag{A.19}$$

where $\hat{\Phi}_\eta(x) := \hat{\varphi}_\eta(x) + \frac{2\pi}{L}(\hat{N}_\eta - \delta_b/2)x$.

LINEARIZATION OF $\epsilon(p)$

This section discusses in detail all steps necessary to apply the constructive approach to Bosonization. We consider only one species of fermions to provide a most basic application example.

The real fermionic field operators can be expressed as

$$\hat{\Psi}(x) = \sqrt{\frac{2\pi}{L}} \sum_{p=0}^{\infty} e^{-ipx} \hat{c}_{-p} + e^{ipx} \hat{c}_p, \tag{A.20}$$

where each plain wave occupies a different energy $\epsilon(p)$. The energy of free free left- and right-moving, spinless electron modes is given by

$$\epsilon(p) = \frac{p^2 - p_F^2}{2m}. \tag{A.21}$$

Since low-energy processes consider only modes in the vicinity of $\epsilon(p_F) = 0$, we continue with a first approximation to proceed further. We want to define a vacuum state in momentum space as introduced in Eq. A.4. Due to the quadratic dispersion, the model has two Fermi points at $\pm|p_F|$. In terms of these points ($k_F := |p_F|$)

$$\hat{\Psi}(x) = \sqrt{\frac{2\pi}{L}} \sum_{k=-k_F}^{\infty} e^{-i(k+k_F)x} \hat{c}_{-k-k_F} + e^{i(k+k_F)x} \hat{c}_{k+k_F}, \tag{A.22}$$

we observe that the momentum space is bounded from below. In order to respect again requirements for Bosonization we do need some further assumptions. To continue the dispersion for unbounded momenta, we assume

$$\epsilon(p) \approx \epsilon_L(p) + \epsilon_R(p), \tag{A.23}$$

with linear dispersion $\epsilon_{L/R}(p) \cdot m = p \mp |p_F|$. The explanation of " \approx " will follow at the end of this section. We introduce a shift in k for left- and right-moving modes, namely

$$\hat{c}_{L/R,k} := \hat{c}_{\mp(k+k_F)}. \quad (\text{A.24})$$

The original fermion modes can be expressed in terms of this modes

$$\hat{\Psi}(x) = \sqrt{\frac{2\pi}{L}} \sum_{k=-k_F}^{\infty} e^{-ik_F x} e^{-ikx} \hat{c}_{L,k} + e^{ik_F x} e^{i(k+k_F)x} \hat{c}_{R,k}. \quad (\text{A.25})$$

Finally, we introduce two fermionic fields that slowly vary for k_F -processes $\psi_{L/R}(x) := \sqrt{\frac{2\pi}{L}} \sum_{-\infty}^{\infty} e^{\mp ikx} \hat{c}_{L/R,k}$

$$\hat{\Psi}(x) \approx e^{-ik_F x} \psi_L(x) + e^{ik_F x} \psi_R(x). \quad (\text{A.26})$$

The relabelling from $p \rightarrow k$ for left- and right-movers is picturized in Fig. 37.

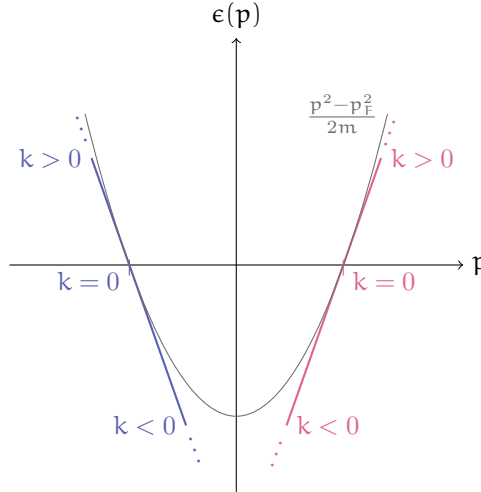


Figure 37: Linearization process of the dispersion relation in Eq. A.23.

The last step to conclude Eq. A.26 requires the extension of the linearized dispersion relations for $\epsilon_{L/R}(p \lesseqgtr 0)$, which also dramatically extends the Fermi-sea with an infinite number of modes. For a mathematically well-defined theory, we need to impose a quantization condition for k to reduce the momentum space to a countable-infinite set of momenta. Assuming (anti-)PBC, the quantization arises from $\psi_{\eta}(L/2) = (-)^{\eta} \psi_{\eta}(-L/2) \Rightarrow k \in \frac{2\pi}{L} \cdot \mathbb{Z}$.

All conditions to apply Bosonization are now satisfied and we may introduce a set of two commuting boson fields for the right and left movers respectively.

These fields become upon using Eq. A.19 for the distinct left- right-mover species $\eta \in \{L/R\}$

$$\begin{aligned}\phi_{L/R} &:= - \sum_{n_q \in \mathbb{Z}^+} \frac{1}{n_q} e^{-\alpha q/2} \left[e^{\mp i q x} b_{q,L/R} + e^{\pm i q x} b_{q,L/R}^\dagger \right] \quad (q = \frac{2\pi}{L} n_q), \\ \psi_{L/R} &:= \sqrt{\alpha} \hat{F}_{L/R} e^{\mp i \frac{2\pi}{L} (\hat{N}_{L/R} - 1/2\delta_b) x} e^{-i\phi_{L/R}}, \\ \rho_{L/R} &:= \pm \partial_x \phi_{L/R} + \frac{2\pi}{L} \hat{N}_{L/R}.\end{aligned}\tag{A.27}$$

The approximation " \approx " is valid for low-energy scattering processes since almost all artificial modes occupy energies far below the Fermi-level and hence do not contribute anyway. This approximation has a consequence: model-specific properties which uniquely define $\epsilon(p)$ may become lost in the process.

After this constructive construction of bosonized fields and the intuitive understanding in terms of particle-hole operators, we now want to make the connection to the field theoretic description, which we use in Ch. II and Ch. III.

A.2 PHENOMENOLOGICAL BOSONIZATION

In the previous section, we saw a careful application of Bosonization formulas for free fermions. We explicitly show that, the validity of these formulas require, strictly speaking, a linearization of the dispersion relation and are only valid for theories which are confined close to the Fermi level. Without explicitly recapitulating the vast consequences of further application, namely solutions for interacting cases (for more details, [42]), one may wonder what will become of the results when interactions are strong and enlarge the confinement to points beyond the Fermi level.

The density operator of a one-dimensional system of bosons and fermions reads

$$\rho(x) = \sum_i \delta(x - x_i).\tag{A.28}$$

Here x_i is the position of the i^{th} particle. Let the "equilibrium" position of a perfect crystalline lattice be denoted by R_i^0 and displacement u_i relative to this position, then

$$x_i = R_i^0 + u_i.\tag{A.29}$$

If the average density is n , $d = 1/n$ is the mean distance between particles. This gives $R_i^0 = d \cdot i$ for the equilibrium position of the i^{th} particle. However, the notation of Eq. A.28 is not convenient. The brilliant idea [43] is to replace a labelling field, we call it $\theta_1(x)$, which relates to the position of the i^{th} particle

$$\theta_1(x_i) := 2\pi i.\tag{A.30}$$

This field is well-defined in one-dimensional systems, because numbering of a countable set of particles is always possible. We now may use the property of the delta function

$$\delta(f(x)) = \sum_{x_i \in \text{Ker}(f)} \frac{1}{|f'(x_i)|} \delta(x - x_i), \quad (\text{A.31})$$

to rewrite the density as a function of θ_l

$$\rho(x) = \sum_i \delta(x - x_i) = |\partial_x \theta_l(x)| \sum_i \delta(\theta_l(x) - 2\pi i) \quad (\text{A.32})$$

$$= |\partial_x \theta_l(x)| \frac{1}{2\pi} \sum_p e^{ip\theta_l(x)}. \quad (\text{A.33})$$

The first expression coincides on lattice positions x_i , since the single element in the kernel of the argument of δ is indeed at position x_i . The last expression in Eq. A.33 follows from a Fourier series of the delta function. To get a feeling about the idea of θ_l , let us consider the following scenario. Assume a set of N atoms sitting on an one-dimensional stripe at arbitrary positions $\{x_i\}_{i=1\dots N}$. The density function θ_l has to satisfy relation Eq. A.30 and it is always possible to choose it to be strictly monotonically increasing. This is why we may aswell neglect $|\cdot|$ around the partial derivative. Whenever $\theta_l(x)$ passes a particle, it increases by an additional "weight" 2π . θ_l is therefore a continuous function mimicking the behavior of ρ (which is discrete).

In the literature, it is more convenient to define θ with respect to the crystalline structure in order to capture only "fluctuations" around the mean density, i.e.

$$\theta_l(x) = 2(\pi n x - \theta(x)). \quad (\text{A.34})$$

Since the density operator at different position commutes with itself, it is natural to require the same for θ . Thus, the density becomes

$$\rho(x) = \left[n - \frac{1}{\pi} \partial_x \theta(x) \right] \sum_p e^{i2p(\pi n x - \theta(x))}. \quad (\text{A.35})$$

The density average over a large range compared to the mean particle distance $d = 1/2$ has a smeared form due to oscillations apart from $p = 0$ terms

$$\rho(x) \approx n - \frac{1}{\pi} \partial_x \theta(x). \quad (\text{A.36})$$

It is possible to define the creation operator of a bosonic mode at position x as

$$\psi^\dagger(x)_B = \sqrt{\rho(x)} e^{-i\phi(x)}, \quad (\text{A.37})$$

with some operator ϕ that has to be introduced to satisfy the bosonic commutation relations

$$\left[\psi^\dagger(x)_B, \psi(x')_B \right] = \delta(x' - x). \quad (\text{A.38})$$

We must require the proper commutation relation between density ρ and auxiliary field θ to satisfy A.38. If we assume $[\phi(x), \phi(x')] = 0$, we can satisfy A.38 upon requiring

$$[\rho(x), e^{-i\phi(x')}] = \delta(x' - x)e^{-i\phi(x')}. \quad (\text{A.39})$$

Since the fields $\theta(x)$ and similarly $\phi(x)$ are expected to vary on a scale of $1/n$, we can approximate the density $\rho(x)$ with the smeared density $n - \frac{1}{\pi}\partial_x\theta(x)$, and obtain a commutation relation for the bosonic fields

$$\left[-\frac{1}{\pi}\partial_x\theta(x), e^{-i\phi(x')}\right] = \delta(x - x')e^{-i\phi(x')}, \quad (\text{A.40})$$

which is satisfied if we ensure

$$[\partial_x\theta(x), \phi(x')] = -i\pi\delta(x - x'), \quad (\text{A.41})$$

and upon integration

$$[\phi(x), \theta(x')] = i\pi\Theta(x' - x). \quad (\text{A.42})$$

Many authors state (without further proof) that $\rho(x) = A\sqrt{\rho(x)}$ with a normalization constant A . Without digging into much detail, they argue the existence of such a normalization constant from representatives of the delta function, i.e.

$$\sqrt{\delta_\epsilon(x)} = \sqrt{\lim_{\epsilon \rightarrow 0} A' e^{-|x|/\epsilon}} = \lim_{\epsilon \rightarrow 0} \sqrt{A' e^{-|x|/(2\epsilon)}} = 1/\sqrt{A'}\delta_\epsilon(x). \quad (\text{A.43})$$

This is why we arrive at the final expression for bosonic fields

$$\psi^\dagger(x)_B = \sqrt{n - \frac{1}{\pi}\partial_x\theta(x)} \sum_p e^{i2p(\pi nx - \theta(x))} e^{-i\phi(x)}. \quad (\text{A.44})$$

To arrive instead at fermionic fields, we need to ensure anticommutation between ψ^\dagger and ψ . This can be easily included in the definition, since $e^{i\phi_1(x)/2} = \pm 1$. For consecutive particles, an exchange of the two fermions must yield a -1 in the overall expression, which is ensured, if

$$\psi^\dagger(x)_F = \psi^\dagger(x)_B e^{i\phi_1(x)/2}. \quad (\text{A.45})$$

With this, we arrive at two almost identical expressions for fermions *and* bosons:

$$\psi^\dagger(x)_{B/F} = \sqrt{n - \frac{1}{\pi}\partial_x\theta(x)} \sum_{\text{even/odd } p \in \mathbb{Z}} e^{ip(\pi nx - \theta(x))} e^{-i\phi(x)}. \quad (\text{A.46})$$

This is the convention we are using in Ch. II, III, when we introduce $2k_F = \pi n$.

B

SUPPLEMENTARY MATERIAL

We provide additional material which is appended for any readers convenience. A introductory section presents Jordan-Wigner maps from fermionic to bosonic models and vice versa. We provide [MPO](#) representations for the non-interacting and density-assisted interacting Hamiltonian. We restrict the visualization to space-independent, local Hamiltonians of dimension 2^4 - the generalization to a space-dependent form is straightforward. In case of wondering, we perform a Majorana-transformation of the noninteracting model which does not yield further insights.

B.1 JORDAN-WIGNER TRANSFORMATION

In order to solve fermionic Hamiltonians numerically, one has to map actions of fermionic modes to a computational basis to then diagonalize the matrix representation of this action. Take for example a system of only two sites, the following relations can define our matrix representations

$$\begin{aligned} a_2^\dagger a_1^\dagger |\vec{0}\rangle &= -a_1^\dagger a_2^\dagger |\vec{0}\rangle & a_2^\dagger a_2^\dagger |\vec{0}\rangle &= a_1^\dagger a_1^\dagger |\vec{0}\rangle = 0 \\ a_1^\dagger |\vec{0}\rangle &= |10\rangle & a_2^\dagger |\vec{0}\rangle &= |01\rangle \\ a_2^\dagger |10\rangle &= -|11\rangle & a_1^\dagger |01\rangle &= |11\rangle \\ a_1^\dagger &= \begin{pmatrix} 0 & 0 & 1 & 0 \\ 0 & 0 & 0 & 1 \\ 0 & 0 & 0 & 0 \\ 0 & 0 & 0 & 0 \end{pmatrix} = \sigma^+ \otimes \mathbb{1} & a_2^\dagger &= \begin{pmatrix} 0 & -1 & 0 & 0 \\ 0 & 0 & 0 & 0 \\ 0 & 0 & 0 & 1 \\ 0 & 0 & 0 & 0 \end{pmatrix} = -\sigma^z \otimes \sigma^+ \end{aligned} \tag{B.1}$$

which depend on the choice and order of basis (here: $\{|11\rangle, |10\rangle, |01\rangle, |00\rangle\}$). This motivates the search for a canonical map from

$$a_j \rightarrow \sigma_j^- \quad a_j^\dagger \rightarrow \sigma_j^+ \tag{B.2}$$

which is a formal change from fermionic α_j^\dagger to bosonic σ_j^+ operators acting on different Hilbert spaces. We arranged the basis in such a way, that our transformation reads

$$\alpha_j^\dagger = \left(\prod_{i < j} -\sigma_i^z \right) \sigma_j^+ \quad \alpha_j = \left(\prod_{i < j} -\sigma_i^z \right) \sigma_j^-, \quad (\text{B.3})$$

which is the favorable choice for a transformation of Hamiltonians with nearest neighbor terms (we will see this later).

Since the typical Jordan-Wigner string in the bulk of the chain is a non-local collection of Pauli matrices, a proper ordering has to be defined, when we want to transform systems of higher dimensionality. To introduce a better enumeration, we choose $\mathcal{J} := \{\pm 1\}^2 = \{(++), (+-), (-+), (---)\} = \{1, 2, 3, 4\}$ and relabel the fermionic operators from $\alpha_{\tau\sigma,r} \rightarrow \alpha_{i,r}$ with $i \in \mathcal{J}$. The most canonical order has been already picturized in Fig. 3. We notice, that we need four commuting sets of Pauli matrices $\{\sigma_{i,j}^x, \sigma_{i,j}^y, \sigma_{i,j}^z\}$ which act locally at site j of subchain i . Now we can properly introduce a choice for the Jordan-Wigner transformation in these quasi 1D systems.

$$\begin{aligned} \alpha_{i,j} &= \left(\bigotimes_{\substack{j' < j \\ i' \in \mathcal{J}}} -\sigma_{i',j'}^z \right) \left(\bigotimes_{i' < i} -\sigma_{i',j}^z \right) \otimes \sigma_{i,j}^- \\ \alpha_{i,j}^\dagger &= \left(\bigotimes_{\substack{j' < j \\ i' \in \mathcal{J}}} -\sigma_{i',j'}^z \right) \left(\bigotimes_{i' < i} -\sigma_{i',j}^z \right) \otimes \sigma_{i,j}^+. \end{aligned} \quad (\text{B.4})$$

In this expression, we neglected the explicit notation of identities at the right hand sides and we want to emphasize that the order of elements in \mathcal{J} indeed matters. The spin ladder operators $\sigma_{\tau\sigma,i}^\pm$ are locally anticommuting, off-site commuting and satisfy a bosonic hard core condition

$$\begin{aligned} \left\{ \sigma_{i,j}^+, \sigma_{i,j}^- \right\} = id \quad \left[\sigma_{i,j}^+, \sigma_{i',j'}^- \right] = 0 \quad \text{for} \quad \begin{cases} i \neq i' \\ j \neq j' \end{cases} \\ \sigma_{i,j}^{+2} = \sigma_{i,j}^{-2} = 0. \end{aligned} \quad (\text{B.5})$$

Note that the introduced matrix representations indeed satisfy fermionic anti-commutation relations (as they should), since

$$\begin{aligned}
a_{i,j}^\dagger a_{i,j} &= \left(\bigotimes_{\substack{j' < j \\ i' \in \mathcal{J}}} \sigma_{i',j'}^z \right)^2 \left(\bigotimes_{i' < i} \sigma_{i',j}^z \right)^2 \otimes \sigma_{i,j}^+ \sigma_{i,j}^- \\
&= \left(\bigotimes_{\substack{j' < j \\ i' \in \mathcal{J}}} id_{i',j'} \right) \left(\bigotimes_{i' < i} id_{i',j} \right) \otimes \frac{1}{2} (id_{i,j} + \sigma_{i,j}^z) \\
a_{i,j} a_{i,j}^\dagger &= \left(\bigotimes_{\substack{j' < j \\ i' \in \mathcal{J}}} \sigma_{i',j'}^z \right)^2 \left(\bigotimes_{i' < i} \sigma_{i',j}^z \right)^2 \otimes \sigma_{i,j}^- \sigma_{i,j}^+ \\
&= \left(\bigotimes_{\substack{j' < j \\ i' \in \mathcal{J}}} id_{i',j'} \right) \left(\bigotimes_{i' < i} id_{i',j} \right) \otimes \frac{1}{2} (id_{i,j} - \sigma_{i,j}^z)
\end{aligned} \tag{B.6}$$

Furthermore they inherit the hard core condition $a_{i,j}^2 = 0$ from the bosonic creation and annihilation operators. From the previous calculations it is quite obvious that the matrix representations are an unnecessary burden in analytical contexts, hence let us work with the operator formulation of the Jordan-Wigner transform where we can forget about trivial operations.

$$a_{i,j}^\dagger = \sigma_{i,j}^+ \left(\prod_{\substack{j' < j \\ i' \in \mathcal{J}}} -\sigma_{i',j'}^z \right) \left(\prod_{i' < i} -\sigma_{i',j}^z \right) \tag{B.7}$$

$$a_{i,j} = \left(\prod_{i' < i} -\sigma_{i',j}^z \right) \left(\prod_{\substack{j' < j \\ i' \in \mathcal{J}}} -\sigma_{i',j'}^z \right) \sigma_{i,j}^- \tag{B.8}$$

The operator

$$\Phi_{i,j} := \left(\prod_{\substack{j' < j \\ i' \in \mathcal{J}}} -\sigma_{i',j'}^z \right) \tag{B.9}$$

is often referred to as Jordan–Wigner string, kink or soliton operator. For different sites and different sublattice (assume $j < l$),

$$\begin{aligned}
 a_{i,j}^\dagger a_{k,l} &= \sigma_{i,j}^+ \cdot \Phi_{i,j}^\dagger \Phi_{k,l} \cdot \sigma_{k,l}^- \\
 &= \sigma_{i,j}^+ \cdot \Phi_{i,j}^\dagger \left(\prod_{\substack{i' \geq i \\ m \in \mathcal{J}}} \sigma_{i',j}^z \right) \left(\prod_{\substack{j < n < l \\ m \in \mathcal{J}}} \sigma_{m,n}^z \right) \Phi_{k,l} \cdot \sigma_{k,l}^- \\
 &= \sigma_{i,j}^+ \cdot \Phi_{k,l}^\dagger \Phi_{i,j} \cdot \sigma_{k,l}^- = -\Phi_{k,l}^\dagger \sigma_{k,l}^+ \sigma_{i,j}^- \Phi_{i,j} \\
 &= -\Phi_{k,l} \sigma_{i,j}^- \sigma_{k,l}^+ \Phi_{i,j}^\dagger = -a_{k,l} a_{i,j}^\dagger,
 \end{aligned} \tag{B.10}$$

since those operators commute off-site (and off-subchain) and $\{\sigma_j^\pm, \sigma_j^z\} = 0$. Note, that the product of those two strings results in

$$\Phi_{i,j} \Phi_{k,l} = \left(\prod_{k' \geq i \in \mathcal{J}} -\sigma_{k',j}^z \right) \left(\prod_{\substack{j < l' < l \\ k' \in \mathcal{J}}} -\sigma_{k',l'}^z \right) \left(\prod_{k' < k} -\sigma_{k',l}^z \right) \tag{B.11}$$

which is a trivial operation on the first $j - 1$ sites and at site j on the first $i - 1$ subsites since the two strings overlap. This makes it easy to work with graphs when transforming a Hamiltonian with many coupling terms. The previous example could be drawn as shown in the next figure. Let us now rewrite the

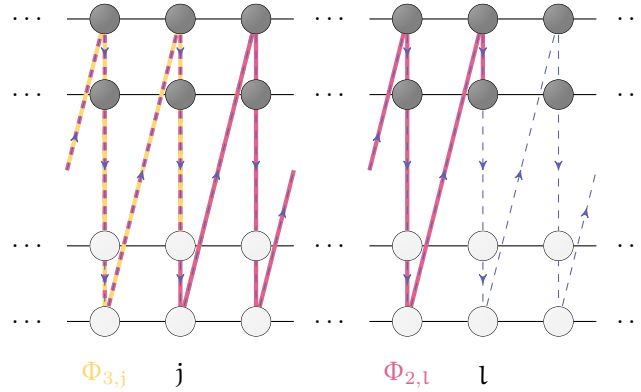


Figure 38: Product of two Jordan-Wigner strings $\Phi_{3,j}$ and $\Phi_{2,j}$. In Regions where the lines overlap, the product of both strings is the identity.

proposed Hamiltonian with this transformation to the spin language.

B.2 REFORMULATION TO MPO

We use the notation introduced in Ch. B.1 to transform all individual terms of the Hamiltonian.

CHEMICAL POTENTIAL

The term that is most easy to transform $\hat{a}_r^\dagger(\mu\tau_z + \mu_0)\hat{a}_r =: \hat{a}_r^\dagger\tilde{\mu}\hat{a}_r$ becomes since $\tilde{\mu} = (\tilde{\mu}_{i,k}\delta_{i,k})_{i,k\in\mathcal{J}}$

$$\hat{a}_{i,j}^\dagger\tilde{\mu}_{i,k}\hat{a}_{k,j} = \tilde{\mu}_{i,i}\sigma_{i,j}^+\Phi_{i,j}^\dagger\Phi_{i,j}\sigma_{i,j}^- = \tilde{\mu}_{i,i}\sigma_{i,j}^+\sigma_{i,j}^- . \quad (\text{B.12})$$

SPIN FLIP

For the spin flip and tunneling contributions, the Wigner string acts nontrivially, i.e.

$$\hat{a}_{i,j}^\dagger\tilde{\Omega}_{i,k}\hat{a}_{k,j} = \Omega(\delta_{k,2}^{i,1} + \delta_{k,1}^{i,2} + \delta_{k,4}^{i,3} + \delta_{k,3}^{i,4})\sigma_{i,j}^+\Phi_{i,j}^\dagger\Phi_{k,j}\sigma_{k,j}^- , \quad (\text{B.13})$$

where the first term is explicitly

$$\Omega\sigma_{1,j}^+\Phi_{1,j}^\dagger\Phi_{2,j}\sigma_{2,j}^- = \sigma_{1,j}^+(-\sigma_{1,j}^z)\sigma_{2,j}^- = \sigma_{1,j}^+\sigma_{2,j}^- . \quad (\text{B.14})$$

Here we notice the beauty of our choice of the Jordan-Wigner string - we get rid of the emerging minus signs. The remaining three terms result in quite similar expressions

$$\hat{a}_{i,j}^\dagger\tilde{\Omega}_{i,k}\hat{a}_{k,j} = \Omega \cdot (\sigma_{1,j}^+\sigma_{2,j}^- + \sigma_{1,j}^-\sigma_{2,j}^+ + \sigma_{3,j}^+\sigma_{4,j}^- + \sigma_{3,j}^-\sigma_{4,j}^+) . \quad (\text{B.15})$$

INTER-CHAIN TUNNELING

The tunneling term reads

$$\begin{aligned} \hat{a}_{i,j}^\dagger\tilde{J}_{i,k}\hat{a}_{k,j} &= J(\delta_{k,3}^{i,1} + \delta_{k,1}^{i,3} + \delta_{k,4}^{i,2} + \delta_{k,2}^{i,4})\Phi_{i,j}^\dagger\sigma_{i,j}^+\sigma_{k,j}^-\Phi_{k,j} , \\ \hat{a}_{i,j}^\dagger\tilde{J}_{i,k}\hat{a}_{k,j} &= -J \cdot (\sigma_{1,j}^+\sigma_{2,j}^z\sigma_{3,j}^- + \sigma_{1,j}^-\sigma_{2,j}^z\sigma_{3,j}^+ \\ &\quad + \sigma_{2,j}^+\sigma_{3,j}^z\sigma_{4,j}^- + \sigma_{2,j}^-\sigma_{3,j}^z\sigma_{4,j}^+) \end{aligned} \quad (\text{B.16})$$

where an additional $-\sigma^z$ appears despite the fact that it appears at first glance as on-site transition. This is due to the fact that this term is technically a next-nearest neighbor transition because we anticipated an internal structure of four subchains and introduced its Wigner-String as stated in the introductory chapter for Jordan-Wigner transformations.

INTRA-CHAIN TUNNELING

The hopping term can be rewritten with a diagonal matrix T to $\hat{a}_{r+1}^\dagger\tau_z \otimes e^{-i\sigma_z^B} \hat{a}_r =: \hat{a}_{r+1}^\dagger T \hat{a}_r$ which simplifies the calculation to

$$\begin{aligned} \hat{a}_{i,j+1}^\dagger T_{i,k} \hat{a}_{k,j} &= T_{i,i}\sigma_{i,j+1}^+ \left(\prod_{i' < i \in \mathcal{J}} -\sigma_{i',j+1}^z \right) \\ &\quad \cdot \left(\prod_{i' > i \in \mathcal{J}} -\sigma_{i',j}^z \right) \sigma_{i,j}^- . \end{aligned} \quad (\text{B.17})$$

The previous calculations yield the transformed non-interacting Hamiltonian in the spin language

$$\begin{aligned} \hat{H} = & \sum_{j=1}^L T_{i,i} \sigma_{i,j+1}^+ \left(\prod_{i' < i \in \mathcal{J}} -\sigma_{i',j+1}^z \right) \left(\prod_{i' > i \in \mathcal{J}} -\sigma_{i',j}^z \right) \sigma_{i,j}^- + \text{h.c.} + \\ & -J \cdot \left(\sigma_{1,j}^+ \sigma_{2,j}^z \sigma_{3,j}^- + \sigma_{1,j}^- \sigma_{2,j}^z \sigma_{3,j}^+ + \sigma_{2,j}^+ \sigma_{3,j}^z \sigma_{4,j}^- + \sigma_{2,j}^- \sigma_{3,j}^z \sigma_{4,j}^+ \right) + \\ & \Omega \cdot \left(\sigma_{1,j}^+ \sigma_{2,j}^- + \sigma_{1,j}^- \sigma_{2,j}^+ + \sigma_{3,j}^+ \sigma_{4,j}^- + \sigma_{3,j}^- \sigma_{4,j}^+ \right) + \\ & \tilde{\mu}_{i,i} \sigma_{i,j}^+ \sigma_{i,j}^- \end{aligned} \quad (\text{B.18})$$

HUBBARD INTERACTION

The Jordan-Wigner transform of density-density interactions is very easy due to the absence of any string operator. We just have to evaluate all terms which yield any coupling:

$$\hat{V}^H(\xi) = \sum_{ij} U_{ij}(\hat{\rho}, \xi). \quad (\text{B.19})$$

In the scope of this thesis, we restricted U_{ij} to two cases

$$U_{ii} = \frac{U}{2} \sum_{\tau} \hat{\rho}_{i,\tau} (\hat{\rho}_{i,\tau} - 1), \quad (\text{B.20})$$

$$U_{i,j} = U \delta_{j,i+\xi} \sum_{\tau} \hat{\rho}_{i,\tau} \hat{\rho}_{j,\tau}. \quad (\text{B.21})$$

The Jordan-Wigner transform of $\hat{\rho}_{i,j} = \sigma_{i,j}^+ \sigma_{i,j}^-$ and $\rho_{i,\tau}$ becomes

$$\hat{\rho}_{i,\tau} = \sum_{\sigma} \hat{\rho}_{i,\tau\sigma} = \sum_{j \in \mathcal{J}_{\tau}} \sigma_{i,j}^+ \sigma_{i,j}^-, \quad (\text{B.22})$$

where we introduced the subset of

$$\mathcal{J}_{\tau=+} := \{1, 2\} \quad \text{and} \quad \mathcal{J}_{\tau=-} := \{3, 4\}. \quad (\text{B.23})$$

Therefore, Eq. B.20 becomes

$$\begin{aligned} \frac{U}{2} \sum_{\tau} \hat{\rho}_{i,\tau} (\hat{\rho}_{i,\tau} - 1) &= \sum_{\tau} U \hat{\rho}_{i,\tau+} \hat{\rho}_{i,\tau-} \\ &= U \left(\sigma_{i,1}^+ \sigma_{i,1}^- \sigma_{i,2}^+ \sigma_{i,2}^- + \sigma_{i,3}^+ \sigma_{i,3}^- \sigma_{i,4}^+ \sigma_{i,4}^- \right), \end{aligned} \quad (\text{B.24})$$

and Eq. B.21 is a little more complicated

$$\begin{aligned} U_{i,j} &= U \delta_{j,i+\xi} \sum_{\tau} \hat{\rho}_{i,\tau} \hat{\rho}_{j,\tau} \\ &= U \delta_{j,i+\xi} \left((\sigma_{i,1}^+ \sigma_{i,1}^- + \sigma_{i,2}^+ \sigma_{i,2}^-) (\sigma_{j,1}^+ \sigma_{j,1}^- + \sigma_{j,2}^+ \sigma_{j,2}^-) \right. \\ &\quad \left. + (\sigma_{i,3}^+ \sigma_{i,3}^- + \sigma_{i,4}^+ \sigma_{i,4}^-) (\sigma_{j,3}^+ \sigma_{j,3}^- + \sigma_{j,4}^+ \sigma_{j,4}^-) \right). \end{aligned} \quad (\text{B.25})$$

The Jordan-Wigner transform does not really complicate the interactions - the τ contributions remain decoupled. It is just a map to a computational basis which we use in our calculations.

DENSITY ASSISTED SPIN-FLIP

One promising interaction term is constructed via density assisted spin-flip operators, which reads

$$\rho_{\uparrow,\tau}(r)\rho_{\downarrow,\tau}(r) \left[\mathbf{a}_{\tau}^{\dagger}(r+1)(\cos(4k_f)\mathbb{1} \otimes \sigma_x - \sin(4k_f)\tau_z \otimes \sigma_y)\mathbf{a}_{\tau}(r+1) + \mathbf{a}_{\tau}^{\dagger}(r-1)(\cos(4k_f)\mathbb{1} \otimes \sigma_x + \sin(4k_f)\tau_z \otimes \sigma_y)\mathbf{a}_{\tau}(r-1) \right], \quad (\text{B.26})$$

where \mathbf{a}_{τ} is a collection of $(\mathbf{a}_{\tau\sigma})_{\sigma}$. Relabelling $\tau\sigma$ as introduced, we accomplish the form

$$\mathcal{F}_{i,j} = \rho_{i,j}\rho_{i+1,j} \sum_{k \in \mathcal{S}_i} \left[\mathbf{a}_{i,j+1}^{\dagger} \Lambda_{i,k} \mathbf{a}_{k,j+1} + \mathbf{a}_{i+1,j+1}^{\dagger} \Lambda_{i+1,k} \mathbf{a}_{k,j+1} + \mathbf{a}_{i,j-1}^{\dagger} \Lambda_{i,k}^* \mathbf{a}_{k,j-1} + \mathbf{a}_{i+1,j-1}^{\dagger} \Lambda_{i+1,k}^* \mathbf{a}_{k,j-1} \right], \quad i \in \{1, 3\}, \quad (\text{B.27})$$

with index set $\mathcal{S}_i = \{i, i+1\}$ and matrix

$$\Lambda = \begin{pmatrix} 0 & e^{i4k_f} & 0 & 0 \\ e^{-i4k_f} & 0 & 0 & 0 \\ 0 & 0 & 0 & e^{-i4k_f} \\ 0 & 0 & e^{i4k_f} & 0 \end{pmatrix}. \quad (\text{B.28})$$

Since the nonzero entries of Λ couple terms similar to B.13, the Jordan-Wigner transform of the first term in the brackets becomes

$$\begin{aligned} \mathbf{a}_{i,j+1}^{\dagger} \Lambda_{i,k} \mathbf{a}_{k,j+1} &= (e^{i4k_f} \delta_{k,2}^{i,1} + e^{-i4k_f} \delta_{k,4}^{i,3}) \sigma_{i,j+1}^+ \Phi_{i,j+1}^{\dagger} \Phi_{k,j+1} \sigma_{k,j+1}^- \\ &= e^{i4k_f} \delta^{i,1} \sigma_{i,j+1}^+ \sigma_{2,j+1}^- + e^{-i4k_f} \delta^{i,3} \sigma_{i,j+1}^+ \sigma_{4,j+1}^- \end{aligned} \quad (\text{B.29})$$

The whole operator $\sum_i \mathcal{F}_{i,j}$ transforms to

$$\begin{aligned} &+ \rho_{1,j}\rho_{2,j} (e^{i4k_f} \sigma_{1,j+1}^+ \sigma_{2,j+1}^- + e^{-i4k_f} \sigma_{1,j+1}^- \sigma_{2,j+1}^+ \\ &\quad + e^{-i4k_f} \sigma_{1,j-1}^+ \sigma_{2,j-1}^- + e^{i4k_f} \sigma_{1,j-1}^- \sigma_{2,j-1}^+) + \\ &+ \rho_{3,j}\rho_{4,j} (e^{-i4k_f} \sigma_{3,j+1}^+ \sigma_{4,j+1}^- + e^{i4k_f} \sigma_{3,j+1}^- \sigma_{4,j+1}^+ \\ &\quad + e^{i4k_f} \sigma_{3,j-1}^+ \sigma_{4,j-1}^- + e^{-i4k_f} \sigma_{3,j-1}^- \sigma_{4,j-1}^+), \end{aligned} \quad (\text{B.30})$$

which leads to the interacting Hamiltonian at $\Omega = 0$

$$\begin{aligned}
\mathcal{H} = & \sum_{j=1}^L -T_{i,i} \left(\sigma_{i,j+1}^+ \left(\prod_{i' > i \in \mathcal{J}} \sigma_{i',j+1}^z \right) \left(\prod_{i' < i \in \mathcal{J}} \sigma_{i',j}^z \right) \sigma_{i,j}^- \right) + \text{h.c.} + \\
& -J \left(\sigma_{1,j}^+ \sigma_{2,j}^z \sigma_{3,j}^- + \sigma_{1,j}^- \sigma_{2,j}^z \sigma_{3,j}^+ + \sigma_{2,j}^+ \sigma_{3,j}^z \sigma_{4,j}^- + \sigma_{2,j}^- \sigma_{3,j}^z \sigma_{4,j}^+ \right) + \\
& + \tilde{\mu}_{i,i} \sigma_{i,j}^+ \sigma_{i,j}^- + \\
& U_{\Omega} \left(\rho_{1,j} \rho_{2,j} \left(e^{i4k_F} \sigma_{1,j+1}^+ \sigma_{2,j+1}^- + e^{-i4k_F} \sigma_{1,j+1}^- \sigma_{2,j+1}^+ \right) + \right. \\
& \left. \rho_{3,j} \rho_{4,j} \left(e^{-i4k_F} \sigma_{3,j+1}^+ \sigma_{4,j+1}^- + e^{i4k_F} \sigma_{3,j+1}^- \sigma_{4,j+1}^+ \right) + \right. \\
& \left. \rho_{1,j+1} \rho_{2,j+1} \left(e^{-i4k_F} \sigma_{1,j}^+ \sigma_{2,j}^- + e^{i4k_F} \sigma_{1,j}^- \sigma_{2,j}^+ \right) + \right. \\
& \left. \rho_{3,j+1} \rho_{4,j+1} \left(e^{i4k_F} \sigma_{3,j}^+ \sigma_{4,j}^- + e^{-i4k_F} \sigma_{3,j}^- \sigma_{4,j}^+ \right) \right) . \tag{B.31}
\end{aligned}$$

DENSITY ASSISTED INTER-CHAIN TUNNELING

Another promising interaction can be realized as

$$\rho_{\sigma,+}(r) \rho_{\sigma,-} \left(\mathbf{a}_{\sigma}^{\dagger}(r+1) \tau_x \otimes \mathbb{1} \mathbf{a}_{\sigma}(r+1) + \mathbf{a}_{\sigma}^{\dagger}(r-1) \tau_x \otimes \mathbb{1} \mathbf{a}_{\sigma}(r-1) \right) , \tag{B.32}$$

which we rewrite in our notation to

$$\begin{aligned}
\Gamma_{i,j} = & \rho_{i,j} \rho_{i+2,j} \sum_{k \in \mathcal{T}_i} \left(\mathbf{a}_{i,j+1}^{\dagger} (\tau_x \otimes \mathbb{1})_{i,k} \mathbf{a}_{k,j+1} + \mathbf{a}_{i+2,j+1}^{\dagger} (\tau_x \otimes \mathbb{1})_{i+2,k} \mathbf{a}_{k,j+1} \right. \\
& \left. + \mathbf{a}_{i,j-1}^{\dagger} (\tau_x \otimes \mathbb{1})_{i,k} \mathbf{a}_{i,j-1} + \mathbf{a}_{i+2,j-1}^{\dagger} (\tau_x \otimes \mathbb{1})_{i+2,k} \mathbf{a}_{i,j-1} \right) , i \in \{1, 2\} . \tag{B.33}
\end{aligned}$$

The sum over k runs over $\mathcal{T}_i = \{i, i+2\}$ since this corresponds to a summation over τ with states of equal spin value σ . The stated expression transforms in a similar way as [B.16](#) to

$$\begin{aligned}
\Gamma_{i,j} = & \rho_{i,j} \rho_{i+2,j} \left(\sigma_{i,j+1}^+ (-\sigma_{i+1,j+1}^z) \sigma_{i+2,j+1}^- + \sigma_{i+2,j+1}^+ (-\sigma_{i+1,j+1}^z) \sigma_{i,j+1}^- \right. \\
& \left. + \sigma_{i,j-1}^+ (-\sigma_{i+1,j-1}^z) \sigma_{i+2,j-1}^- + \sigma_{i+2,j-1}^+ (-\sigma_{i+1,j-1}^z) \sigma_{i,j-1}^- \right) , i \in \{1, 2\} , \tag{B.34}
\end{aligned}$$

and we can write the interacting Hamiltonian at $J = 0$ as

$$\begin{aligned}
\mathcal{H} = \sum_{j=1}^L & -T_{i,i} \left(\sigma_{i,j+1}^+ \left(\prod_{i' > i \in \mathcal{J}} \sigma_{i',j+1}^z \right) \left(\prod_{i' < i \in \mathcal{J}} \sigma_{i',j}^z \right) \sigma_{i,j}^- \right) + \text{h.c.} + \\
& \Omega \left(\sigma_{1,j}^+ \sigma_{2,j}^- + \sigma_{1,j}^- \sigma_{2,j}^+ + \sigma_{3,j}^+ \sigma_{4,j}^- + \sigma_{3,j}^- \sigma_{4,j}^+ \right) + \tilde{\mu}_{i,i} \sigma_{i,j}^+ \sigma_{i,j}^- + \\
& -U_J \left(\rho_{1,j} \rho_{3,j} \left(\sigma_{1,j+1}^+ \sigma_{2,j+1}^z \sigma_{3,j+1}^- + \text{h.c.} \right) \right. \\
& \quad + \rho_{2,j} \rho_{4,j} \left(\sigma_{2,j+1}^+ \sigma_{3,j+1}^z \sigma_{4,j+1}^- + \text{h.c.} \right) + \\
& \quad \rho_{1,j+1} \rho_{3,j+1} \left(\sigma_{1,j}^+ \sigma_{2,j}^z \sigma_{3,j}^- + \text{h.c.} \right) \\
& \quad \left. + \rho_{2,j+1} \rho_{4,j+1} \left(\sigma_{2,j}^+ \sigma_{3,j}^z \sigma_{4,j}^- + \text{h.c.} \right) \right). \tag{B.35}
\end{aligned}$$

It is possible to give exact solutions for a generic setup of the four-leg ladder up to $L = 4$ sites. In the computational basis, the complexity of this problem is the diagonalization of a sparse $2^{4L} = 65536$ matrix - this dimension is about the limit of LAPACK libraries which are the commonly used libraries for such processes. Although we could decompose the generic Hamiltonian of larger systems to its individual $U(1)$ -charge sectors, we do not see the need for it since we want to go to $L \approx 100$ - way above the limit for any exact diagonalization. We only use exact diagonalization to verify the correct implementation of the many different MPO we used in this thesis. Since the most costly next-to-nearest Hubbard interaction and the three-body density-assisted spin flip interaction considers twelve adjacent sites in the computational basis, sixteen virtual sites are more than enough to guarantee a correct implementation when we compare the simulation to results of exact diagonalization.

We conclude our local MPO of Eq. I.3 to have a compact form when merging four virtual sites to a single physical site of dimension $2^4 = 16$. This explicit realization is picturized in Fig. 40 and has an easy to grasp form because it reads very similar as the individual terms of the Hamiltonian. Nevertheless, implementing this representation kills the fast simulation runtime due to the huge local dimensionality.

There is a very elegant opportunity to keep MPS at the smallest possible local dimension $d = 2$. I.e. it is possible to implement a space-dependence for the local Hamiltonian, because the contractions are implemented site-by-site anyway. This allows for the freedom to choose operator representatives which depend on the sub-site position $i \in \mathcal{J}$ of the different species at the same physical position. For the four species ladder, we can find such an MPO with a mod_4 recursive construction, iterating over all enumerated virtual sites as Fig. 3 suggests. In analog, in the two-leg ladder this MPO has a mod_2 construction.

The following figures represent the MPO implementation of single-particle Hamiltonian (Fig. 40) and density-assisted interactions (Fig. 40) in the $d = 2^4 = 16$ computational basis.

Coefficient	MPO _L	MPO _R
1	$0_1 \begin{array}{c} \uparrow c \\ \square \\ \downarrow c \\ \rightarrow 0_1 \end{array} + \mathbb{1} \otimes \mathbb{1} \otimes \mathbb{1} \otimes \mathbb{1}$	$0_2 \begin{array}{c} \uparrow c \\ \square \\ \downarrow c \\ \rightarrow 0_2 \end{array} \mathbb{1} \otimes \mathbb{1} \otimes \mathbb{1} \otimes \mathbb{1}$
+texp(-iB/2)	$0_1 \begin{array}{c} \uparrow c+1 \\ \square \\ \downarrow c+1 \\ \rightarrow 0_1 \end{array} -\sigma^- \otimes \sigma^z \otimes \sigma^z \otimes \sigma^z$	$-1_1 \begin{array}{c} \uparrow c \\ \square \\ \downarrow c+1 \\ \rightarrow 0_2 \end{array} +\sigma^+ \otimes \mathbb{1} \otimes \mathbb{1} \otimes \mathbb{1}$
+texp(+iB/2)	$0_1 \begin{array}{c} \uparrow c+1 \\ \square \\ \downarrow c+1 \\ \rightarrow 0_1 \end{array} + \mathbb{1} \otimes \sigma^- \otimes \sigma^z \otimes \sigma^z$	$-1_2 \begin{array}{c} \uparrow c \\ \square \\ \downarrow c+1 \\ \rightarrow 0_2 \end{array} -\sigma^z \otimes \sigma^+ \otimes \mathbb{1} \otimes \mathbb{1}$
-texp(-iB/2)	$0_1 \begin{array}{c} \uparrow c+1 \\ \square \\ \downarrow c+1 \\ \rightarrow 0_1 \end{array} - \mathbb{1} \otimes \mathbb{1} \otimes \sigma^- \otimes \sigma^z$	$-1_3 \begin{array}{c} \uparrow c \\ \square \\ \downarrow c+1 \\ \rightarrow 0_2 \end{array} +\sigma^z \otimes \sigma^z \otimes \sigma^+ \otimes \mathbb{1}$
-texp(+iB/2)	$0_1 \begin{array}{c} \uparrow c+1 \\ \square \\ \downarrow c+1 \\ \rightarrow 0_1 \end{array} + \mathbb{1} \otimes \mathbb{1} \otimes \mathbb{1} \otimes \sigma^-$	$-1_4 \begin{array}{c} \uparrow c \\ \square \\ \downarrow c+1 \\ \rightarrow 0_2 \end{array} -\sigma^z \otimes \sigma^z \otimes \sigma^z \otimes \sigma^+$
+texp(+iB/2)	$0_1 \begin{array}{c} \uparrow c \\ \square \\ \downarrow c+1 \\ \rightarrow 0_1 \end{array} -\sigma^+ \otimes \sigma^z \otimes \sigma^z \otimes \sigma^z$	$1_1 \begin{array}{c} \uparrow c+1 \\ \square \\ \downarrow c \\ \rightarrow 0_2 \end{array} +\sigma^- \otimes \mathbb{1} \otimes \mathbb{1} \otimes \mathbb{1}$
+texp(-iB/2)	$0_1 \begin{array}{c} \uparrow c \\ \square \\ \downarrow c+1 \\ \rightarrow 0_1 \end{array} + \mathbb{1} \otimes \sigma^+ \otimes \sigma^z \otimes \sigma^z$	$1_2 \begin{array}{c} \uparrow c+1 \\ \square \\ \downarrow c \\ \rightarrow 0_2 \end{array} -\sigma^z \otimes \sigma^- \otimes \mathbb{1} \otimes \mathbb{1}$
-texp(+iB/2)	$0_1 \begin{array}{c} \uparrow c \\ \square \\ \downarrow c+1 \\ \rightarrow 0_1 \end{array} - \mathbb{1} \otimes \mathbb{1} \otimes \sigma^+ \otimes \sigma^z$	$1_3 \begin{array}{c} \uparrow c+1 \\ \square \\ \downarrow c \\ \rightarrow 0_2 \end{array} +\sigma^z \otimes \sigma^z \otimes \sigma^- \otimes \mathbb{1}$
-texp(-iB/2)	$0_1 \begin{array}{c} \uparrow c \\ \square \\ \downarrow c+1 \\ \rightarrow 0_1 \end{array} + \mathbb{1} \otimes \mathbb{1} \otimes \mathbb{1} \otimes \sigma^+$	$1_4 \begin{array}{c} \uparrow c+1 \\ \square \\ \downarrow c \\ \rightarrow 0_2 \end{array} -\sigma^z \otimes \sigma^z \otimes \sigma^z \otimes \sigma^-$
$\mu_0 + \mu$	$0_1 \begin{array}{c} \uparrow c \\ \square \\ \downarrow c \\ \rightarrow 0_2 \end{array} + \begin{array}{c} \sigma^+ \sigma^- \otimes \mathbb{1} \otimes \mathbb{1} \otimes \mathbb{1} \\ \mathbb{1} \otimes \sigma^+ \sigma^- \otimes \mathbb{1} \otimes \mathbb{1} \end{array}$	
$\mu_0 - \mu$	$0_1 \begin{array}{c} \uparrow c \\ \square \\ \downarrow c \\ \rightarrow 0_2 \end{array} + \begin{array}{c} \mathbb{1} \otimes \mathbb{1} \otimes \sigma^+ \sigma^- \otimes \mathbb{1} \\ \mathbb{1} \otimes \mathbb{1} \otimes \mathbb{1} \otimes \sigma^+ \sigma^- \end{array}$	
Ω	$0_1 \begin{array}{c} \uparrow c \\ \square \\ \downarrow c \\ \rightarrow 0_2 \end{array} + \begin{array}{c} \sigma^+ \otimes \sigma^- \otimes \mathbb{1} \otimes \mathbb{1} + \mathbb{1} \otimes \mathbb{1} \otimes \sigma^+ \otimes \sigma^- \\ \sigma^- \otimes \sigma^+ \otimes \mathbb{1} \otimes \mathbb{1} + \mathbb{1} \otimes \mathbb{1} \otimes \sigma^- \otimes \sigma^+ \end{array}$	
J	$0_1 \begin{array}{c} \uparrow c \\ \square \\ \downarrow c \\ \rightarrow 0_2 \end{array} - \begin{array}{c} \sigma^+ \otimes \sigma^z \otimes \sigma^- \otimes \mathbb{1} - \mathbb{1} \otimes \sigma^+ \otimes \sigma^z \otimes \sigma^- \\ \sigma^- \otimes \sigma^z \otimes \sigma^+ \otimes \mathbb{1} - \mathbb{1} \otimes \sigma^- \otimes \sigma^z \otimes \sigma^+ \end{array}$	

Figure 39: Jordan-Wigner transformed, local Hamiltonian (Eq. B.18) of local dimension 2^4 . The first column contains coefficients that have to be multiplied exactly once, either to the opening channels in column two or their closing channels in column three. Despite its beauty in terms of readability, a realization of this MPO in a DMRG simulation has a rather unfortunate runtime in comparison to its reformulation to local dimension two or four. For the reduction of local dimension, the MPO has to be site-dependent.

Coefficient	MPO _L	MPO _R		
$U_{\Omega} \exp(+i4k_F)$		$\sigma^+ \sigma^- \otimes \sigma^+ \sigma^- \otimes 1 \otimes 1$		$\sigma^+ \otimes \sigma^- \otimes 1 \otimes 1$
$U_{\Omega} \exp(-i4k_F)$		$1 \otimes 1 \otimes \sigma^+ \sigma^- \otimes \sigma^+ \sigma^-$		$1 \otimes 1 \otimes \sigma^+ \otimes \sigma^-$
$U_{\Omega} \exp(-i4k_F)$		$\sigma^+ \otimes \sigma^- \otimes 1 \otimes 1$		$\sigma^+ \sigma^- \otimes \sigma^+ \sigma^- \otimes 1 \otimes 1$
$U_{\Omega} \exp(+i4k_F)$		$1 \otimes 1 \otimes \sigma^+ \otimes \sigma^-$		$1 \otimes 1 \otimes \sigma^+ \sigma^- \otimes \sigma^+ \sigma^-$
$U_{\Omega} \exp(-i4k_F)$				$\sigma^- \otimes \sigma^+ \otimes 1 \otimes 1$
$U_{\Omega} \exp(+i4k_F)$				$1 \otimes 1 \otimes \sigma^- \otimes \sigma^+$
$U_{\Omega} \exp(+i4k_F)$		$\sigma^- \otimes \sigma^+ \otimes 1 \otimes 1$		
$U_{\Omega} \exp(-i4k_F)$		$1 \otimes 1 \otimes \sigma^- \otimes \sigma^+$		
U_J		$\sigma^+ \sigma^- \otimes 1 \otimes \sigma^+ \sigma^- \otimes 1$		$-\sigma^+ \otimes \sigma^z \otimes \sigma^- \otimes 1$
U_J		$1 \otimes \sigma^+ \sigma^- \otimes 1 \otimes \sigma^+ \sigma^-$		$-1 \otimes \sigma^+ \otimes \sigma^z \otimes \sigma^-$
U_J		$-\sigma^+ \otimes \sigma^z \otimes \sigma^- \otimes 1$		$\sigma^+ \sigma^- \otimes 1 \otimes \sigma^+ \sigma^- \otimes 1$
U_J		$-1 \otimes \sigma^+ \otimes \sigma^z \otimes \sigma^-$		$1 \otimes \sigma^+ \sigma^- \otimes 1 \otimes \sigma^+ \sigma^-$
				$-\sigma^- \otimes \sigma^z \otimes \sigma^+ \otimes 1$
				$-1 \otimes \sigma^- \otimes \sigma^z \otimes \sigma^+$
U_J		$-\sigma^- \otimes \sigma^z \otimes \sigma^+ \otimes 1$		
U_J		$-1 \otimes \sigma^- \otimes \sigma^z \otimes \sigma^+$		

Figure 40: Jordan-Wigner transformed density-dependent interactions of Eq. III.11 (top) and Eq. III.13 (bottom).

B.3 TRANSFORMATION TO MAJORANA-FERMIONS

We hope to achieve more insights into the model by mapping it to Majorana-fermions

$$\hat{a} = \frac{1}{2} (\hat{m}^1 - i\hat{m}^2) \quad (\text{B.36})$$

$$\hat{a}^\dagger = \frac{1}{2} (\hat{m}^1 + i\hat{m}^2) \quad (\text{B.37})$$

which results in

$$H = \hat{a}_i^\dagger (d\delta_{i,j} + T\delta_{i+1,j} + T^*\delta_{i,j+1}) \hat{a}_j \quad (\text{B.38})$$

$$= \frac{1}{4} (\hat{m}_i^1 + i\hat{m}_i^2) (d\delta_{i,j} + T\delta_{i+1,j} + T^*\delta_{i,j+1}) (\hat{m}_j^1 - i\hat{m}_j^2) . \quad (\text{B.39})$$

The first term of this expression reads

$$\begin{aligned} (\hat{m}_i^1 + i\hat{m}_i^2) d\delta_{ij} (\hat{m}_j^1 - i\hat{m}_j^2) &= \hat{m}_i^1 d\hat{m}_i^1 + \hat{m}_i^2 d\hat{m}_i^2 \\ &\quad + i (\hat{m}_i^2 d\hat{m}_i^1 - \hat{m}_i^1 d\hat{m}_i^2) . \end{aligned} \quad (\text{B.40})$$

d is a real, symmetric and non-diagonal 4×4 matrix

$$d = \begin{pmatrix} \mu_0 + \mu & \Omega & J & 0 \\ \Omega & \mu_0 + \mu & 0 & J \\ J & 0 & \mu_0 - \mu & \Omega \\ 0 & J & \Omega & \mu_0 - \mu \end{pmatrix} \quad (\text{B.41})$$

and the 4-component Majorana-Fermions fulfill in addition to the anticommutation relations

$$\{m_{i,j}^\alpha, m_{k,l}^\beta\} = 2\delta_{ik}\delta_{jl}\delta_{\alpha\beta} \quad (\hat{m}^\alpha)^2 = 1 \quad (\text{B.42})$$

i.e. they are hermitian creation operators and in this sense they are their own antiparticles. because d is symmetric and real, the scalar expression $\hat{m}_i^\alpha d\hat{m}_i^\alpha$ becomes

$$\begin{aligned} \hat{m}^\alpha d\hat{m}^\beta &= + (\mu_0 + \mu) (m_{1,i}^\alpha m_{1,i}^\beta + m_{2,i}^\alpha m_{2,i}^\beta) \\ &\quad + (\mu_0 - \mu) (m_{3,i}^\alpha m_{3,i}^\beta + m_{4,i}^\alpha m_{4,i}^\beta) \\ &\quad + J (m_{1,i}^\alpha m_{3,i}^\beta + m_{3,i}^\alpha m_{1,i}^\beta + m_{2,i}^\alpha m_{4,i}^\beta + m_{4,i}^\alpha m_{2,i}^\beta) \\ &\quad + \Omega (m_{1,i}^\alpha m_{2,i}^\beta + m_{2,i}^\alpha m_{1,i}^\beta + m_{3,i}^\alpha m_{4,i}^\beta + m_{4,i}^\alpha m_{3,i}^\beta) . \end{aligned} \quad (\text{B.43})$$

In the cases $\alpha = \beta$, the only resulting term is

$$\sum_{\alpha=1}^2 \hat{m}_i^\alpha d\hat{m}_i^\alpha = 8\mu_0 . \quad (\text{B.44})$$

This simplifies the expression from before to

$$(\widehat{\mathbf{m}}_i^1 + i\widehat{\mathbf{m}}_i^2) d\delta_{ij} (\widehat{\mathbf{m}}_j^1 - i\widehat{\mathbf{m}}_j^2) = i \begin{pmatrix} \widehat{\mathbf{m}}^1 & \widehat{\mathbf{m}}^2 \end{pmatrix} \begin{pmatrix} 0 & D \\ -D & 0 \end{pmatrix} \begin{pmatrix} \widehat{\mathbf{m}}^1 \\ \widehat{\mathbf{m}}^2 \end{pmatrix} + 8L\mu_0 \quad (\text{B.45})$$

with a $4L \times 4L$ matrix D with diagonal elements d . Now to the simplification of the second and third term. $T^* = T^\dagger$, because T is strictly diagonal.

$$\begin{aligned} (\widehat{\mathbf{m}}_i^1 + i\widehat{\mathbf{m}}_i^2) (T\delta_{i+1,j} + T^*\delta_{i,j+1}) (\widehat{\mathbf{m}}_j^1 - i\widehat{\mathbf{m}}_j^2) &= (\widehat{\mathbf{m}}_i^\alpha T\widehat{\mathbf{m}}_{i+1}^\alpha + \widehat{\mathbf{m}}_{i+1}^\alpha T^*\widehat{\mathbf{m}}_i^\alpha \\ &\quad + i(\widehat{\mathbf{m}}_i^2 T\widehat{\mathbf{m}}_{i+1}^1 + \widehat{\mathbf{m}}_{i+1}^2 T^*\widehat{\mathbf{m}}_i^1 - \widehat{\mathbf{m}}_i^1 T\widehat{\mathbf{m}}_{i+1}^2 - \widehat{\mathbf{m}}_{i+1}^1 T^*\widehat{\mathbf{m}}_i^2)) \\ &= (\widehat{\mathbf{m}}_i^\alpha T\widehat{\mathbf{m}}_{i+1}^\alpha + \text{h.c.}) + i(\widehat{\mathbf{m}}_i^2 T\widehat{\mathbf{m}}_{i+1}^1 + \widehat{\mathbf{m}}_{i+1}^2 T^*\widehat{\mathbf{m}}_i^1 - \text{h.c.}) \end{aligned} \quad (\text{B.46})$$

There appear non-flavor mixing terms

$$\begin{aligned} \widehat{\mathbf{m}}_i^\alpha T\widehat{\mathbf{m}}_{i+1}^\alpha + \text{h.c.} &= t\tau_z \exp\left(i\frac{B}{2}\sigma_z\right) \widehat{\mathbf{m}}_i^\alpha \widehat{\mathbf{m}}_{i+1}^\alpha \\ &\quad + t\tau_z \exp\left(-i\frac{B}{2}\sigma_z\right) \widehat{\mathbf{m}}_{i+1}^\alpha \widehat{\mathbf{m}}_i^\alpha \\ &= t\tau_z \widehat{\mathbf{m}}_i^\alpha \widehat{\mathbf{m}}_{i+1}^\alpha \left(\exp\left(i\frac{B}{2}\sigma_z\right) - \exp\left(-i\frac{B}{2}\sigma_z\right)\right) \\ &= 2it\tau_z \sin(B/2\sigma_z) \widehat{\mathbf{m}}_i^\alpha \widehat{\mathbf{m}}_{i+1}^\alpha \\ &= 2it\tau_z \sigma_z \sin(B/2) \widehat{\mathbf{m}}_i^\alpha \widehat{\mathbf{m}}_{i+1}^\alpha = it\tau_z \sigma_z \sin(B/2) (\widehat{\mathbf{m}}_i^\alpha \widehat{\mathbf{m}}_{i+1}^\alpha - \widehat{\mathbf{m}}_{i+1}^\alpha \widehat{\mathbf{m}}_i^\alpha) \end{aligned} \quad (\text{B.47})$$

and flavor-mixing $\alpha \neq \beta$ terms

$$\begin{aligned} \widehat{\mathbf{m}}_i^\alpha T\widehat{\mathbf{m}}_{i+1}^\beta - \text{h.c.} &= t\tau_z \exp\left(i\frac{B}{2}\sigma_z\right) \widehat{\mathbf{m}}_i^\alpha \widehat{\mathbf{m}}_{i+1}^\beta \\ &\quad - t\tau_z \exp\left(-i\frac{B}{2}\sigma_z\right) \widehat{\mathbf{m}}_{i+1}^\beta \widehat{\mathbf{m}}_i^\alpha \\ &= t\tau_z \widehat{\mathbf{m}}_i^\alpha \widehat{\mathbf{m}}_{i+1}^\beta \left(\exp\left(i\frac{B}{2}\sigma_z\right) + \exp\left(-i\frac{B}{2}\sigma_z\right)\right) \\ &= 2t\tau_z \cos(B/2) \widehat{\mathbf{m}}_i^\alpha \widehat{\mathbf{m}}_{i+1}^\beta = t\tau_z \cos(B/2) (\widehat{\mathbf{m}}_i^\alpha \widehat{\mathbf{m}}_{i+1}^\beta - \widehat{\mathbf{m}}_{i+1}^\beta \widehat{\mathbf{m}}_i^\alpha) . \end{aligned} \quad (\text{B.48})$$

When we put everything together and introduce coupling matrices Γ_i as

$$\Gamma_{i,j}^1 := \tau_z \otimes \sigma_z (\delta_{j,i+1} - \delta_{i,j+1}) \quad (\text{B.49})$$

$$\Gamma_{i,j}^2 := \tau_z \otimes \mathbb{1} (\delta_{j,i+1} + \delta_{i,j+1}) \quad (\text{B.50})$$

$$\Gamma_{i,j}^3 := d\delta_{i,j} , \quad (\text{B.51})$$

we end up writing the Hamiltonian in a more compact way

$$\begin{aligned} H_{\text{Majorana}} &= \frac{i}{4} \begin{pmatrix} \widehat{\mathbf{m}}^1 & \widehat{\mathbf{m}}^2 \end{pmatrix} \left(t \sin(B/2) \begin{pmatrix} \Gamma^1 & 0 \\ 0 & \Gamma^1 \end{pmatrix} \right. \\ &\quad \left. - t \cos(B/2) \begin{pmatrix} 0 & \Gamma^2 \\ -\Gamma^2 & 0 \end{pmatrix} + \begin{pmatrix} 0 & \Gamma^3 \\ -\Gamma^3 & 0 \end{pmatrix} \right) \begin{pmatrix} \widehat{\mathbf{m}}^1 \\ \widehat{\mathbf{m}}^2 \end{pmatrix} . \end{aligned} \quad (\text{B.52})$$

Unfortunately, this transformation does not yield any simplification.

C

OPTICAL LATTICES

Optical lattices provide a convenient platform for quantum simulations of many body systems that can be described efficiently using tight-binding approximations on lattice structures [5]. For this thesis, a four-leg ladder system yields the noninteracting Hamiltonian that is of particular interest in Ch. I. Due to the gauge field that results in the magnetic field along each plaquette, a successful realization requires the framework of synthetic gauge potentials [44]. The laboratory framework for optical lattices utilizes confinement of cold atoms in potentials created with laser light to reduce the dimensionality from 3D to effective 2D or 1D systems. To understand any experimental setup, we first need to understand how trapping neutral atoms becomes possible with optical dipole traps using far-detuned light. We review briefly the origin and consequences of the dipole force, which we explicitly use therein. After this recap, we will introduce two realizable optical lattices, and use their combination to motivate the Hamiltonian that we will use as a starting point for the second chapter of this thesis.

C.1 OPTICAL POTENTIALS

We want to understand the basic concept of dipole potentials by modeling atoms as simple oscillators subject to the radiation field. We assume a field described by the vector potential

$$\vec{A}(\vec{r}, t) = \vec{\epsilon} \cdot A_0 e^{+i(\vec{k}\vec{r} - \omega t)}. \quad (\text{C.1})$$

and subject to the Coulomb gauge condition $\vec{\nabla} \cdot \vec{A} = 0$. In this notation, we use a polarization unit vector $\vec{\epsilon}$ and describe a wave oscillating in time at angular frequency ω , propagating in the vacuum along direction \vec{k} . Whenever an atom is placed inside such a laser field, its dipole moment \vec{p} reacts to the oscillation

$$\vec{p}(\vec{r}, t) = \vec{\epsilon} \cdot p_0(\vec{r}) e^{-i\omega t}. \quad (\text{C.2})$$

The amplitude p_0 has an explicit relation to the amplitude of the electric field

$$\vec{E}(\vec{r}, t) = -\partial_t \vec{A}(\vec{r}, t) = \vec{e} \cdot E_0(\vec{r}) e^{-i\omega t} \quad p_0(\vec{r}) = \alpha(\omega) E_0(\vec{r}). \quad (\text{C.3})$$

The scalar value $\alpha(\omega) \in \mathbb{C}$ is called polarizability and depends on the driving frequency ω of the vector potential \vec{A} . The induction of a dipole moment results in an interaction potential

$$U_{\text{dip}} = -\frac{1}{2} \left\langle \vec{p}(\vec{r}, t) \cdot \vec{E}(\vec{r}, t) \right\rangle_t = -\frac{\text{Re}(\alpha(\omega)) \cdot I(\vec{r})}{2\epsilon_0 c} \propto \text{Re}(\alpha(\omega)) I(\vec{r}), \quad (\text{C.4})$$

of field intensity $I(\vec{r}) = 2\epsilon_0 c |E_0(\vec{r})|^2$. This immediately implies that we may create artificial effective potentials by varying the space-dependent light-intensity of our setup through superposition of several laser-fields. To give an example, we consider the composition of three different laser beams $\vec{E}_1, \vec{E}_2, \vec{E}_3$ that span a 2D plane with $2\pi/3$ -configuration as shown in Fig. 41. If the polarization is in the $x-y$ plane as the alignment of the laser beams, it is possible to engineer a hexagonal lattice. The result is a perfect triangular lattice, if the polarization choice is along z and the three laser beams span the $x-y$ plane. With two additional lasers beams along the z -axis, further confinement is possible to achieve an effective 3D optical potential which confines neutral atoms at certain lattice points in \mathbb{R}^3 . Due to the use of laser light, a vast control of the distance between potential minima and their depth is possible, which may be used to restrict the atom movements along effective 2D and even 1D structures.

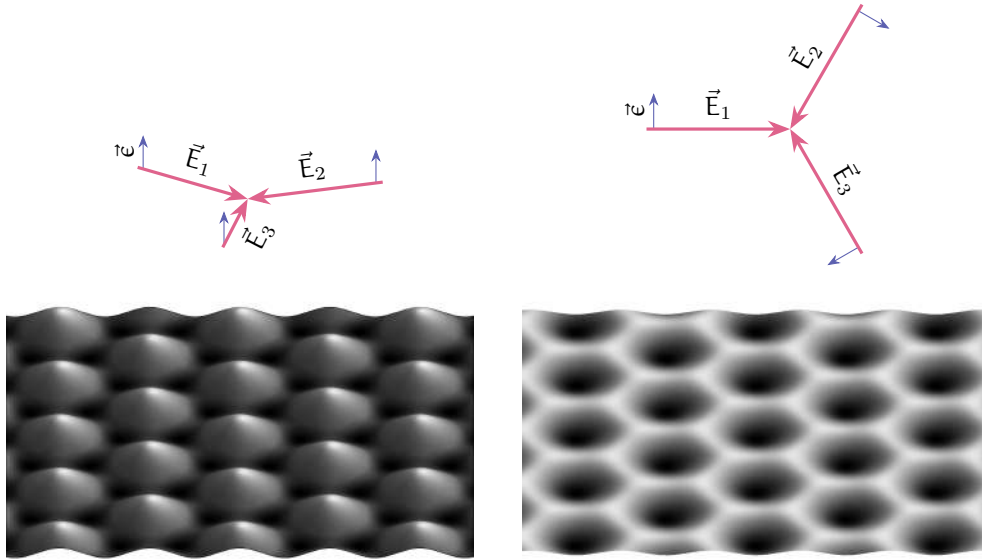


Figure 41: Hexagonal and triangular optical potentials with two different polarization choices \vec{e} for identical laser beam configuration.

For simplicity, we henceforth consider atoms forming a two-level systems of ground $|g\rangle$ and excited state $|e\rangle$ with frequency difference ω_0 . For large detuned optical lattices (meaning the laser's frequency is not in the vicinity of the atomic excitation frequency $\omega \gg \omega_0$ or $\omega \ll \omega_0$), the resulting optical lattice potential is approximately the same for all atomic sublevels in the ground-state manifold

of the atom. However when working with near-resonant red $\omega < \omega_0$ or blue $\omega > \omega_0$ detuned light, it is possible to make explicit use of the dependence on $\alpha(\omega)$ to engineer lattices that expose different magnetic sublevels to different grid positions. Such spin-dependent potentials offer to tune interactions between two atoms in different spin-states. I.e. shifting spin-dependent lattices relative to each other, the overlap of the atoms wave functions can be manipulated from zero to a maximum value which addresses directly the inter-species interaction strength [45]. In the next section, we will briefly recapitulate the physics and effects of such a setup.

C.2 ARTIFICIAL GAUGE FIELDS AND STATE DEPENDENT SUPERLATTICES

For tight-binding approximations of charged particles, it has been shown [46] that the effect of a nonzero vector potential $\vec{A} = -By\vec{e}_x$ contributes to the Hamiltonian as complex Peierl's phase with factor $2\pi\alpha n$ and $\alpha = eBd^2/h$ being the flux per unit cell in units of h/e .

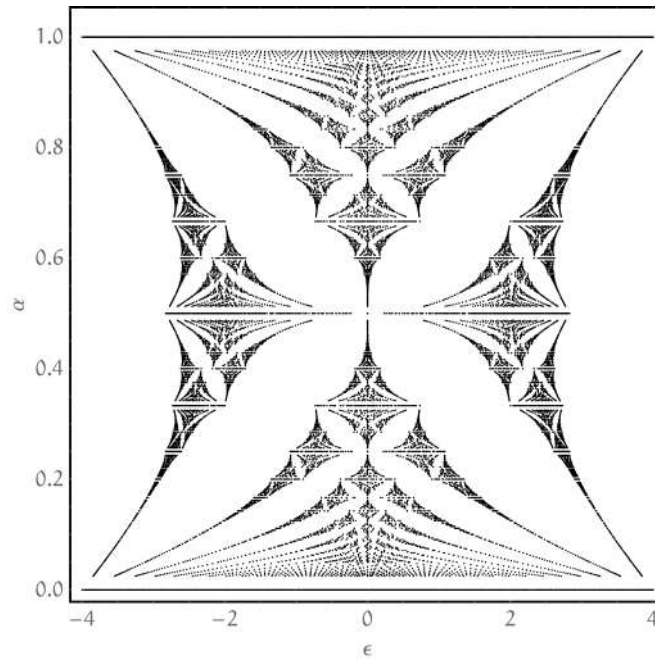


Figure 42: The famous Hofstadter butterfly [47] is a figure of the energy-flux spectrum of the Harper Hamiltonian. Since it is quadratic in fermionic annihilation and creation operators, we solve it exactly. Each data point at $(\epsilon, \alpha = p/q)$ is an exact solution of Eq. C.5 for single unit cell with periodic boundary conditions. For this picture, the eigenvalues of the Hamiltonian $\epsilon(k)$ have been rescaled to $\epsilon := \epsilon(k)/J$ where $J_x = J_y$.

A necessary component to realize such a setup in the lab relies on in being able penetrate the system with a tunable magnetic flux. However, due to the neutral nature of atoms, they do not react upon being penetrated by a physical magnetic

field. Fortunately, people came up with the concept of synthetic gauge potentials in the context of Raman-assisted tunneling, providing lattice structures with *neutral atoms* and mimicking tight-binding approximations of *charged particles*, being penetrated by nonzero magnetic field [48]. Such a setup can be described by the Harper Hamiltonian

$$\hat{H}_{\text{Harper}} = - \sum_{m,n,\pm} e^{\pm i 2\pi \alpha n} J_x \hat{c}_{m\pm 1,n}^\dagger \hat{c}_{m,n} + J_y \hat{c}_{m,n\pm 1}^\dagger \hat{c}_{m,n} + \text{H.c.}, \quad (\text{C.5})$$

which was introduced assuming $J_x = J_y =: J$ in 1955 [47]. The fermionic operators $\hat{c}_{m,n}^\dagger$ are single-species fermionic operators which create a particle at grid position $(x, y) = (m\alpha, n\alpha)$. This grid has a constant lattice spacing α and J denotes the energy of nearest neighbor tunneling without magnetic field. When we allow for arbitrary values of $\alpha \in (0, 1)$, this Hamiltonian classifies to a more generalized tight binding model. The physics of the energy-spectrum is not of particular interest for this thesis, but we want to show it explicitly as one of many examples of the beauty of models realizable on optical lattices.

Other approaches to realize gauge fields do not rely on the internal degrees of freedom but instead apply off-resonant time-periodic shakings in well-confined atomic lattices [49]. Such shakings yield then a complex Peierl's phase combined with other on-site interactions.

In 2003, Jaksch and Zoller proposed an experimentally feasible setup to imprint the Peierl's phase factor $e^{\pm i 2\pi \alpha}$ with help of laser-induced hopping between adjacent sites [50] that dramatically increases the physically reachable values of α .

Works of Gerbier et al. showed the possibility to construct an optical superlattice to generate the gauge potential yielding Eq. C.5. This is possible using effective two-level atoms with so-called (*anti*-)magic wavelengths, meaning the polarizability of ground and excited state is exactly the same (opposite) at certain frequencies.

The use of a spin-independent superlattice along the y -direction allows to freeze the movement along y and enables the possibility to separate atoms as pleased. An additional superlattice along the x -direction is driven at appropriate anti-magic wavelengths to yield an effective spin-dependent energy offset between two lattice sites.

This concepts, combined in a single model, provide all terms that are needed for the non-interacting Hamiltonian in Eq. I.3. Here, we do not follow the steps necessary to engineer such a setup, but instead refer to the detailed proposal for the experimental realization in [13].

BIBLIOGRAPHY

- [1] Andreas P. Schnyder, Shinsei Ryu, Akira Furusaki, and Andreas W. W. Ludwig. **Classification of topological insulators and superconductors in three spatial dimensions**. *Phys. Rev. B*, 78:195125, Nov 2008.
- [2] Paul Fendley. **Parafermionic edge zero modes in Z_n -invariant spin chains**. *Journal of Statistical Mechanics: Theory and Experiment*, 2012(11):P11020, 2012.
- [3] Jason Alicea and Paul Fendley. Topological phases with parafermions: Theory and blueprints. *Annual Review of Condensed Matter Physics*, 7(1):119–139, 2016.
- [4] C. L. Kane, Ranjan Mukhopadhyay, and T. C. Lubensky. **Fractional Quantum Hall Effect in an Array of Quantum Wires**. *Phys. Rev. Lett.*, 88:036401, Jan 2002.
- [5] Immanuel Bloch, Jean Dalibard, and Wilhelm Zwerger. **Many-body physics with ultracold gases**. *Rev. Mod. Phys.*, 80:885–964, Jul 2008.
- [6] Roger S. K. Mong, David J. Clarke, Jason Alicea, Netanel H. Lindner, Paul Fendley, Chetan Nayak, Yuval Oreg, Ady Stern, Erez Berg, Kirill Shtengel, and Matthew P. A. Fisher. **Universal Topological Quantum Computation from a Superconductor-Abelian Quantum Hall Heterostructure**. *Phys. Rev. X*, 4:011036, Mar 2014.
- [7] Román Orús. **A practical introduction to tensor networks: Matrix product states and projected entangled pair states**. *Annals of Physics*, 349:117 – 158, 2014.
- [8] J. Eisert, M. Cramer, and M. B. Plenio. **colloquium : area laws for the entanglement entropy**. *Rev. Mod. Phys.*, 82:277–306, Feb 2010.
- [9] Ralf Bulla, Theo A. Costi, and Thomas Pruschke. **Numerical renormalization group method for quantum impurity systems**. *Rev. Mod. Phys.*, 80:395–450, Apr 2008.
- [10] J Ignacio Cirac and Frank Verstraete. **Renormalization and tensor product states in spin chains and lattices**. *Journal of Physics A: Mathematical and Theoretical*, 42(50):504004, 2009.
- [11] Ulrich Schollwöck. **The density-matrix renormalization group in the age of matrix product states**. *Annals of Physics*, 326(1):96 – 192, 2011. January 2011 Special Issue.

- [12] Eyal Cornfeld and Eran Sela. **Chiral currents in one-dimensional fractional quantum Hall states**. *Phys. Rev. B*, 92:115446, Sep 2015.
- [13] Leonardo Mazza, Monika Aidelsburger, Hong-Hao Tu, Nathan Goldman, and Michele Burrello. **Methods for detecting charge fractionalization and winding numbers in an interacting fermionic ladder**. *New Journal of Physics*, 17(10):105001, 2015.
- [14] Sukhwinder Singh, Robert N. C. Pfeifer, and Guifre Vidal. **Tensor network states and algorithms in the presence of a global U(1) symmetry**. *Phys. Rev. B*, 83:115125, Mar 2011.
- [15] A. Haller. *Matrix Product States - A Variational Approach to Strongly Correlated Systems*. Bachelor thesis. 2014.
- [16] Sumanta Tewari and Jay D. Sau. **Topological Invariants for Spin-Orbit Coupled Superconductor Nanowires**. *Phys. Rev. Lett.*, 109:150408, Oct 2012.
- [17] Dario Hügél and Belén Paredes. **Chiral ladders and the edges of quantum Hall insulators**. *Phys. Rev. A*, 89:023619, Feb 2014.
- [18] S.-A. Cheong and C. L. Henley. **Many-Body Density Matrices for Free Fermions**. *eprint arXiv:cond-mat/0206196*, June 2002.
- [19] Luca Taddia. *Entanglement Entropies in One-Dimensional Systems*. PhD thesis, Università degli Studi di Bologna, 2013.
- [20] Hannes Pichler, Lars Bonnes, Andrew J Daley, Andreas M Läuchli, and Peter Zoller. **Thermal versus entanglement entropy: a measurement protocol for fermionic atoms with a quantum gas microscope**. *New Journal of Physics*, 15(6):063003, 2013.
- [21] Pasquale Calabrese and John Cardy. **Entanglement entropy and quantum field theory**. *Journal of Statistical Mechanics: Theory and Experiment*, 2004(06):P06002, 2004.
- [22] Pasquale Calabrese and Fabian H L Essler. **Universal corrections to scaling for block entanglement in spin-1/2 XX chains**. *Journal of Statistical Mechanics: Theory and Experiment*, 2010(08):P08029, 2010.
- [23] Steven R. White. **Density matrix formulation for quantum renormalization groups**. *Phys. Rev. Lett.*, 69:2863–2866, Nov 1992.
- [24] G. Vidal, J. I. Latorre, E. Rico, and A. Kitaev. **Entanglement in Quantum Critical Phenomena**. *Phys. Rev. Lett.*, 90:227902, Jun 2003.
- [25] P. Silvi. *Tensor Networks: a quantum-information perspective on numerical renormalization groups*. PhD thesis, Scuola Internazionale Superiore di Studi Avanzati, SISSA, 2012.
- [26] J. Friedel. **XIV. The distribution of electrons round impurities in monovalent metals**. *The London, Edinburgh, and Dublin Philosophical Magazine and Journal of Science*, 43(337):153–189, 1952.

- [27] A. Kitaev and C. Laumann. **Topological phases and quantum computation**. *ArXiv e-prints*, April 2009.
- [28] J. Hubbard. Electron correlations in narrow energy bands. *Proceedings of the Royal Society of London A: Mathematical, Physical and Engineering Sciences*, 276(1365):238–257, 1963.
- [29] M. Born and R. Oppenheimer. **Zur Quantentheorie der Molekeln**. *Annalen der Physik*, 389(20):457–484, 1927.
- [30] L. D. Landau, E. M. Lifshitz, J. B. Sykes, J. S. Bell, and M. E. Rose. **Quantum Mechanics, Non-Relativistic Theory**. *Physics Today*, 11:56, 1958.
- [31] Jeffrey C. Y. Teo and C. L. Kane. **From Luttinger liquid to non-Abelian quantum Hall states**. *Phys. Rev. B*, 89:085101, Feb 2014.
- [32] Eran Sela, Matthias Punk, and Markus Garst. **Dislocation-mediated melting of one-dimensional Rydberg crystals**. *Phys. Rev. B*, 84:085434, Aug 2011.
- [33] Jelena Klinovaja and Daniel Loss. **Parafermions in an Interacting Nanowire Bundle**. *Phys. Rev. Lett.*, 112:246403, Jun 2014.
- [34] Yuval Oreg, Eran Sela, and Ady Stern. **Fractional helical liquids in quantum wires**. *Phys. Rev. B*, 89:115402, Mar 2014.
- [35] Jelena Klinovaja and Daniel Loss. **Time-reversal invariant parafermions in interacting Rashba nanowires**. *Phys. Rev. B*, 90:045118, Jul 2014.
- [36] Simone Barbarino, Luca Taddia, Davide Rossini, Leonardo Mazza, and Rosario Fazio. **Synthetic gauge fields in synthetic dimensions: interactions and chiral edge modes**. *New Journal of Physics*, 18(3):035010, 2016.
- [37] Jan von Delft and Herbert Schoeller. **Bosonization for beginners ,Ä& refermionization for experts**. *Annalen der Physik*, 7(4):225–305, 1998.
- [38] M. P. A. Fisher and L. I. Glazman. **Transport in a one-dimensional Luttinger liquid**. *eprint arXiv:cond-mat/9610037*, October 1996.
- [39] M A Cazalilla. **Bosonizing one-dimensional cold atomic gases**. *Journal of Physics B: Atomic, Molecular and Optical Physics*, 37(7):S1, 2004.
- [40] Daniel C. Mattis and Elliott H. Lieb. **Exact Solution of a Many,Ä& Fermion System and Its Associated Boson Field**. *Journal of Mathematical Physics*, 6(2):304–312, 1965.
- [41] F D M Haldane. **'Luttinger liquid theory' of one-dimensional quantum fluids. I. Properties of the Luttinger model and their extension to the general 1D interacting spinless Fermi gas**. *Journal of Physics C: Solid State Physics*, 14(19):2585, 1981.
- [42] T. Giamarchi. **Quantum Physics in One Dimension**. International Series of Monographs on Physics. Clarendon Press, 2003.

- [43] F. D. M. Haldane. **Effective Harmonic-Fluid Approach to Low-Energy Properties of One-Dimensional Quantum Fluids.** *Phys. Rev. Lett.*, 47:1840–1843, Dec 1981.
- [44] N. Goldman and J. Dalibard. **Periodically Driven Quantum Systems: Effective Hamiltonians and Engineered Gauge Fields.** *Phys. Rev. X*, 4:031027, Aug 2014.
- [45] Immanuel Bloch, Jean Dalibard, and Wilhelm Zwerger. **Many-body physics with ultracold gases.** *Rev. Mod. Phys.*, 80:885–964, Jul 2008.
- [46] R Peierls. On the theory of diamagnetism of conduction electrons. *Physics Today*, 80:763, 791, 1933.
- [47] **Single Band Motion of Conduction Electrons in a Uniform Magnetic Field.** *Proceedings of the Physical Society. Section A*, 68(10):874, 1955.
- [48] Hirokazu Miyake, Georgios A. Siviloglou, Colin J. Kennedy, William Cody Burton, and Wolfgang Ketterle. **Realizing the Harper Hamiltonian with Laser-Assisted Tunneling in Optical Lattices.** *Phys. Rev. Lett.*, 111:185302, Oct 2013.
- [49] J. Struck, C. Ölschläger, M. Weinberg, P. Hauke, J. Simonet, A. Eckardt, M. Lewenstein, K. Sengstock, and P. Windpassinger. **Tunable Gauge Potential for Neutral and Spinless Particles in Driven Optical Lattices.** *Phys. Rev. Lett.*, 108:225304, May 2012.
- [50] D Jaksch and P Zoller. **Creation of effective magnetic fields in optical lattices: the Hofstadter butterfly for cold neutral atoms.** *New Journal of Physics*, 5(1):56, 2003.